UNIVERSITY OF CALIFORNIA

Los Angeles

Dynamics of Multiferroic Coupling

A dissertation submitted in partial satisfaction of the

requirements for the degree Doctor of Philosophy in

Electrical and Computer Engineering

by

Sidhant Tiwari

2020

© Copyright by

Sidhant Tiwari

2020

ABSTRACT OF THE DISSERTATION

Dynamics of Multiferroic Coupling

by

Sidhant Tiwari

Doctor of Philosophy in Electrical and Computer Engineering

University of California, Los Angeles, 2020

Professor Robert N. Candler, Chair

Multiferroics is a field that has rapidly garnered much interest in the past several years because of its establishment of a new unconventional class of electromagnetic devices. By capitalizing on a special class of material systems that have coupled magnetic and electrical properties, multiferroics offer unique possibilities for micromagnetic devices because of their ability to control magnetization with electric fields (and vice versa). Strain-coupled multiferroic composites, in particular, are promising because their magnetoelectric coupling is many orders-of-magnitude stronger than single-phase multiferroic materials.

Telecommunication systems utilize dynamic magnetic processes for many applications, such as filters, nonreciprocal components, and electrically small antennas. These devices rely on electromagnetic waves for transduction, limiting their sizes and constraining their usage. Strain-coupled multiferroic composites utilize mechanical waves, leading to a five order-of-magnitude reduction in characteristic length and opening the door to device miniaturization. The dynamics of multiferroic coupling can be characterized into several different regimes that depend on the magnetic state of the composite (multi- or single domain) and the actuation

frequency (relative to the domain wall relaxation and the ferromagnetic resonance frequencies). Miniaturization of dynamic magnetic devices relies on the thorough study of multiferroic coupling in these different regimes.

In this work, the dynamics of multiferroic coupling in three different regimes are investigated. A variety of micro-scale piezoelectric devices are designed and fabricated to investigate coupling in each of these regimes. First, resonant cantilevers are used to study dynamic actuation in the regime of quasi-static domain wall motion. It is found that nonlinearity in this regime can lead to doubling of the actuation force frequency, a useful phenomenon for low noise electromagnetic characterization. Second, damping in thin film bulk acoustic resonators in a multi-domain state near ferromagnetic resonance is investigated, and the effect of the domain structure on the power absorption at resonance is characterized. Finally, the perturbations of acoustic Lamb waves caused by a single domain magnetic thin film are studied at frequencies above ferromagnetic resonance. Interactions with spin waves are found to lead to an angular dependence in the magneto-acoustic absorption. These results demonstrate several unique aspects of dynamic multiferroic coupling across different regimes and can be readily capitalized to develop novel micro-scale devices for telecommunication systems.

The dissertation of Sidhant Tiwari is approved.

Sam Emaminejad

Yuanxun Wang

Gregory P. Carman

Robert N. Candler, Committee Chair

University of California, Los Angeles

2020

To Mr. B, the high school teacher that inspired a
lifelong love of physics and engineering.

To my family and the love of my life, for their
unending patience and encouragement.

And most of all, to my brother Sawan, for supporting our
family so I could pursue my dreams. Not one day with a complaint.

Table of Contents

List of Figures ix

List of Symbols xviii

Acknowledgements xxi

Vita xxiii

Chapter 1: Background and Motivation 1

1.1 Introduction to Multiferroic Coupling 1

1.1.1 Multiferroic Materials *1*

1.1.2 Strain-Coupled Multiferroic Composites *4*

1.2 Radio Frequency Magnetic Devices 8

1.2.1 Applications of Dynamic Magnetics *8*

1.2.2 Issues with Miniaturization *10*

1.3 The Case for Dynamic Multiferroics 12

1.3.1 Research on Magneto-Acoustic Coupling *12*

1.3.2 Radio Frequency Piezoelectric Devices *14*

1.4 Research in Dynamic Multiferroics 17

1.4.1 Current State of the Art *17*

1.4.2 Contributions of This Work *21*

Chapter 2: Dynamics of Magnetization 23

2.1 Features of Ferromagnetic Materials 23

2.2 Dynamics of Magnetization 27

2.2.1 Dynamics of a Single Magnetic Moment *27*

2.2.2 Effective Fields *30*

2.2.3 Modifications for a Continuum *31*

2.3 Interactions Within an Amorphous Ferromagnet 33

2.3.1 *Dipolar Interactions* 33
2.3.2 *Exchange Interactions* 35
2.3.3 *Magneto-Elastic Interactions* 36
2.3.4 *Dissipative Interactions* 38
2.4 Solutions to the Equation of Motion 39
2.4.1 *Simplifications for Independent Spins* 39
2.4.2 *Simplifications for a Single Domain Thin Film* 41
2.4.3 *Simplifications for Domain Wall Dynamics* 43
2.4.4 *Regimes of Dynamic Magnetization* 44
Chapter 3: Nonlinear MF Actuation 47
3.1 Wirelessly Actuated Multiferroic Devices 47
3.1.1 *Linear Multiferroic Devices* 47
3.1.2 *Nonlinear Multiferroic Devices* 48
3.2 Nonlinearity from Perpendicular Poling 50
3.3 Experimental Approach 52
3.3.1 *Device Design and Fabrication* 52
3.3.2 *Device Characterization* 55
3.4 Experimental Results 57
3.5 Future Work 60
Chapter 4: FMR Below Saturation 62
4.1 Ferromagnetic Resonance in Saturated Films 62
4.1.1 *Acoustically Driven Ferromagnetic Resonance* 62
4.1.2 *Coupled Magneto-Elastic Resonance* 64
4.2 Ferromagnetic Resonance in Multi-Domain Films 65
4.3 Experimental Approach 68
4.3.1 *Device Design and Fabrication* 68
4.3.2 *Device Characterization* 71
4.4 Experimental Results 73
4.5 Future Work 76
Chapter 5: Magneto-Acoustic Waves 77
5.1 Operation Beyond ADFMR 77
5.1.1 *Deviations from ADFMR Model* 77

5.1.2 *Approximations in ADFMR* ... 78
5.2 Acoustic Wave / Spin Wave Coupling ... 82
5.3 Experimental Approach ... 84
5.3.1 *Device Design and Fabrication* ... 84
5.3.2 *Device Characterization* ... 87
5.4 Experimental Results ... 89
5.5 Future Work ... 91

Chapter 6: Conclusions ... 93

Appendix A1: Fabrication Notes ... 95

A1.1 Lithography ... 95
A1.1.1 *Silicon* ... 95
A1.1.2 *Lithium Niobate* ... 96
A1.1.3 *Aluminum Nitride / Silicon Nitride* ... 98
A1.1.4 *Mask Layout* ... 99
A1.2 Thin Film Deposition ... 101
A1.2.1 *Electron-Beam Evaporation* ... 101
A1.2.2 *Sputtering* ... 102
A1.2.3 *Adhesion Layers for Metallization* ... 104
A1.2.4 *Reactive Sputtering of Aluminum Nitride* ... 105
A1.3 Etching ... 107
A1.3.1 *Wet Etching of Aluminum Nitride* ... 107
A1.3.2 *Plasma Etching of Aluminum Nitride* ... 108
A1.3.3 *Gas Phase Etching of Silicon* ... 108

References ... 110

List of Figures

Figure 1.1: (a) Relations between various subclasses of electrical materials. (b) Relations between various subclasses of magnetic materials. Adapted from [33]. 1

Figure 1.2: Relations between various kinds of electric, magnetic, and magnetoelectric materials. Adapted from [1]. 2

Figure 1.3: (a) Schematic of a hysteresis loop for a “ferroic” material. (b) Cross coupled hysteresis loops for an ideal multiferroic material. Figures from [7]. 3

Figure 1.4: (a) Comparison of magnetoelectric susceptibility ($\chi ME = \epsilon r \epsilon 0 \eta$) for single-phase and composite multiferroics. (b) Approximate comparison of the range of magnetizations and electrical polarizations of different kinds of multiferroic materials. Figures from [4]. 4

Figure 1.5: Schematic of a simple laminate multiferroic composite. Magnetic fields only interact with the piezomagnetic layer and electric fields only interact with the piezoelectric layer. The two layers are mechanically coupled because the strains parallel to the interface and the stresses orthogonal to the interface must be continuous between both materials. .. 5

Figure 1.6: Different types of multiferroic composites: (a) particulate composites, (b) laminated composites, and (c) fiber composites. Figures from [3]. 7

Figure 1.7: (a) Schematic of a thin film multiferroic motor. (b) White-space chart of power density versus volume for different micro-motor technologies. The vertical red dashed line indicates the approximate size of biological cells. Adapted from [23]. 8

Figure 1.8: (a) Geometry of a stripline circulator. (b) Schematic of circulator operation. A wave entering from the input (port 1) only couples to one output port (port 2) and the last port is completely isolated (port 3). Figures from [52]. 9

Figure 1.9: (a) Geometry of a nonreciprocal ferrite waveguide isolator. (b) Attenuation constant as a function of frequency for waves travelling in the forward and backward directions. Figures from [52]. 10

Figure 1.10: Transceiver module for an electronically scanned array radar. Adapted from [43]. 11

Figure 1.11: 1.05 GHz one-port magneto-acoustic delay line made with a single-crystal YIG rod with a diameter of 2.74 mm and length of 7.37 mm. Figure from [69]..................... 13

Figure 1.12: Approximate film thicknesses as a function of frequencies for different types of resonant modes. Width or Length to thickness ratio of 10:1 is assumed. Figure from [63]. 16

Figure 1.13: Time response of a multiferroic near-field coupler. (a) Strain applied by the piezoelectric transducer. (b) Magnetic flux density within the magnetic material. (c) Generated magnetic flux density measured 20 cm away. Figure from [12]................ 19

Figure 1.14: (a) Power absorption of ADFMR as a function of magnetic bias in the x and y directions. Maximal coupling is approximately 45 degrees. (b) Power absorption along the direction of the arrow shown in (a) at different bias magnetic fields. Figures from [173]. 20

Figure 2.1: Sample hysteresis loop of a ferromagnetic material. 23

Figure 2.2: Transformation of domain structure under applied magnetic fields. Domain walls are represented by dashed lines. (a) Multi-domain state at no applied field. (b) Domain wall motion expanding domains parallel to field. (c) High fields with only domains orthogonal to applied field left. (d) Completely saturated sample. 25

Figure 2.3: (a) Ferromagnetic compound with approximately parallel dipoles. (b) Ferrimagnetic material with unequal and antiparallel dipoles. (c) Antiferromagnetic material with equal and antiparallel dipoles. 26
Figure 2.4: Contributes to total angular momentum, $\mathcal{J}$: (a) orbital angular momentum, $\mathcal{L}$, from the electron circling the nucleus and (b) spin angular momentum, $\mathcal{s}$, that is intrinsic to the electron. 28
Figure 2.5: Types of micro-magnetic interactions present in an amorphous ferromagnetic material. These are discussed in depth in Section 2.3. Notice that the material is broken up into several domains 31
Figure 2.6: Demagnetizing constants for a thin plate, thin rod, and sphere. The plate is assumed to be infinitely thin and the rod is assumed to be infinitely long. Figure from [52]. 35
Figure 2.7: (a) Deformation of a sphere via magnetostrictive strains. (b) Saturation of strain in a magnetostrictive material. Adapted from [192]. 37
Figure 2.8: Schematic of various mechanisms of energy redistribution inside a magnetic material. Adapted from [71]. 39
Figure 2.9: Precessional motion of magnetization about the DC bias field. 41
Figure 2.10: (a) Magnetic susceptibility magnitude peaking at FMR. (b) Real and imaginary parts of susceptibility. The imaginary part peaks at FMR, indicating that damping is maximized at this point. 41
Figure 2.11: Measured (a) real and (b) imaginary parts of permeability for Ni-Zn Ferrite for several bias magnetic fields. Note that the frequency axis is in log-scale. Figures from [204]. 44
Figure 2.12: Trend for the instantaneous susceptibility of an arbitrary magnetic material. This is broken up into three zones depending on the frequency: Quasit-Static, Cut-Off, and Spin Precession. 45

Figure 3.1: (a) Variation of magnetostrictive strain, $Smag$, and piezomagnetic constant, $q33$, as a function of bias magnetic field. Adapted from [209]. (b) Frequency dependence of multiferroic transduction at two different bias magnetic fields in a multiferroic transformer. The coupling peaks at the mechanical resonance frequency. Figure from [207]. 48

Figure 3.2: (a) Schematic of harmonic RFID system. The reader emits a $1f$ signal, and the passive RFID tag reradiates a $2f$ signal to distinguish itself from backscatter. (b) Package of a test device with parasitic antennas identified. These antennas receive electromagnetic signals and make it difficult to characterize the true device response. 49

Figure 3.3: Pictorial representation of magneto-elastic frequency doubling through perpendicular poling. The purple arrows are the magnetic dipoles in the material and the red lines represent the magnetostrictive strain associated with the magnetic dipoles. The material is assumed to have negative magnetostriction, so the red axis is associated with compressive strain. 52

Figure 3.4: (a) Cross section of a multiferroic bimorph cantilever. Depicted is the resonant mode excited by an AC magnetic field along the long axis of the cantilever. The dotted lines represent the undeformed state. (b) Multiferroic cantilever before silicon etching to release the MEMS structure. The purple arrows indicate the intended direction of the DC magnetization during the experiments. 53

Figure 3.5: Cross sections of the fabrication process flow for the multiferroic MEMS cantilevers. 54

Figure 3.6: (a) Normalized measured hysteresis loop for the deposited nickel thin film. (b) PCB with a device to be tested in the vacuum chamber. (c) Measured frequency response of the MEMS multiferroic cantilever when driven with the piezoelectric layer. 55

Figure 3.7: Schematic of the test set up used to characterize multiferroic MEMS cantilevers. 56

Figure 3.8: (a) Displacement measured at twice the frequency of the magnetic field generated by the Helmholtz coils, showing a peak when the drive frequency is half of the resonance frequency. (b) Peak amplitude measured as a function of the AC voltage applied to the coil. Because the coupling is nonlinear, the displacement varies quadratically with amplitude. 58

Figure 3.9: (a) Displacement of the cantilever measured at the magnetic field frequency. (b) Displacement of the cantilever at twice the magnetic field frequency. (c) Measured output voltage at the magnetic field frequency. (d) Measured output voltage at twice the magnetic field frequency. 59

Figure 4.1: (a) Typical SAW device used for ADFMR experiments. Nickel is used as the magnetostrictive thin film and $LiNbO_3$ is the piezoelectric substrate. Adapted from [174]. (b) Angular dependence of SAW attenuation in ADFMR. Peak attenuation is measured at about 40°. Figure from [173]. 63

Figure 4.2: (a) Return loss of a multiferroic HBAR resonator in the regime of maximized multiferroic coupling. (b) Dispersion relation of magneto-elastic waves. (c) Plotted resonance frequency shift versus bias magnetic field. The trends here recreate the magneto-elastic dispersion curve, indicating strong bidirectional coupling between the mechanical resonance and FMR. Adapted from [184]. 65

Figure 4.3: (a) Layered domain structure in a single crystal ferromagnet with a cubic crystal structure. (b) Magnetic resonant modes of (a) below and above saturation. Adapted from [71]. 66

Figure 4.4: Measured magnetic resonance frequencies versus magnetic field for a single crystal sample below and above saturation. The two curves are for applied fields in two different directions. Figure from [220]. 67

Figure 4.5: Schematic of the thin film bulk acoustic wave resonator used to characterize spin precession in a multi-domain ferromagnetic material. 68

Figure 4.6: Process used for the fabrication of multiferroic FBARs. 69

Figure 4.7: (a) Nickel lift-off pattern showing "winging" effects due to conformal sputter deposition. (b) Nickel lift-off of stripes with deposition process tuned to give larger Ni mean free path during deposition. The effects of shadowing can be seen on the edges of the stripes by the discoloration.. 70

Figure 4.8: Microscope image of a multiferroic FBAR device before XeF2 etching. Notice that the top electrode appears brown despite it being platinum. This is due to the roughening of the aluminum nitride surface from its exposure to TMAH. 70

Figure 4.9: Measured reflection and transmission coefficients of the fabricated multiferroic FBAR. 71

Figure 4.10: Magnetic hysteresis loop for a characteristic nickel sample. Measured using SQUID. 71

Figure 4.11: (a) Characterization test set up used to measure the S_{11} as a function of bias magnetic field magnitude and angle. (b) Simple circuit model used for data analysis... 72

Figure 4.12: Percent change in conductance as a function of frequency and magnetic field. a) At 0° applied magnetic field near 1.8 GHz. b) At 0° applied magnetic field near 3.2 GHz. c) At 45° applied magnetic field near 3.2 GHz. d) At 85° applied magnetic field near 3.2 GHz. 73

Figure 4.13: Simulated magnetization response (solid line) compared to percent change in conductance at the mode frequency (dashed line) as a function of magnetic field...... 75

Figure 5.1: Attenuation of SAW by ADFMR for four nickel film thicknesses at 2 GHz: (a) 20 nm, (b) 30 nm, (c) 40 nm, (d) 50 nm. All Samples have a 5 nm gold capping layer. Color bar in units of dB/mm. Figure from [226]. 78

Figure 5.2: Illustration of the difference between the long wavelength and short wavelength regimes on the uniformity of the spin precession. 79

Figure 5.3: Angular dependence of the effective magnetic fields from extensional and shearing strains. Dotted lines represent negative numbers. 81

Figure 5.4: Analytical model for the dependence of the bias magnetic field magnitude needed for the existence of a spin wave mode as a function of the angle between the bias magnetic field and the spin wave propagation direction, keeping the spin wave frequency and wavelength fixed. 84

Figure 5.5: Schematic of Lamb wave delay line used for characterization. The angle between the acoustic wave propagation direction and the bias magnetic field applied by the electromagnet is shown as θ. These devices use a shorted grating for the top electrode and a plate for the bottom electrode. The electric field (E) generated by the electrodes create an axial extensional stress under the electrode strips (red arrows). By the Poisson effect, this creates an in-plane stress (blue arrows). This in-plane stress then creates a negative axial stress between the electrode stripes (yellow arrows). The fundamental mode will have the wavelength half that of a design using traditional IDTs with the same dimensions. 85

Figure 5.6: Cross sections of the fabrication process for multiferroic Lamb wave delay lines. 86

Figure 5.7: Image of released multiferroic Lamb wave delay line. The holes are used to increase the area of the suspended membrane to minimize any acoustic reflections from the edges of the device. 87

Figure 5.8: (a) Measured Lamb wave transmission, and simulated (b) extensional and (c) shear strains along the length off the delay line for the chosen mode of operation. 88

Figure 5.9: Experimental set up used for characterization of Lamb wave delays lines. The inset figure is the device mounted on to the CPW used for characterization. 89

Figure 5.10: Change in S_{21} of the chosen acoustic mode, 7.492 GHz, as a function of the DC magnetic field at an angle of 30˚. Attenuation of the acoustic wave by the magnetic thin film maximizes near 250 Oe, indicating the presence of a spin wave mode that matches the acoustic wave wavelength and frequency.. 90

Figure 5.11: Measured magnetic field for maximal damping of the acoustic wave versus angle of the magnetic field relative to the Lamb wave propagation direction. 90

Figure A1.1: Lithography process developed for nLof 2020 on a bare silicon substrate. Typical minimum feature size of this process is 2 µm. 95

Figure A1.2: Lithography process developed for nLof 2020 on a bare lithium niobate substrate. Typical minimum feature size of this process is 2.5 µm. 97

Figure A1.3: Lithography process developed for KMPR 1005 on 400 nm of aluminum nitride (or silicon nitride) on a silicon substrate. Typical minimum feature size of this process is 2 µm.. 99

Figure A1.4: Sample lithography mask. Grid lines are highlighted in yellow. Alignment verniers are highlighted in red. The blue dotted circle shows where a 4-inch wafer would sit once aligned to the mask. Green dotted boxes highlight identifying text for the mask. 100

Figure A1.5: Relation between plasma pressure and residual film stress for 100 nm of sputtered molybdenum. Each curve is for a different type of plasma. Figure from [231]. 103

Figure A1.6: (a) Lift-off results for sputtered nickel film with a conformal deposition. The jagged edges are “winging” due to the coating of the photoresist sidewall. (b) Photoresist sputter coated by nickel with a low-pressure sputtering process. Notice how the negative sidewall is not as heavily coated by metal, as shown by its darker color in the image. (c) Lift-off results for nickel using a low-pressure sputtering process. Notice the absence of any winging. Because of the long mean free path of the sputtered material, there is

shadowing by the photoresist during deposition. This manifests itself as thinner regions at the pattern edges in the image. 104

Figure A1.7: Measured magneto-optic Kerr effect (MOKE) response from a nickel thin film deposited with and without a titanium adhesion layer. 105

Figure A1.8: Measured c-axis angular spread in aluminum nitride as a function of film thickness and underlayer. Figure from [63]....106

Figure A1.9: (a) Via etched in aluminum nitride with hot phosphoric acid. The spotty surface of the via is indicative of inversion domains. (b) Sidewall slope of wet etched via. Adapted from [96]. 107

List of Symbols

Mathematical Notation

Symbol	Meaning
j	imaginary unit, $j^2 = -1$
$\underline{x}$	position vector
$\hat{x}$	x-direction unit vector
$\hat{y}$	y-direction unit vector
$\hat{z}$	z-direction unit vector
$\underline{u}$	displacement vector
t	time
f	frequency
ω	angular frequency, radial frequency
k	wave vector, wave number
$\underline{\hat{n}}$	direction normal to an interface
$g(A)$	g as a function of A
$\frac{\partial g}{\partial A}$	partial derivative of g with respect to A
$\dot{A}$, $\frac{d}{dt}A$	first derivative of A with respect to time
$\ddot{A}$	second derivative of A with respect to time
A	scalar, (zeroth order tensor)
$\underline{A}$	vector, (first order tensor)
$\underline{\underline{A}}$	second order tensor
$\underline{\underline{\underline{A}}}$	third order tensor
$\underline{\underline{\underline{\underline{A}}}}$	fourth order tensor
A_p	pth component of $\underline{A}$
A_{pq}	pqth component of $\underline{\underline{A}}$
$\underline{\underline{A}}^T$	transpose of $\underline{\underline{A}}$
$\underline{\underline{\underline{\underline{A}}}}^T$	transpose of $\underline{\underline{\underline{\underline{A}}}}$
$\underline{\hat{A}}$	unit vector in the direction of $\underline{A}$
$\lvert A \rvert$	absolute value of A, magnitude of A
$\langle A \rangle$	average value of A
$\underline{A} \cdot \underline{B}$	dot product of $\underline{A}$ and $\underline{B}$
$\underline{A} \times \underline{B}$	cross product of $\underline{A}$ with $\underline{B}$
$\underline{\nabla}$	del operator
$\underline{\nabla} A$	gradient of A
$\underline{\nabla} \cdot \underline{A}$	divergence of $\underline{A}$
$\underline{\nabla} \times \underline{A}$	curl of $\underline{A}$
$\nabla^2 A$	laplacian of A
$\int_{\mathbb{S}} g(\underline{x})\, d^2\underline{x}$	surface integral of $g(\underline{x})$
$\int_{\mathbb{V}} g(\underline{x})\, d^3\underline{x}$	volume integral of $g(\underline{x})$

Physical Constants

μ_0	vacuum permeability	γ	gyromagnetic ratio
ϵ_0	vacuum permittivity		

Mechanics

U_A	energy density due to A	$\underline{\underline{S}}$	strain tensor
$\underline{u}$	displacement vector	$\underline{\Gamma}$	net torque
$\underline{\underline{T}}$	stress tensor		

Electromagnetics

$\underline{E}$	electric field	$\underline{B}$	magnetic flux density
$\underline{D}$	electric displacement field	$\underline{b}$	time-varying magnetic flux density, AC magnetic flux density
$\phi(\underline{x})$	magnetostatic potential		
$\underline{H}$	magnetic field	$\underline{M}$	magnetization
H_0	magnitude of DC magnetic field	$\underline{M_0}$	DC magnetization
$\underline{h}$	time-varying magnetic field, AC magnetic field	$\underline{m}$	time-varying magnetization, AC magnetization
		$\underline{\mathfrak{m}}$	magnetic dipole moment

Quantum Mechanics

$\underline{\mathcal{S}}$	spin angular momentum	$\underline{\mathcal{J}}$	total atomic angular momentum
$\underline{\mathcal{L}}$	orbital angular momentum		

Material Properties

Symbol	Description
ρ_A	volume density of A
$\underline{\underline{\underline{\underline{c}}}}$	stiffness tensor
$\underline{\underline{\epsilon}}$	permittivity tensor
$\underline{\underline{\chi}}$	magnetic susceptibility tensor
$\underline{\underline{\mu}}$	permeability tensor
$\underline{\underline{\underline{e}}}$	piezoelectric coupling tensor (stress-charge form)
$\underline{\underline{\underline{q}}}$	piezomagnetic coupling tensor (stress-flux form)
$\underline{\underline{\eta}}$	multiferroic coupling tensor, magnetoelectric coupling tensor
$\underline{\underline{\underline{\underline{c_A}}}}$	stiffness at constant A
$\underline{\underline{\epsilon_A}}$	permittivity at constant A
$\underline{\underline{\mu_A}}$	permeability at constant A
H_{sat}	saturating field
H_c	coercive field
M_r	remanent magnetization
M_s	saturation magnetization
N_p	demagnetization constant along the p-axis
λ_s	saturation magnetostriction
D	spin stiffness, exchange constant
B_{ME}	magneto-elastic energy constant
α	Gilbert damping constant
m_w	domain wall effective mass
β_w	domain wall damping
α_w	domain wall stiffness
ξ	domain wall displacement

Acknowledgements

Among all of those who have contributed to this work and my experience at UCLA, I would like to single out seven specific people. First are Qiang Xu and Paul Nordeen, who spent the early years of my PhD teaching me the fundamentals that would eventually grow into the work presented in this text. Next are Zhi Yao and Joseph Devin Schneider, who have been my closest collaborators and have been absolutely integral to the work done during my doctorate. Thirdly are Max Ho and Jimmy Wu, who have been my closest friends and confidants during my time at UCLA, having been there for me on both good days and bad. Lastly is my research advisor, Professor Rob Candler, whose thoughtful mentorship I attribute not only this work but the future successes of my career.

Over the course of my doctorate, I have had the good fortune to work with a large number of colleagues who have all contributed to this work and my own personal growth. I would like to thank all of my STL labmates (Zhuyun Xiao, Ling Li, Siyuan Liu, Ben Pound, Yuan Dai, Hyunmin Sohn, Omeed Paydar, Jere Harrison, Srikanth Iyer, Yongha Hwang, and Jonathan Lake), my AML collaborators (Kyle Wetzlar, Scott Keller, Jesse Rivera, Andres Chavez, Anthony Barra, John Domann, K.P. Mohanchandra, Paymon Shirazi, and Jinzhao Hu), my DML collaborators (Ting Lu, Kevin Luong, and Umut Tok), my TANMS 2D thrust collaborators (Nishanth Virushabadoss, Colin Rementer, Kevin Fitzell, Adrian Acosta, Adi Jung, Dominic Labanowski, Ty Karaba, Shauna Robbennolt, Shreya Patel, Hwaider Lin, and Xianfeng Liang), my international collaborators (Sebastian Wintz, Killian Lenz, Phani Arekapudi, Olav Hellwig, Juergen Lindner, and Rei-Fu Xu), the undergraduate and master’s students I have worked with

(Natalie Lin, Amanda Marotto, Mohammad Shahili, Jenna Davis, Brandon Read, Neil Ramirez, Dwayne McKinney Jr, Tylisia Wallace, Daniel Corona, Rodrigo Curiel, and Fausto Rendon), and several others (Kuan-Wen Tung, Michael Moon, and Scott Burnside).

For supporting the experimental portions of this work, I would like to thank the UCLA Nanoelectronics Research Facility and the Integrated Systems Nanofabrication Cleanroom for the use of their extensive fabrication facilities, and the Center for High Frequency Electronics for the access to their wide suite of experimental equipment and electromagnetics simulation software. I would also like to thank Qualcomm and the Translational Applications of Nanoscale Multiferroic Systems (TANMS) NSF Engineering Research Center for funding the projects that served as the basis of this dissertation.

Vita

EDUCATION

University of California, Los Angeles
M.S. Electrical Engineering *Sept. 2013 – Mar. 2015*

University of California, Berkeley
B.S. Engineering Physics *Aug. 2009 – May 2013*

HONORS AND AWARDS

- 2020 Distinguished PhD Dissertation Research Award (UCLA Department of Electrical and Computer Engineering, Physical and Wave Electronics)
- 2019 TANMS CLIMB Award
- 2018 UCLA Dissertation Year Fellowship
- 2018 IEEE International Frequency Control Symposium (IFCS) Best Student Paper Award (Group 4: Sensors and Transducers)
- 2015 Qualcomm Innovation Fellowship
- Southern California United Food and Commercial Workers (UFCW) Scholarship: Highest Award for 2009; Second Highest Award for 2011, 2012

JOURNAL PUBLICATIONS

[1] Z. Xiao, R. Lo Conte, M. Goiriena-Goikoetxea, R.V. Chopdekar, C.H. Lambert, X. Li, A.T. N'Diaye, P. Shafer, **S. Tiwari**, A. Barra, A. Chavez, K.P. Mohanchandra, G.P. Carman, K. Wang, S. Salahuddin, E. Arenholz, J. Bokor, R.N. Candler, "Tunable Magnetoelastic Effect in Voltage-controlled Exchange-coupled Composite Multiferroic Microstructures." *ACS Applied Materials & Interfaces*, 2020.

[2] J.D. Schneider, J.P. Domann, M.K. Panduranga, **S. Tiwari**, P. Shirazi, Z. Yao, C. Sennott, D. Shahan, S. Selvin, G. McKnight, W. Wall, R.N. Candler, Y.E. Wang, and G.P. Carman, "Experimental Demonstration and Operating Principles of a Multiferroic Antenna." *Journal of Applied Physics*, 126(22), 224104, 2019.

[3] Z. Yao, **S. Tiwari**, T. Lu, J. Rivera, K. Luong, R.N. Candler, G.P. Carman, and Y.E. Wang, "Modeling of Multiple Dynamics in the Radiation of Bulk Acoustic Wave (BAW) Antennas." *IEEE Journal on Multiscale and Multiphysics Computational Techniques*, 2019.

[4] A.C. Chavez, J.D. Schneider, A. Barra, **S. Tiwari**, R.N. Candler, and G.P. Carman, "Voltage-Controlled Ferromagnetic Resonance of Dipole-Coupled $Co_{40}Fe_{40}B_{20}$ Nanoellipses." *Physical Review Applied*, 12(4), 044071, 2019.

[5] **S. Tiwari**, and R.N. Candler, "Using Flexural Mems to Study and Exploit Nonlinearities: A Review." *Journal of Micromechanics and Microengineering*, 29(8), 083002, 2019.

[6] K.W. Tung, P.S. Chung, C. Wu, T. Man, **S. Tiwari**, B. Wu, Y.F. Chou, F.L. Yang, and P.Y. Chiou, "Deep, Sub-Wavelength Acoustic Patterning of Complex and Non-Periodic Shapes on Soft Membranes Supported by Air Cavities." *Lab on a Chip*, 19(21), 3714-3725, 2019.

[7] Z. Xiao, K.P. Mohanchandra, R. Lo Conte, T. Karaba, J.D. Schneider, A. Chavez, **S. Tiwari**, H. Sohn, M.E. Nowakowski, A. Scholl, S.H. Tolbert, J. Bokor, G.P. Carman, and R.N. Candler, "Enhanced Magnetoelectric Coupling In A Composite Multiferroic System Via Interposing A Thin Film Polymer." *AIP Advances*, 8(5), 055907, 2018.

CONFERENCE PRESENTATIONS

[1] J.D. Schneider, T. Lu, **S. Tiwari**, X. Zou, A. Mal, R.N. Candler, Y.E. Wang, and G.P. Carman, "High frequency parametric mixing in Lamb waves using a time and space varying elastic modulus (Conference Presentation)." Proc. SPIE 11379, Sensors and Smart Structures Technologies for Civil, Mechanical, and Aerospace Systems 2020, 113792I, 2020.

[2] J.D. Schneider, T. Lu, **S. Tiwari**, X. Zou, A. Mal, R.N. Candler, Y.E. Wang, and G.P. Carman, "Parametric Coupling in Aluminium Nitride Lamb Wave Devices Through A Nonlinear Elastic Modulus." Bulletin of the American Physical Society, 2020.

[3] Z. Xiao, R. Lo Conte, M. Goiriena, R. V. Chopdekar, X. Li, **S. Tiwari**, C.H. Lambert, S. Salahuddin, G. P. Carman, K. Wang, J. Bokor, and R.N. Candler, "Electric-Field Controlled Magnetic Reorientation in Exchange Coupled CoFeB/Ni Bilayer Microstructures.", *PowerMEMS Conference (The 18th International Conference on Micro and Nanotechnology for Power Generation and Energy Conversion Applications), IOP Conference Series*, 2019.

[4] **S. Tiwari**, M. Ho, A. Marotto, and R.N. Candler, "Frequency Doubling in Wirelessly Actuated Multiferroic MEMS Cantilevers." *2018 IEEE International Frequency Control Symposium (IFCS)* (pp. 1-3). IEEE, 2018.

[5] R.F. Xu, **S. Tiwari**, R.N. Candler, and S.Y. Chen, "Polarization Control of Bulk Acoustic Wave-Mediated Multiferroic Antennas Based on Thickness Shear Modes." *12th European Conference on Antennas and Propagation (EuCAP 2018)* (pp. 1-5). IET, 2018.

[6] **S. Tiwari**, P. Nordeen, Q. Xu, Z. Yao, Y.E. Wang, G.P. Carman, and R.N. Candler, "Ferromagnetic Resonance in Bulk-Acoustic Wave Multiferroic Devices." *Proceedings of Solid-State Sensors, Actuators, and Microsystems Workshop (Hilton Head),* (pp. 420-423), 2016.

Chapter 1 Background and Motivation

1.1 Introduction to Multiferroic Coupling

1.1.1 Multiferroic Materials

Multiferroics is a rapidly growing field that has garnered much interest in the past several years because of its establishment of a new unconventional class of electromagnetic devices [1]–[9]. In typical electromagnetic materials (Figure 1.1), the properties of the electric and magnetic polarizations are completely independent. Electric polarization serves as the base of a large variety of electronic applications, such as capacitors, transistors, transmission lines, and antennas. Magnetic polarization has similarly been widely used, proving to be useful in inductors, solenoid actuators, motors, and many other devices. Multiferroic materials (Figure 1.2) are a special class of materials where the electrical and magnetic properties cross couple, offering unique and unprecedented device concepts to be possible, enabling new classes of

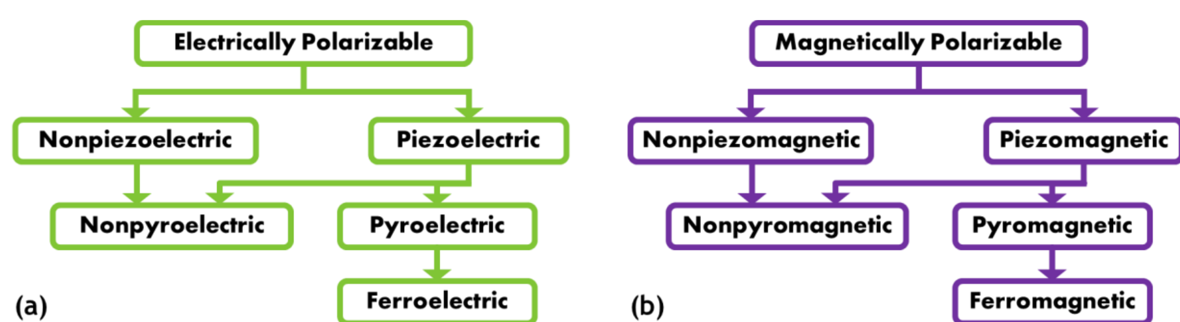

Figure 1.1: (a) Relations between various subclasses of electrical materials. (b) Relations between various subclasses of magnetic materials. Adapted from [33].

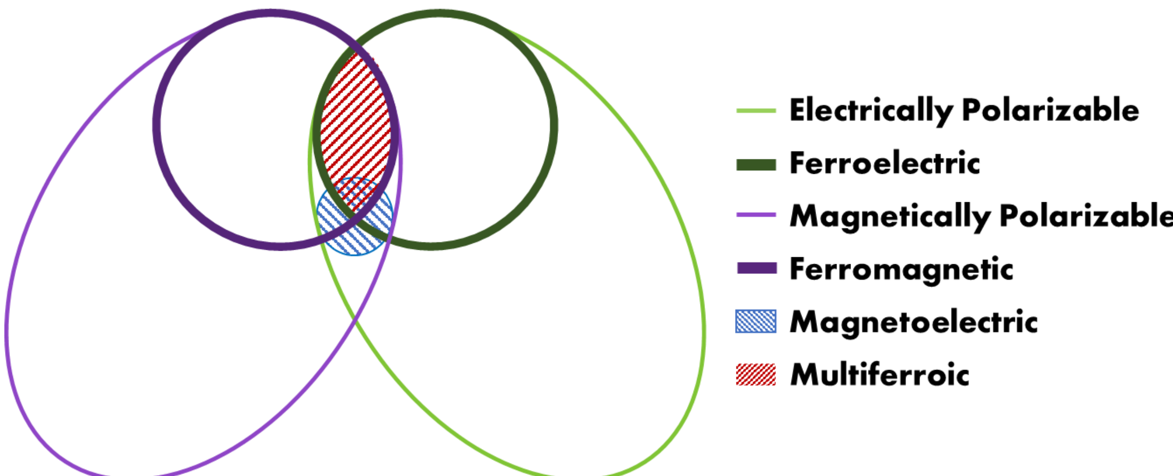

Figure 1.2: Relations between various kinds of electric, magnetic, and magnetoelectric materials. Adapted from [1].

antennas [10]–[12], memory devices [13]–[16], sensors [17]–[19], micro-actuators [20]–[23], signal processing devices [24]–[28], and many other types of devices.

The constitutive laws for a multiferroic material are nearly the same as a typical electromagnetic material with one alteration, as shown below in Equations 1.1 and 1.2.

$$\underline{B} = \underline{\underline{\mu_E}}\,\underline{H} + \underline{\underline{\eta}}^T\,\underline{E} \tag{1.1}$$

$$\underline{D} = \underline{\underline{\epsilon_H}}\,\underline{E} + \underline{\underline{\eta}}\,\underline{H} \tag{1.2}$$

Here $\underline{\underline{\mu_E}}$ and $\underline{\underline{\epsilon_H}}$ are the permeability (measured at constant electric field) and permittivity (measured at constant magnetic field) tensors, respectively, that are present in every electromagnetic material. In multiferroic materials there is also a magnetoelectric coupling coefficient, represented by the tensor $\underline{\underline{\eta}}$, that couples the magnetic state to the electric field and vice versa. In the specific case where the cross coupled properties are "ferroic", meaning they have hysteresis, the material is multiferroic (Figure 1.3). In practice, however, the term multiferroic is often used interchangeably with magnetoelectric, especially in the case of dynamic problems.

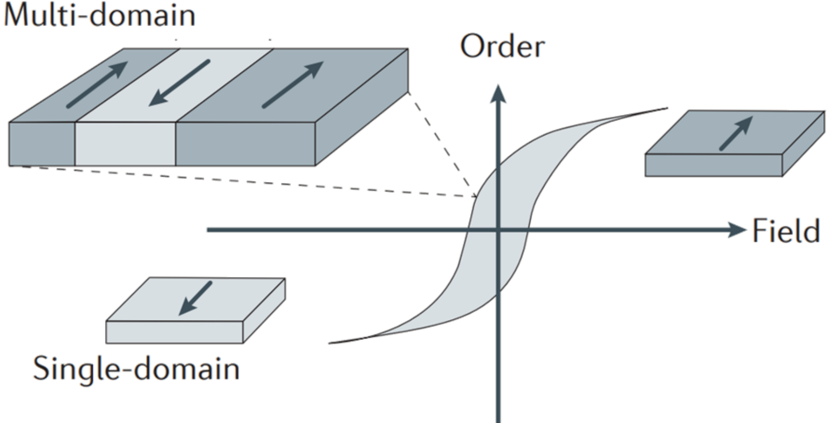

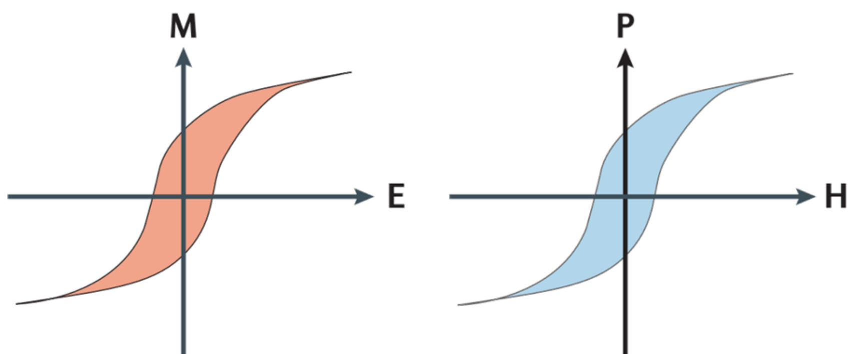

Figure 1.3: (a) Schematic of a hysteresis loop for a "ferroic" material. (b) Cross coupled hysteresis loops for an ideal multiferroic material. Figures from [7].

Development of single-phase multiferroic materials has been an active area of investigation [2], [4], [6], [7], [29]. These materials can be categorized as Type-I multiferroics, where the ferroelectricity and ferromagnetism have independent atomic origins, and Type-II, where the ferroelectric order is due to the magnetic ordering within the material itself [4], [7], [30]. Of these materials, bismuth ferrite ($BiFeO_3$) has generated the most interest, with approximately 6,000 papers published on this material over the past decade [6], [31]. One of the few materials that exhibit room temperature magnetoelectricity, modern interest in the material traces its origin to a paper by Wang et al., demonstrating a giant magnetoelectric coefficient of 3 V/(cm·Oe) in heteroepitaxially constrained 70 nm thick films [32].

1.1.2 Strain-Coupled Multiferroic Composites

Practical application of single-phase multiferroic materials has been seriously hampered by the fact that many of the materials only exhibit multiferroic properties below room temperature and, when they are present, the coupling is weak [3], [5], [8], [9]. Considering general trends in magnetic and electrical materials provides some intuition as to why this is the case. The materials with the strongest magnetic responses are metallic. However, mobile charge carriers in a metal will screen out electric fields, rendering any dielectric effects to be effectively nonexistent. One avenue to bypass this physical restriction is to approach the problem by using composites [3], [5]. Many materials with strong magnetic and electrical properties also strongly couple to mechanical strains. By mechanically coupling piezomagnetic and piezoelectric materials via strain, multiferroic composite materials with magnetoelectric coupling factors, magnetizations, and electrical polarizations of many orders-of-magnitude above that of single-phase materials can be made, as shown in Figure 1.4.

Instead of a single pair of constitutive laws, the system is now described by a pair of constitutive laws for each element in the composite. For the example laminate composite in

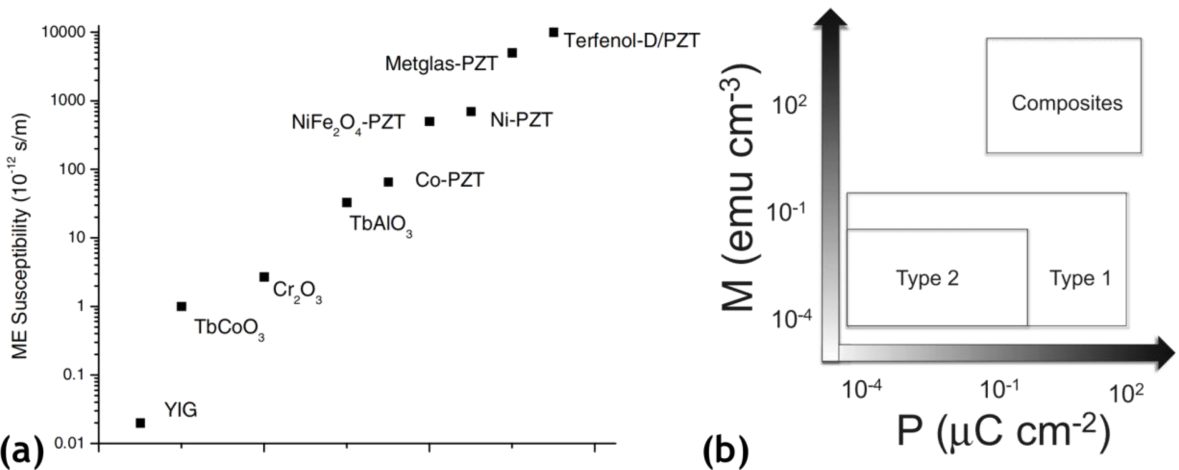

Figure 1.4: (a) Comparison of magnetoelectric susceptibility ($\chi_{ME} = \epsilon_r \epsilon_0 \eta$) for single-phase and composite multiferroics. (b) Approximate comparison of the range of magnetizations and electrical polarizations of different kinds of multiferroic materials. Figures from [4].

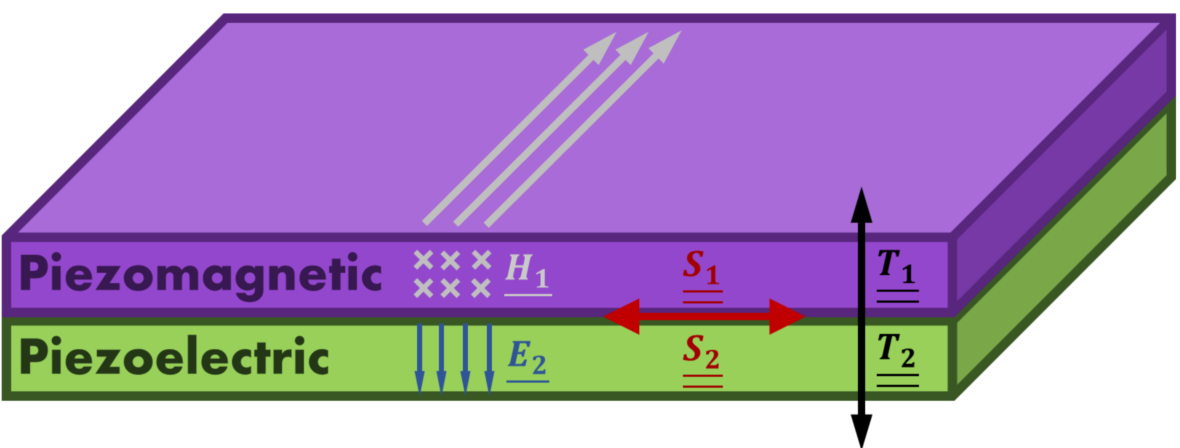

Figure 1.5: Schematic of a simple laminate multiferroic composite. Magnetic fields only interact with the piezomagnetic layer and electric fields only interact with the piezoelectric layer. The two layers are mechanically coupled because the strains parallel to the interface and the stresses orthogonal to the interface must be continuous between both materials.

Figure 1.5, the multiferroic coupling is described by the system of four equations below: one pair of constitutive laws for the piezomagnetic material (denoted by the subscript 1), and one pair for the piezoelectric material (denoted by the subscript 2).

$$\underline{B_1} = \underline{\underline{\mu_T}}\,\underline{H_1} + \underline{\underline{\underline{q}}}\,\underline{\underline{S_1}} \tag{1.3}$$

$$\underline{\underline{T_1}} = \underline{\underline{\underline{\underline{c_H}}}}\,\underline{\underline{S_1}} - \underline{\underline{\underline{q^T}}}\,\underline{H_1} \tag{1.4}$$

$$\underline{D_2} = \underline{\underline{\epsilon_T}}\,\underline{E_2} + \underline{\underline{\underline{e}}}\,\underline{\underline{S_2}} \tag{1.5}$$

$$\underline{\underline{T_2}} = \underline{\underline{\underline{\underline{c_E}}}}\,\underline{\underline{S_2}} - \underline{\underline{\underline{e^T}}}\,\underline{E_2} \tag{1.6}$$

Here $\underline{\underline{\underline{\underline{c_H}}}}$ ($\underline{\underline{\underline{\underline{c_E}}}}$) is the stiffness tensor measured at constant magnetic (electric) field, $\underline{\underline{\underline{e}}}$ is the piezoelectric coupling tensor, and $\underline{\underline{\underline{q}}}$ is the piezomagnetic coupling tensor. The multiferroic coupling is then due to the interfacial mechanical coupling between these materials, in accordance with the conditions of continuity of force and displacement across the interface.

$$\underline{\hat{n}} \cdot \underline{\underline{T_1}} = \underline{\hat{n}} \cdot \underline{\underline{T_2}} \tag{1.7}$$

$$\underline{u_1} = \underline{u_2} \tag{1.8}$$

Here $\underline{\hat{n}}$ is a unit vector normal to the interface. The material displacement is related to the material strain by the following equation:

$$\underline{\underline{S}} = \frac{1}{2}\left(\underline{\nabla}\,\underline{u} + \left(\underline{\nabla}\,\underline{u}\right)^T\right) \tag{1.9}$$

Materials typically only demonstrate piezomagnetic properties below room temperature and, even then, the coupling is weak [33]-[35]. To realize practical composites with high multiferroic coupling, magnetostrictive ferromagnetic materials are used instead [3], [5]. These materials (such as Terfenol-D, nickel, and galfenol) have already shown great success in making magneto-mechanical transducers [36], [37]. The coupling in these materials is highly nonlinear, but in practice linear piezomagnetic operation can be approximated if a bias magnetic field or prestress is applied.

There are many methods to form these composites (Figure 1.6) [3]. Of these, laminated multiferroic composites have been particularly popular for device applications [3], [5], [38]. A major thrust in this research area has been the development of energy efficient micromagnetic devices. Using traditional methods, magnetic devices all require some form of an inductor to generate the magnetic energy needed in these devices. However, miniaturization of these devices come at a major cost of efficiency as the Ohmic loss skyrockets in the inductor loop wiring as dimensions shrink. In contrast, electrical devices utilizing some form of a capacitor have shown excellent scalability, as evidenced by the order-of-magnitude reduction in feature size of the CMOS transistor during the last two decades [39].

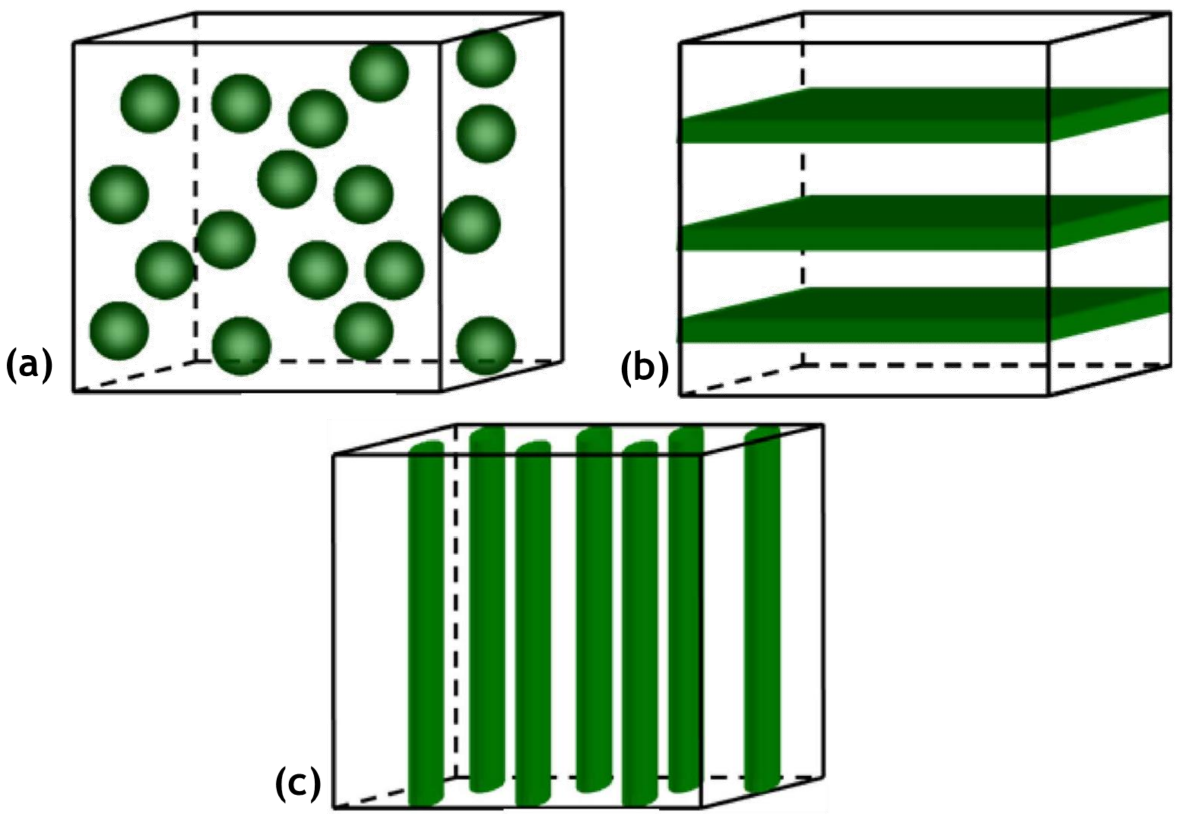

Figure 1.6: Different types of multiferroic composites: (a) particulate composites, (b) laminated composites, and (c) fiber composites. Figures from [3].

In these micro-multiferroic devices, the magnetic state within the magnetic thin film is controlled via an applied strain. Due to internal forces within the magnetic material, the geometry of the structure greatly influences the possible magnetic states, leading to research on multiferroic coupling in a wide variety of thin film geometries, such as rectangles/squares [13], [16], [20], [40], ellipses/circles [14], [21], and rings [22]. Modifying the magnetic state in these structures is functionally equivalent to changing the position of a permanent magnet or the strength of an electromagnet, and it is this equivalence that enables multiferroics to mimic macro-scale magnetic devices. This mechanism has been exploited to develop multiferroic motors that can capture and displace magnetic micro-beads [20]–[23], a promising technology for sorting of individual biological cells as multiferroic motors offer the highest power densities at cell size scales (Figure 1.7). This mechanism has also been applied for the development of

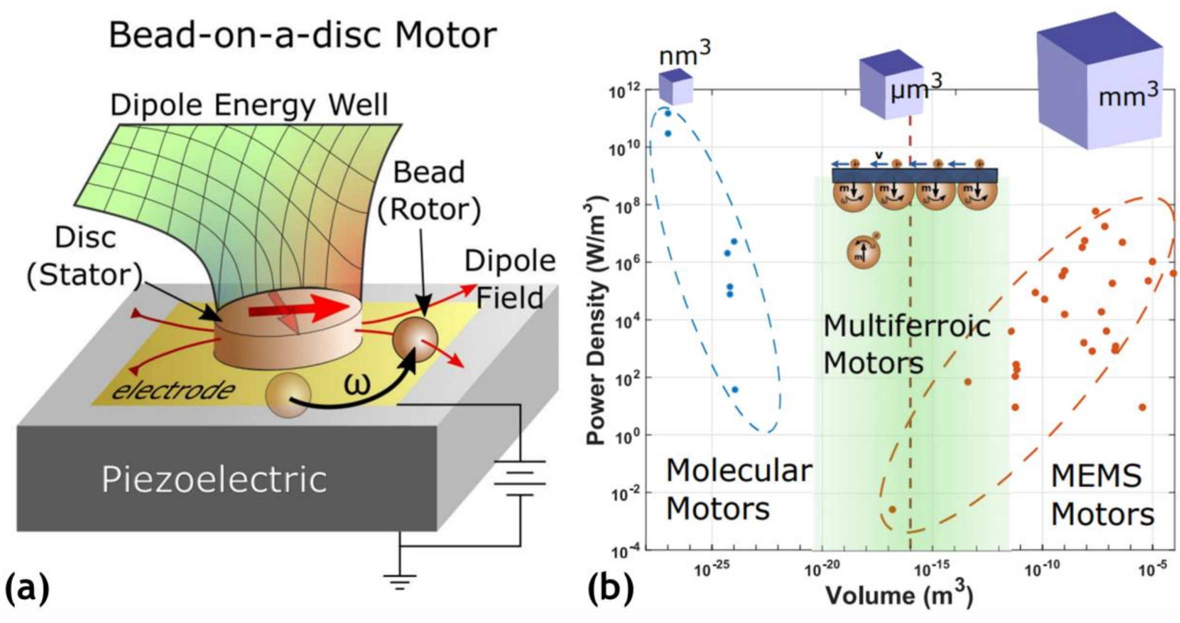

Figure 1.7: (a) Schematic of a thin film multiferroic motor. (b) White-space chart of power density versus volume for different micro-motor technologies. The vertical red dashed line indicates the approximate size of biological cells. Adapted from [23].

novel memory devices. One such device is a multiferroic read head developed by Zhang et al. for magnetic hard disk drives [13]. Using magnetic tunnel junctions, strain-coupled multiferroic magnetic random-access memory (MRAM) has also been developed [14], which has the potential to have much lower write energies than the current state-of-the-art [15]. If ferromagnetic and ferroelectric materials are simultaneously used, a four-state memory bit is even possible [16].

1.2 Radio Frequency Magnetic Devices

1.2.1 Applications of Dynamic Magnetics

The applications discussed in the last section utilize a quasi-static control of the magnetic state. However, there are many unique dynamic processes in magnetic materials that have successfully found numerous applications in radio frequency (RF) telecommunication systems. These devices use high resistivity magnetic materials, known as ferrites, to carry

dynamic electromagnetic fields without eddy current damping [41]–[44]. The simplest of these applications are based on wire loops with a ferrite core (or substrate) to boost the magnetic flux, such as inductors [45], [46], transformers [47]–[49], and loop antennas [50], [51].

Several applications couple electromagnetic waves directly to the motion of the dynamic magnetization within the magnetic material [41]–[43], [52], [53]. One such application is the circulator, a 3-port device that leverages the unique “rotation” associated with the dynamic magnetization to steer electromagnetic waves, as shown in Figure 1.8. This steering property is integral for transceiver systems, where the circulator prevents crosstalk between the transmitted and received signals that pass through a single antenna. Another application that takes advantage of this “rotation” is the nonreciprocal isolator, a 2-port device that absorbs electromagnetic waves in one direction and not the other (Figure 1.9). There are also applications that take advantage of the nonlinear aspects of dynamic magnetization, such as frequency selective limiters and signal-to-noise enhancers [53]. Applications of dynamic

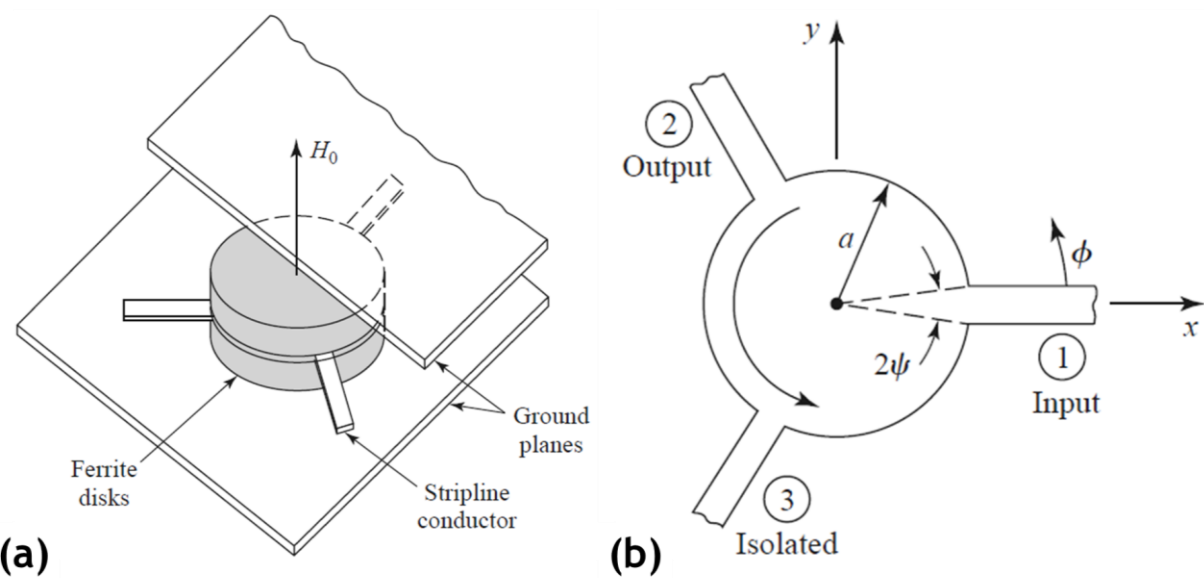

Figure 1.8: (a) Geometry of a stripline circulator. (b) Schematic of circulator operation. A wave entering from the input (port 1) only couples to one output port (port 2) and the last port is completely isolated (port 3). Figures from [52].

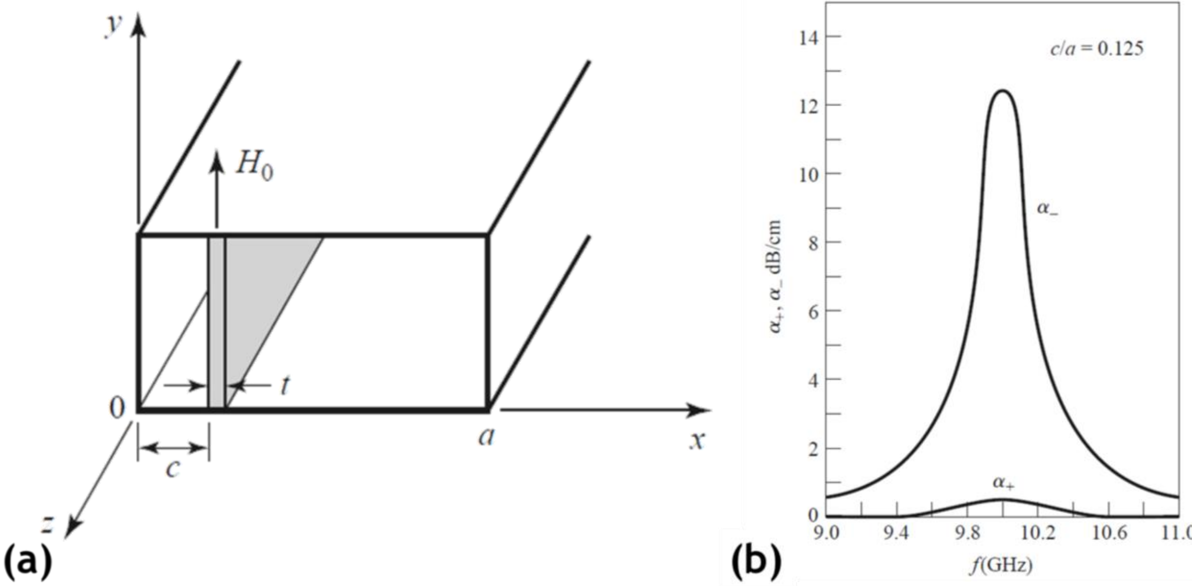

Figure 1.9: (a) Geometry of a nonreciprocal ferrite waveguide isolator. (b) Attenuation constant as a function of frequency for waves travelling in the forward and backward directions. Figures from [52].

magnetization is currently still an active area of research, the field of spintronics being one prominent example [54], [55].

1.2.2 Issues with Miniaturization

As system dimensions shrink, it has become very apparent that conventional magnetic devices cannot be miniaturized nearly as well as their electronic counterparts. For example, consider the transceiver module shown in Figure 1.10 [43]. The CMOS and MMIC circuits are each approximately the same size as the circulator, but the circuits are packed to the brim with components, while the circulator is just one single element. This is a recurring design problem for systems that rely on dynamic magnetization, the necessary magnetic devices require much larger footprints than the more streamlined electronics and limit the miniaturization of the entire system.

Magnetic devices cannot be practically miniaturized because they typically fall into at least one of the three following scenarios:

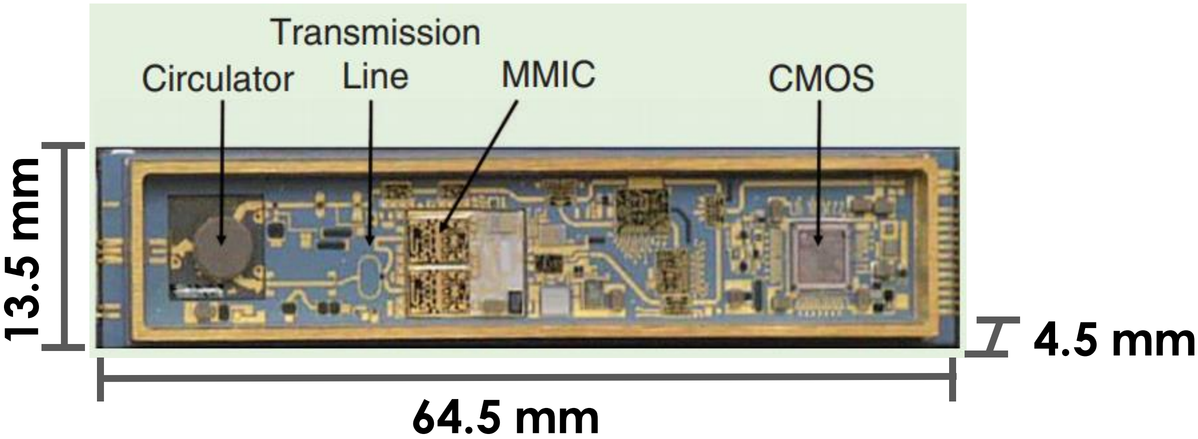

Figure 1.10: Transceiver module for an electronically scanned array radar. Adapted from [43].

1. Devices that require the use of ferrite materials because, at the time of writing, there has not been a commercially viable method to integrate ferrites onto semiconductor substrates [43], [53]. This necessitates the use of off chip magnetic components, limiting not only package size but the overall system efficiency because of the additional losses and noise from the wiring now needed to connect the external magnetic components.
2. Devices, such as loop antennas, transformers, and inductors, that rely on wire loops to generate the necessary magnetic fields for operation. When the dimensions of these loops shrink, the Ohmic losses associated with them begin to grow meaning that miniaturization comes at the cost of system efficiency.
3. Devices that couple electromagnetic waves directly to the dynamic magnetization, such as isolators and circulators. The size of these devices must be on par with the electromagnetic wavelength to have an appreciable effect on the wave. If these devices are miniaturized, the coupling strength decreases, and the devices can no longer operate as intended. As a result, when system miniaturization is the goal, alternative approaches are used to eliminate the need of these devices. Again using a transceiver as an example, to eliminate the possibility of collisions between received and

transmitted signals in a mobile transceiver without a circulator, techniques like frequency division duplexing and time division duplexing are typically employed [56]. However, this comes at the expense of the transceiver's data rate which again effectively lowers the system's efficiency. Attempts to make nonmagnetic circulators have been made [57]–[61], but these are all active devices and thus are a source of constant power drain on the system whereas magnetic circulators are completely passive.

From this list, it is evident that the fundamental mechanisms utilized for dynamic magnetic devices also prevent their miniaturization. To develop small-scale magnetic devices with dimensions that rival their electronic analogs, a new mechanism for the transduction of dynamic magnetization must first be established.

1.3 The Case for Dynamic Multiferroics

1.3.1 Research on Magneto-Acoustic Coupling

As discussed in Section 1.1.2, magnetostrictive materials are a class of materials where the magnetization couples to mechanical strains. Because of the large strains generated by these materials, they have been very successful in magnetically driven mechanical actuators in sonar transducers [37]. Using this concept in reverse, mechanical actuation can serve as an alternative method to generate dynamic magnetization. The speed of light is approximately 3×10^8 m/s, while the typical speed of an acoustic wave is approximately 3×10^3 m/s, meaning that, by utilizing acoustic waves instead of electromagnetic waves, the characteristic dimension of the magnetic devices can now be reduced by five orders-of-magnitude. There is a large amount of precedent to using this approach as mechanical resonators have been used

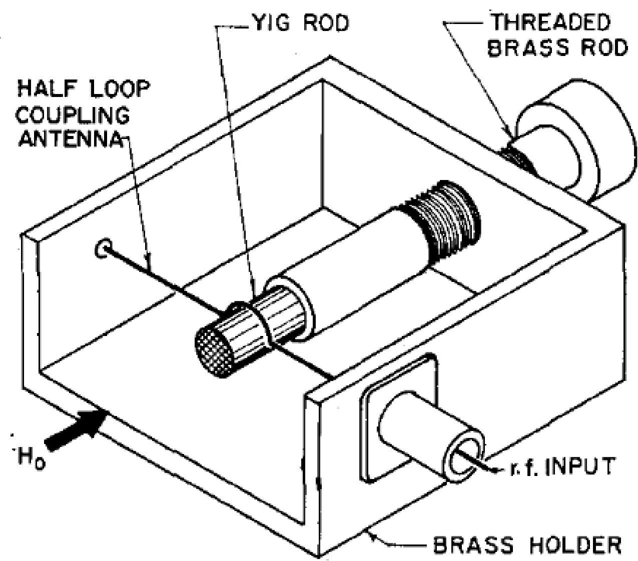

Figure 1.11: 1.05 GHz one-port magneto-acoustic delay line made with a single-crystal YIG rod with a diameter of 2.74 mm and length of 7.37 mm. Figure from [69].

in RF filters for decades because of their ability to achieve higher quality factors and smaller form factors than what is possible with traditional electronics [62], [63].

Early research on magneto-acoustic devices for RF applications was focused on the design of delay lines, where the relatively slow velocity of the acoustic waves allowed for much longer delays times than reasonably possible using an electromagnetic wave approach [64]–[71]. These devices used shorted fine-wire couplers to generate magnetic fields, which in turn transduce magneto-acoustic waves that propagate in the magnetic material (Figure 1.11). The waves are then sensed using the shorted couplers after a time delay that is set by the geometry of the sample. As was the case for the electromagnetic devices discussed in Section 1.2.1, coupling acoustic waves with the "rotation" of the dynamic magnetization introduces a number of unique aspects to the wave propagation, such as Faraday rotation and nonreciprocity [68], [72]. If the bias magnetic field is modulated (either temporally or spatially) additional processes, such as frequency conversion and pulse compression, have also been demonstrated [72], [73].

These devices required low acoustic losses, high resistivity, and low magnetic losses, making single crystal yttrium iron garnet (YIG) the de facto material in these systems [64], [67], [74]. Being limited to YIG proved to be a major limitation for the technology due to the difficulty in consistently machining the YIG single crystals into geometries that achieve the needed wave dispersion characteristics for delay lines [64], [66]. Similar to the case of magnetic thin films discussed in Section 1.1.2, the geometry of the sample dictates the internal forces within the magnetic material, which in turn influences the dynamics [64], [67], [68], [75]. The geometries that were consistently machinable lead to largely nonuniform internal fields in these devices, which lead to the non-ideal wave dispersion. Attempts to mitigate this by machining the YIG into cones instead of rods [76] or surrounding the device with magnetic flux guides [72], [74], [77], [78] to reshape the internal magnetic field were investigated but ultimately were unsuccessful. Eventually epitaxially grown thin films YIG on gadolinium gallium garnet (GGG) substrates were developed, which gave an alternative to the bulk machined single crystals. These thin films enabled the devices to have aspect ratios ideal for delay lines. However, by the time this was done, research on magneto-acoustic delay lines had largely stopped in favor of a purely magnetic approach [64], [66].

1.3.2 Radio Frequency Piezoelectric Devices

Leveraging magneto-acoustics alleviates the dependence on electromagnetic wavelength for the dynamic magnetic devices discussed in Section 1.2.1, but there are still other issues that impede miniaturization and integration. Shorted fine-wire couplers are used to generate and sense the acoustic waves in these devices, which means they are susceptible to the same issues with miniaturization of inductors discussed in Section 1.2.2. Miniaturization requires the use of some type of capacitive transducer as an alternative to generate the acoustic waves. To that end, dynamic multiferroic devices utilizing the strain-coupled composites discussed in Section 1.1.2 offer a solution to this dilemma.

To generate the strains needed for dynamic multiferroic devices, the strain-coupled composites can leverage the piezoelectric device geometries that have long been a staple of RF systems [44], [63]–[65], [79]–[88]. As was the case for magneto-acoustic devices, early RF applications of piezoelectricity focused on bulk acoustic wave delay (BAW) lines. Piezoelectric substrates were originally polished down to a thickness set by the operating frequency and mounted onto low loss crystal rods. Eventually, the target frequencies required piezoelectric thicknesses that surpassed what was possible through substrate polishing and spurred the development of deposition processes for piezoelectric thin films [63], [64]. With advances in microelectronics manufacturing, namely photolithography, the fabrication of patterned electrodes directly onto piezoelectric surfaces became possible and enabled the development of surface acoustic wave (SAW) delay lines [63], [89]. These manufacturing processes have all now, after years of development, culminated into three highly successful commercial piezoelectric products: quartz crystal oscillators (using substrate polishing), SAW filters (using surface patterning), and BAW filters (using piezoelectric thin films) [83]–[85], [90]–[92]. These three devices have become ubiquitous in modern mobile telecommunication systems, where large numbers of timing references and filters are necessary to support all the subsystems crammed into the electronics (albeit, piezoelectric clocks are now facing healthy competition from silicon-based oscillators [93]–[95]).

Radio frequency micro-scale piezoelectric devices remain an active field of research today. With the unique properties of thin film aluminum nitride being an enabling factor for BAW duplexers at GHz frequencies [83], a large body of research has been devoted to studying other types of resonant modes possible in the material to enable filters at lower frequencies (Figure 1.12), such as contour modes [96]–[98], Lamb modes [99], [100], and cross-sectional Lamé modes [101], [102]. Alternative materials are also being investigated, using both thin film deposition (aluminum scandium nitride (AlScN) [103], [104], lead zirconate titanate (PZT) [105]-

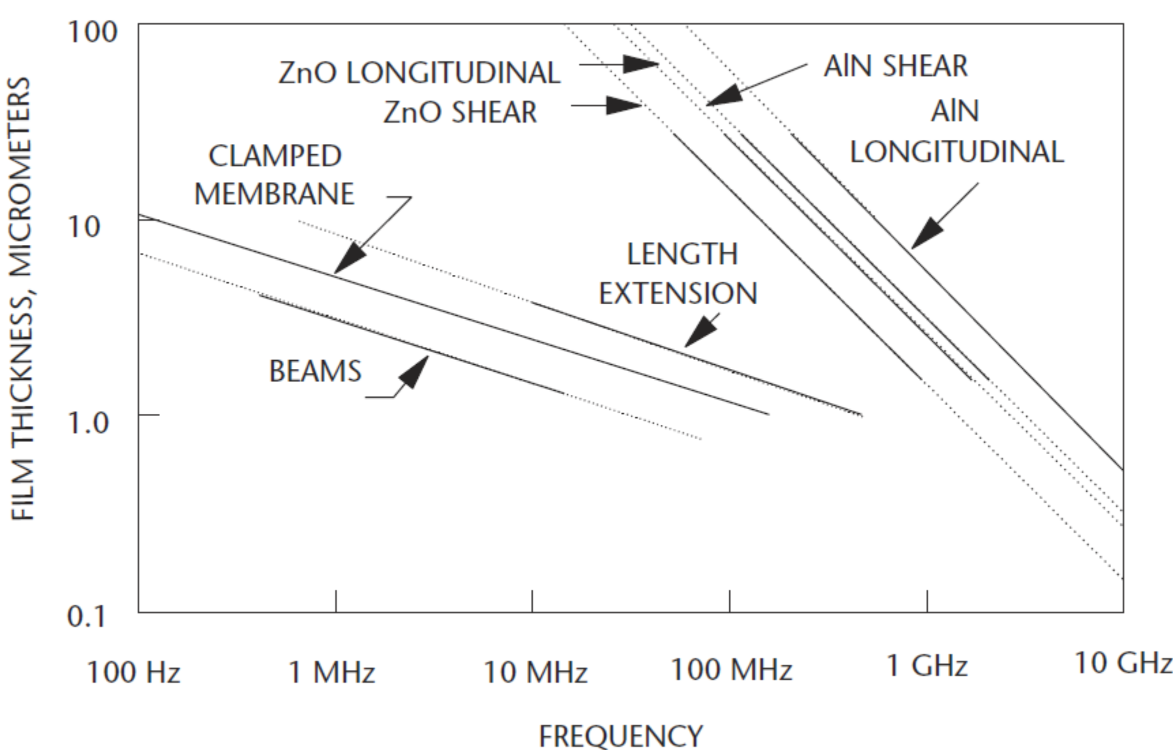

Figure 1.12: Approximate film thicknesses as a function of frequencies for different types of resonant modes. Width or Length to thickness ratio of 10:1 is assumed. Figure from [63].

[108], and barium strontium titanate (BST) [109], [110]) and substrate polishing (lithium niobate ($LiNbO_3$) [111]-[115]), with the intent of leveraging unique aspects of these materials. Piezoelectric materials with ferroelectric properties (PZT, $LiNbO_3$, and BST) can be tuned with an applied DC voltage. Materials with higher piezoelectric coupling and permittivity (AlScN, PZT, and $LiNbO_3$) would enable smaller devices at lower frequencies and wider filtering bandwidths. Manufacturing of piezoelectric filters for future 5G systems (6 GHz – 40 GHz) remains a tall order, so research on high frequency filtering has been focused on efficiently transducing higher harmonics of lower frequency resonators [116], [117]. Besides filtering, micro-scale piezoelectric devices have been applied to a large number of other RF applications: transformers [118]–[120], power transfer [121]–[123], ultrasonic transducers [103], [124]–[126], oscillators [127]–[129], switches [108], [130], [131], nonreciprocal devices [57]–[59], and acoustic transmission line devices [132]–[136]. Additional functionality can be achieved by

strain-coupling the piezoelectric layer to another material system, yielding new classes of devices such as acousto-electric devices [137]–[140], optomechanical devices [141], harsh environment compatible devices [142]–[144], and many types of sensors [145]–[148]. In addition to the large body of experimental work already discussed, there has also been a great deal of theoretical research on the design of micro-scale RF piezoelectric devices [80], [149]–[159].

1.4 Research in Dynamic Multiferroics

1.4.1 Current State of the Art

Summarizing what has been discussed thus far:

1. Strain-coupled multiferroics offer a unique way to efficiently control magnetism at small scales by using electric fields.
2. Dynamic magnetic devices are widely used in RF systems but cannot be miniaturized due to their reliance on inductors and electromagnetic waves.
3. Magneto-acoustic devices can be miniaturized using elastic waves but lacked the technology for micro-scale transducers at the time.
4. Micro-scale RF piezoelectric devices are well established and strain-coupling these devices to other material systems for new functionality has already been demonstrated.

With the large amount of present-day work on quasi-static strain-coupled multiferroics and on piezoelectric resonators, it is now the proper time to revisit the magneto-acoustics work of the past to achieve miniaturized RF magnetic devices in the near future. Through strain-coupling RF piezoelectric devices with magnetostrictive thin films, dynamic multiferroic coupling has the potential to achieve the same functionality at the micro-scale as the macro-scale magnetic devices discussed in Section 1.2.1.

Quasi-dynamic multiferroic coupling has been demonstrated in several devices to date. As opposed to true dynamic coupling, where the electric and magnetic fields coupled through the multiferroic composite both vary with time, in quasi-static coupling one of the fields is static. Most commonly, these devices utilize the ΔE-effect, where the Young's modulus of the magnetostrictive material is dependent on the DC magnetic field. This approach has been used to make magnetic field sensors [17]–[19], tunable piezoelectric resonators [24], [25], and tunable SAW delay lines [26]–[28]. By using this approach in conjunction with phase lock loop (PLL), it has been proposed that this type of structure could work as a wide band antenna [160]. As the magnetic field varies slowly (relative to the device frequency and PLL response time), the ΔE-effect induces a shift in resonance frequency. The device is then forced into resonance by the PLL circuit, and this new resonance frequency is used to measure the time-dependent magnetic field amplitude. Quasi-dynamic coupling has also been used to make electric field tunable devices, where the DC electric field creates a static strain in the magnetic layer, effectively acting as a DC bias field and altering the magnetization dynamics. This is mostly used to shift the magnetic resonance frequency within the film (as opposed to a mechanical resonance), which can be useful for tunable electromagnetic filters [161]–[163].

A major push in dynamic multiferroics has come from various research communities interested in wireless transduction. One such community is the field of energy harvesting and power transfer [164]–[166]. Conventional wireless power technology utilizes magnetic fields and inductive coupling [167], [168]. Multiferroic devices lend themselves well to these systems as they also couple to magnetic fields, with the added advantage that mechanical resonators have much higher quality factors than what is achievable with inductors. If this operation is run in reverse, where an electric field is applied to the multiferroic sample to create a dynamic magnetic field, these devices may be used as multiferroic antennas (Figure 1.13) [10]–[12]. The major advantage here is that, since elastic waves travel much slower than electromagnetic

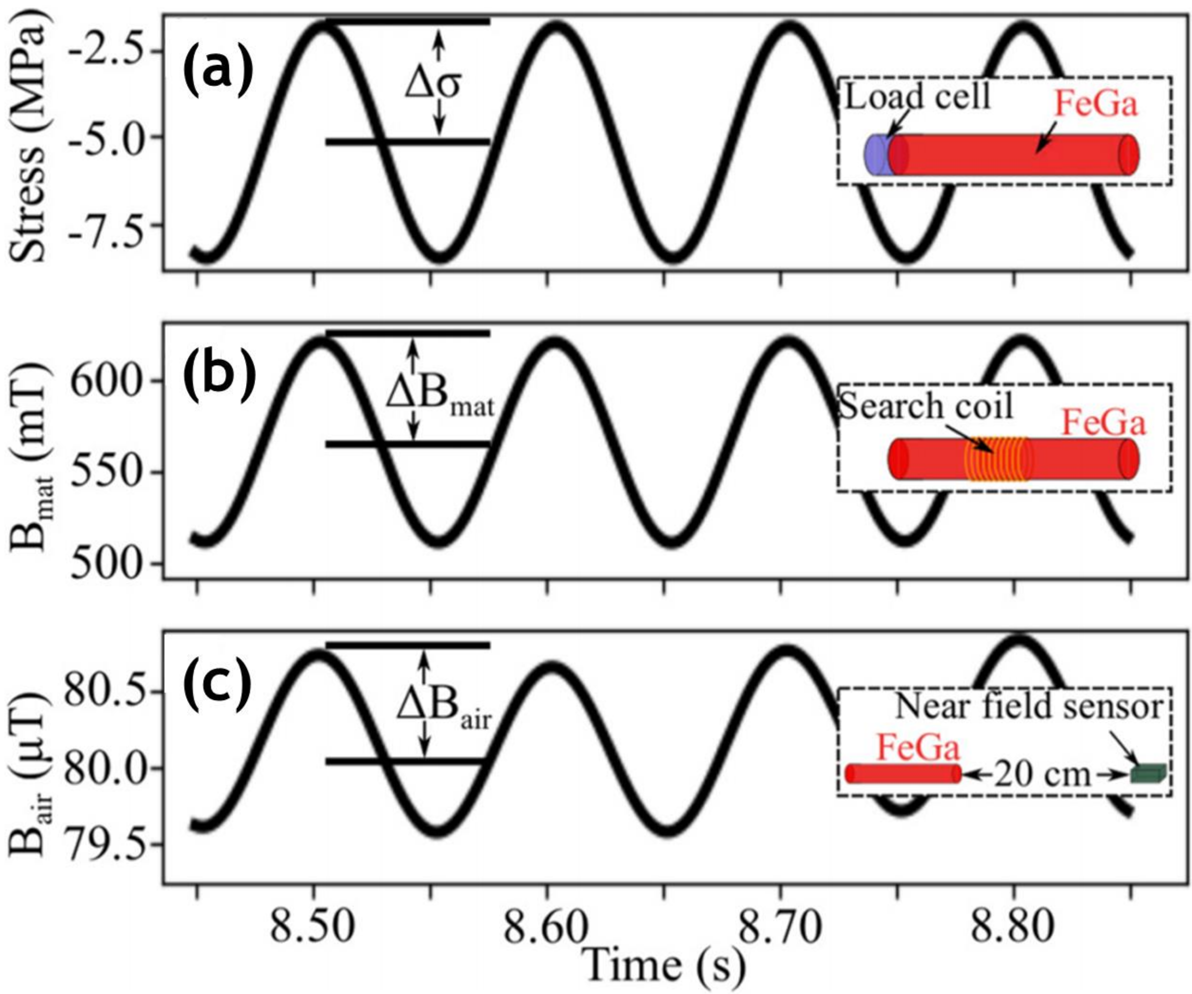

Figure 1.13: Time response of a multiferroic near-field coupler. (a) Strain applied by the piezoelectric transducer. (b) Magnetic flux density within the magnetic material. (c) Generated magnetic flux density measured 20 cm away. Figure from [12].

waves (as discussed in Section 1.3.1), multiferroic resonators can be made with much smaller dimensions than conventional antennas. Achieving resonance in a smaller size means that high amplitudes of electromagnetic fields can be generated without the need of a bulky matching network [169]. This is particularly advantageous for near field communication systems, which already require electrically-small antennas and predominately use magnetic fields (as they penetrate deeper into typical lossy media) [170]. However, characterization of radiated signals from micro-scale multiferroic devices remain elusive due to the weakness of the signal

compared to parasitic radiation from the characterization equipment, with no conclusive measurements made to date [11], [171], [172].

Researchers interested in high frequency dynamic multiferroic coupling are predominantly focused on the coupling of acoustic waves with dynamic magnetization. The most well-known experiments in the field are those of acoustically driven ferromagnetic resonance (ADFMR) done by Labanowski et al. [173] and Dreher at al. [174]. In these experiments, SAW devices are used to generate acoustic waves that travel through a nickel thin film, exciting ferromagnetic resonance (FMR) when the acoustic wave frequency matches the FMR frequency (Figure 1.14). The key takeaway from these experiments is that the multiferroic coupling maximizes when the magnetization is oriented 45 degrees from the acoustic wave direction, a nuance not seen in electromagnetic coupling with magnetic materials. Work later done by Nygren et al. extends this result by measuring damping of the magnetization as a function of length along the sample [175]. It was found that the decay length of the magnetization in these systems are much longer than that of spin waves driven by magnetic fields. This result is key because conventional dynamic magnetic devices require ferrites, as

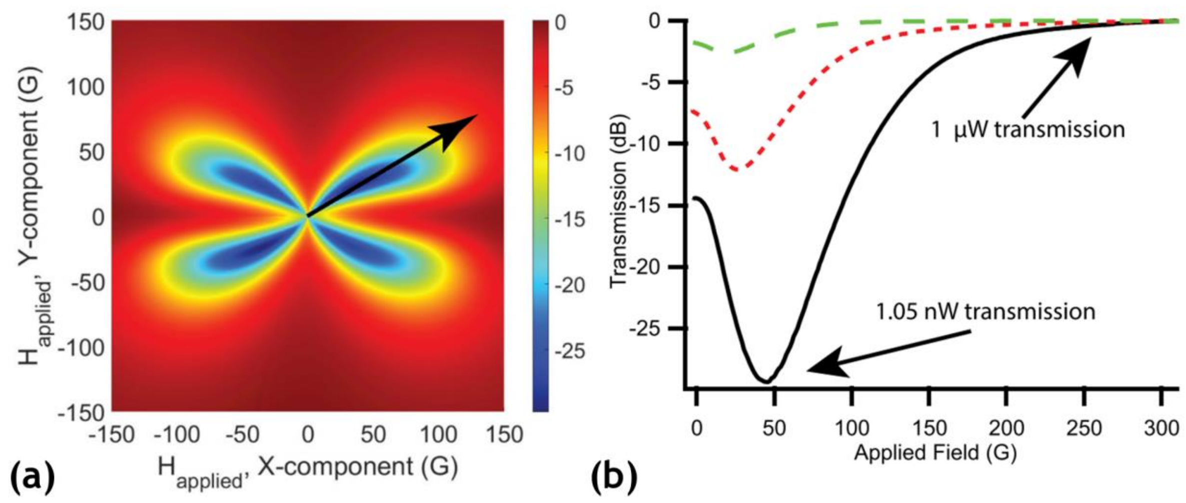

Figure 1.14: (a) Power absorption of ADFMR as a function of magnetic bias in the x and y directions. Maximal coupling is approximately 45 degrees. (b) Power absorption along the direction of the arrow shown in (a) at different bias magnetic fields. Figures from [173].

discussed in Section 1.2.2, to minimize eddy current damping of the electromagnetic signal. Ferrites are difficult to integrate on chip so, since the damping is lower using acoustic actuation, the ability to use conductive magnetic materials through strain-coupled multiferroics makes miniaturization much more practical. Experiments by other groups have utilized similar approaches to demonstrate a number of unique dynamic effects, such as parametric amplification [176], magnetization reorientation [177]–[180], nonreciprocity [181]–[183], coupled magneto-acoustic resonances [184]–[186], and reverse spin wave doppler shift [187].

Dynamic multiferroic devices are complicated systems, coupling electromagnetics, acoustics, and dynamic magnetization. Because of this complexity, accurate modelling of these systems is a difficult task in its own right. Approximate methods have used analytical [170], [188] and finite element approaches [189], but the only fully coupled model developed thus far has been for resonant BAW multiferroic antennas using the FDTD method by Yao et al. [190], [191]. The major challenge is that the characteristic length scales for the magnetization dynamics and acoustics are much smaller than that of the electromagnetics. This requires much longer computation times than necessary because of the stability condition of the FDTD algorithm for wave problems [191]. The work presented in [190], [191] bypasses this issue by specifically using an ADI-FDTD algorithm.

1.4.2 Contributions of This Work

As discussed above, dynamic multiferroic coupling is a new field with the potential to finally realize energy efficient micro-scale RF magnetic devices. The goal of this work is to contribute to the field by investigating the nuances of dynamic multiferroics in three specific regimes. The remainder of this thesis is organized as follows. First, in Chapter 2 the theoretical foundation of dynamic magnetization coupling is discussed, and the different regimes of coupling are defined. Chapter 3 then discusses quasi-static coupling in multi-domain resonators,

focusing on nonlinear forces arising from magnetostriction. Chapter 4 discusses coupling in the spin precession regime in multi-domain resonators. And finally, Chapter 5 discusses coupling above the spin precession regime in a single domain magnetic film.

Chapter 2 Dynamics of Magnetization

2.1 Features of Ferromagnetic Materials

Ferromagnetic materials are ubiquitous in modern society, being integral components of motors, transformers, actuators, and many other applications [37], [70], [71], [192], [193]. The defining feature of these materials is that their permeability is hysteretic, meaning that the permeability is not only nonlinear but depends on the exact sweep of the applied bias magnetic field. Hysteresis loops of the average material magnetization versus the applied bias, such as Figure 2.1, are used to characterize these materials.

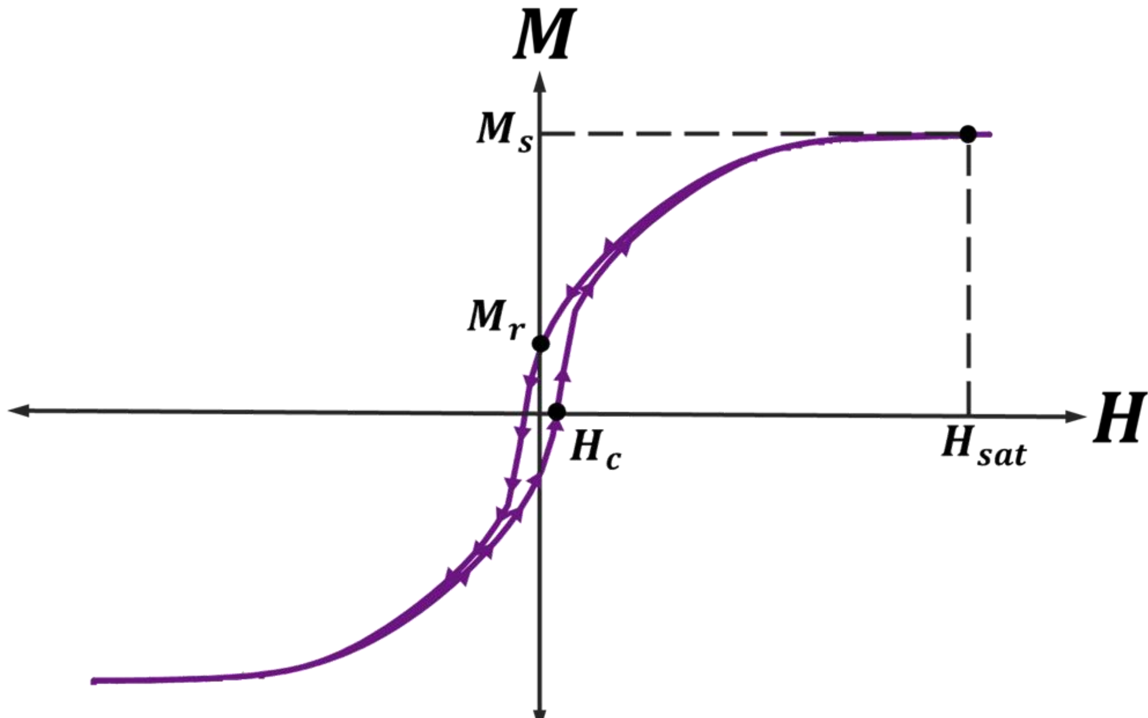

Figure 2.1: Sample hysteresis loop of a ferromagnetic material.

There are four key aspects of the material that can be determined from these curves:

1. The remanent magnetization (M_r), which is the absolute value of the magnetization at zero applied bias field.
2. The coercive field (H_c), which is the absolute value of the applied field at which point the total magnetization is zero.
3. The saturating field (H_{sat}), which is the absolute value of the applied field at which the magnetization throughout the material is uniformly aligned. In practice, due to thermal fluctuations, complete saturation is impossible so an approximate H_{sat} is defined.
4. The saturation magnetization (M_s), which is the value of the magnetization measured at saturation. Again, due to thermal fluctuations this is technically impossible to measure. This value can be taken as what the magnetization asymptotically approaches as the applied magnetic field continues to increase in magnitude.

The signs of these values depend on the direction of the magnetic field sweep, which is indicated by the arrows in the plot. The constitutive law for a ferromagnetic material is thus a nonlinear function of applied magnetic field and is given below in SI units.

$$\underline{B} = \mu_0 \left[\underline{M}(\underline{H}) + \underline{H} \right] \tag{2.1}$$

To put the constitutive laws in a form similar to linear magnetic materials, the above equation can be cast into the following piecewise formulation:

$$\underline{M}(\underline{H}) = \underline{\underline{\chi_{eff}}}(\underline{H})\underline{H} \tag{2.2}$$

$$\underline{B} = \begin{cases} \mu_0 \left[\underline{\underline{\chi_{eff}}}(\underline{H})\underline{H} + \underline{H} \right] & |\underline{H}| < H_{sat} \\ \mu_0 \left[M_s \hat{\underline{H}} + \underline{H} \right] & |\underline{H}| \geq H_{sat} \end{cases} \tag{2.3}$$

The instantaneous susceptibility of the material for small changes in applied field is the local slope of the hysteresis loop at the applied magnetic field.

$$b = \mu_0 \left[\frac{\partial M}{\partial H} h + h \right] \tag{2.4}$$

Inside a ferromagnetic material is a collection of individual magnetic dipoles whose orientation is determined by random thermal fluctuations, various local interactions in the material, and any external magnetic fields [192]. Typically, the magnetic dipoles inside the material form into conglomerations called domains, as shown in Figure 2.2. Within each domain, all the magnetic dipoles are uniformly arranged. The narrow zone in between two domains is called a domain wall and in this area the magnetization has a gradient as it transitions between the uniform orientation of one domain to the next. When a magnetic field is applied, at low fields the net magnetization change is predominantly determined by the movement of these domain walls, as shown in Figure 2.2b. The domain walls are highly mobile and are responsible

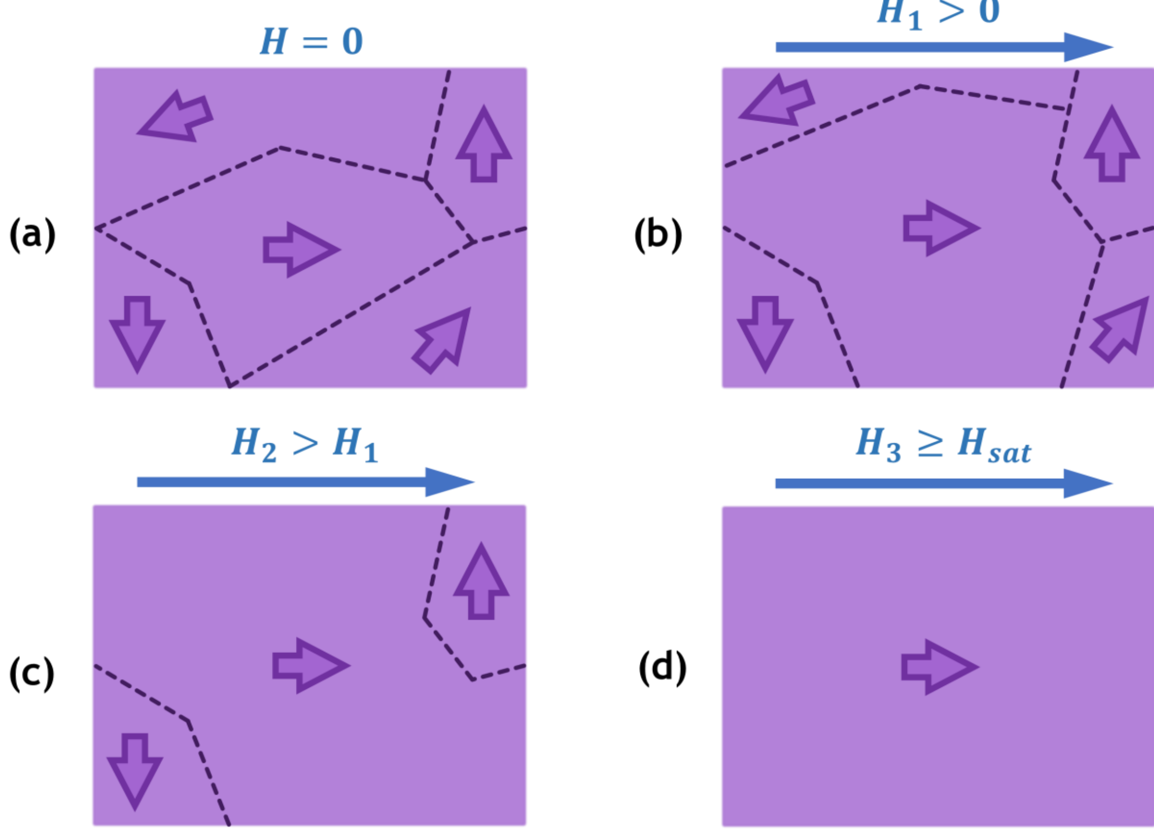

Figure 2.2: Transformation of domain structure under applied magnetic fields. Domain walls are represented by dashed lines. (a) Multi-domain state at no applied field. (b) Domain wall motion expanding domains parallel to field. (c) High fields with only domains orthogonal to applied field left. (d) Completely saturated sample.

for the portions of the hysteresis loop with large instantaneous susceptibility. At higher fields, the magnetization changes are caused by rotation of the magnetic dipoles within the last few domains that still exist in the material (Figure 2.2c). These domains are usually magnetized orthogonally to the applied field. Much smaller changes are generated this way, and this is responsible for the low instantaneous susceptibility as the material approaches saturation. Past saturation (Figure 2.2d), no changes in magnetization is possible as all the magnetic dipoles within the material are already completely aligned. If the dimensions of the material approach the sizes of the magnetic domains, interesting formations can occur as well [22], [194]–[197].

In addition to ferromagnetic materials, there are two other classes of magnetic compounds that are heavily used in dynamic systems [41]–[43], [198]. Ferrimagnetic materials are compounds very similar to ferromagnetic materials, with the key difference being that ferrimagnetic materials are made of at least two types of antiparallel magnetic dipoles at the atomic scale. As shown in Figure 2.3b, these two dipoles are antiparallel but are unequal in magnitude, meaning that there is still a net magnetization. Magnetic materials in many radio frequency applications use ferrimagnetic materials because they are often insulating, meaning that eddy current losses generated by the electromagnetic waves are not an issue [41]–[43].

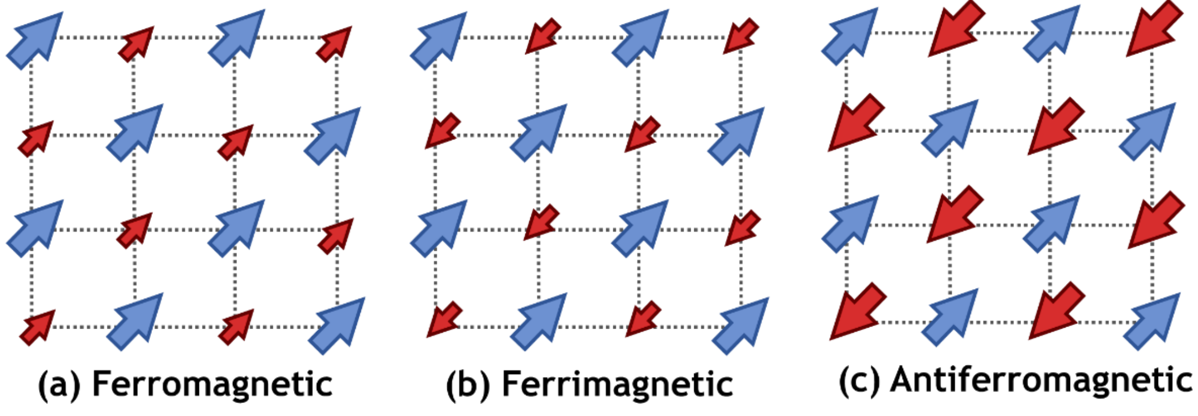

Figure 2.3: (a) Ferromagnetic compound with approximately parallel dipoles. (b) Ferrimagnetic material with unequal and antiparallel dipoles. (c) Antiferromagnetic material with equal and antiparallel dipoles.

When modelling these materials, typically the net magnetization is used, and any atomic scale variation is ignored. In the specific case where the different magnetic dipoles sum to a zero net magnetization (Figure 2.3c), the material is called antiferromagnetic [198]. Due to the internal dynamics specific to antiferromagnets, they hold promise for future terahertz systems.

2.2 Dynamics of Magnetization

2.2.1 Dynamics of a Single Magnetic Moment

The complications of magnetization dynamics trace their roots to the fact that the source of magnetization is the atomic angular momentum. The total angular momentum of an atomic site ($\underline{\mathcal{J}}$) in a material is the sum of two contributions, the orbital angular momentum ($\underline{\mathcal{L}}$) and the spin angular momentum ($\underline{\mathcal{S}}$), as shown in Figure 2.4. While in general both contributions matter, in practice the contribution of the spin angular momentum dominates, and the orbital moment can be ignored.

Following the derivation in [52], the magnetic moment ($\underline{\mathfrak{m}}$) is related to the atomic spin by the following equation:

$$\underline{\mathfrak{m}} = -\gamma \underline{\mathcal{S}} \tag{2.5}$$

where, γ is the gyromagnetic ratio. If a magnetic field ($\underline{H}$) is applied to the dipole, it experiences the torque given by Equation 2.6.

$$\underline{\Gamma} = \underline{\dot{\mathcal{S}}} = \underline{\mathfrak{m}} \times \underline{B} = \mu_0 \underline{\mathfrak{m}} \times \underline{H} \tag{2.6}$$

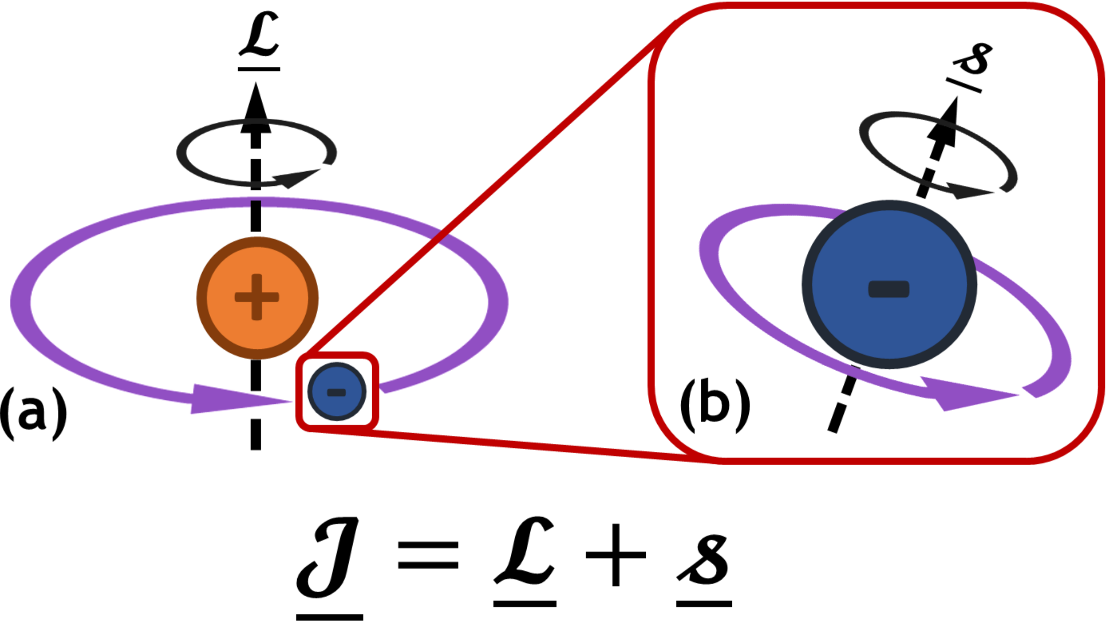

Figure 2.4: Contributes to total angular momentum, $\underline{\mathcal{J}}$: (a) orbital angular momentum, $\underline{\mathcal{L}}$, from the electron circling the nucleus and (b) spin angular momentum, $\underline{\mathcal{S}}$, that is intrinsic to the electron.

Now combining Equations 2.5 and 2.6, the equation of motion for a single spin is found to be to be Equation 2.7.

$$\dot{\underline{\mathfrak{m}}} = -\mu_0 \gamma \underline{\mathfrak{m}} \times \underline{H} \tag{2.7}$$

Assuming the density of magnetic dipoles per unit volume is $\rho_{\mathfrak{m}}$, then the magnetization is defined by the following equation:

$$\underline{M} = \rho_{\mathfrak{m}} \cdot \underline{\mathfrak{m}} \tag{2.8}$$

and the new equation of motion for the volume magnetization is now given below.

$$\dot{\underline{M}} = -\mu_0 \gamma \underline{M} \times \underline{H} \tag{2.9}$$

By the equation above, no torque is exerted on the magnetization if it is parallel to the magnetic field. When a magnetic field is at an angle to the magnetization, the magnetization will rotate until it is parallel to the magnetic field, at which point the magnetization stops changing and is now in DC equilibrium. If a dynamic field is applied that is smaller than the DC

magnetic field, the magnetization then only slightly moves away from the DC equilibrium point. Modelling of the dynamics becomes much simpler in this approximation as the equation can be "centered" around the DC equilibrium point. The total magnetic field and magnetization is now defined by the following two relations:

$$\underline{M} = \underline{M_0} + \underline{m} = M_s\underline{\widehat{M_0}} + \underline{m} \tag{2.10}$$

$$\underline{H} = H_0\underline{\widehat{M_0}} + \underline{h} \tag{2.11}$$

where $\underline{m}$, $\underline{h}$, $\underline{M_0}$, $\underline{\widehat{M_0}}$, and H_0 are the AC magnetization, the AC magnetic field, DC magnetization, direction of the DC magnetization, and the DC magnetic field magnitude, respectively. Taking into account the fact that the DC equilibrium values, by definition, do not change in time, substituting Equations 2.10 and 2.11 into Equation 2.9 yields the equation below.

$$\underline{\dot{m}} = -\mu_0\gamma\left[\left(\underline{m} \times H_0\underline{\widehat{M_0}}\right) + \left(M_s\underline{\widehat{M_0}} \times \underline{h}\right) + \left(\underline{m} \times \underline{h}\right)\right] \tag{2.12}$$

Taking a time derivative of Equation 2.12 yields the following second order differential equation:

$$\begin{aligned}\underline{\ddot{m}} &= -\mu_0\gamma\left[-\left(H_0\underline{\widehat{M_0}} \times \underline{\dot{m}}\right) + \left(M_s\underline{\widehat{M_0}} \times \underline{\dot{h}}\right) + \frac{d}{dt}\left(\underline{m} \times \underline{h}\right)\right] \\ &= -\left[\omega_0^2\left(\underline{m} - \left(\underline{m} \cdot \underline{\widehat{M_0}}\right)\underline{\widehat{M_0}}\right)\right] + \left[\omega_0\omega_M\left(\underline{h} - \left(\underline{h} \cdot \underline{\widehat{M_0}}\right)\underline{\widehat{M_0}}\right)\right] - \left[\omega_M\left(\underline{\widehat{M_0}} \times \underline{\dot{h}}\right)\right] \\ &\quad - \left[(\mu_0\gamma\omega_0)\underline{\widehat{M_0}} \times \left(\underline{m} \times \underline{h}\right)\right] - \left[\mu_0\gamma\frac{d}{dt}\left(\underline{m} \times \underline{h}\right)\right]\end{aligned} \tag{2.13}$$

$$= -\left[\omega_0^2\left(\underline{m} - \left(\underline{m} \cdot \underline{\widehat{M_0}}\right)\underline{\widehat{M_0}}\right)\right] + \left[\omega_0\omega_M\left(\underline{h} - \left(\underline{h} \cdot \underline{\widehat{M_0}}\right)\underline{\widehat{M_0}}\right)\right] - \left[\omega_M\left(\underline{\widehat{M_0}} \times \underline{\dot{h}}\right)\right] \tag{2.14}$$

Here $\omega_0 = \mu_0\gamma H_0$ and $\omega_M = \mu_0\gamma M_s$. The difference between Equation 2.13 and 2.14 is that in 2.14 a small signal approximation is applied ($|\underline{m}| \ll M_s$ and $|\underline{h}| \ll H_0$) so the term $\underline{m} \times \underline{h}$ is assumed to be negligibly small. This has the effect of linearizing the equation, so that the frequency of the magnetization will now be the same as the frequency of the applied field.

Examining Equation 2.14 can provide two major insights into the dynamics of an independent spin. The first term contains the expression $\left(\underline{m} - \left(\underline{m} \cdot \underline{\widehat{M_0}}\right)\underline{\widehat{M_0}}\right)$, which subtracts the component of $\underline{m}$ parallel to the DC magnetization direction. This means that if there is any change in magnetization along the $\underline{\widehat{M_0}}$, it has a minimal effect on the torque felt by the magnetization. A similar expression is present in the second term for the AC magnetic field, $\left(\underline{h} - \left(\underline{h} \cdot \underline{\widehat{M_0}}\right)\underline{\widehat{M_0}}\right)$, meaning that any AC magnetic fields parallel to the $\underline{\widehat{M_0}}$ direction will also have minimal effect. AC magnetization and AC magnetic fields parallel to the $\underline{\widehat{M_0}}$ direction are responsible for nonlinear processes, which are ignored in the small signal approximation used in Equation 2.14 [71]. In the linear problem considered here, only AC fields applied perpendicular to $\underline{\widehat{M_0}}$ have any effect, and the magnetization change generated is also only perpendicular to $\underline{\widehat{M_0}}$.

2.2.2 Effective Fields

Thus far, only the effect of a magnetic field on a spin has been considered. But within a material there are several types of micro-magnetic interactions that can drive a spin, as summarized in Figure 2.5. These interactions all generate their own torques on the magnetic dipole and the sum of these is what determines the dynamics.

Calculating the torque for each of these interactions is feasible, however it is troublesome given that several equations have previously been derived assuming an applied magnetic field, such as the equations derived in Section 2.2.1, which would no longer be of any use. The effective field is a method that uses the energy densities of the different micro-magnetic interactions (U_{MM}) and derives what the field would be if this energy was due to a magnetic field ($\underline{H}_{MM}$) [70], [71], [193].

$$H_{MM} = -\frac{1}{\mu_0}\left(\frac{\partial}{\partial M_x}\hat{x} + \frac{\partial}{\partial M_y}\hat{y} + \frac{\partial}{\partial M_z}\hat{z}\right)\cdot U_{MM} + \sum_{p=x,y,z}\frac{\partial}{\partial p}\left[\frac{\partial U_{MM}}{\partial(\partial \underline{M}/\partial p)}\right] \qquad (2.15)$$

With these effective magnetic fields, the previously derived equations of motion can still be used. However, one important caveat is that these fields are not real and thus do not factor into Maxwell's equations. As an example, the effective field generated by a strain in a magnetostrictive material will reorient a spin. But a spin outside of the material will not feel any effective field caused by the strain. What it will feel is the magnetic field generated by the material, as magnetic fields generated by spins are real magnetic fields and can affect each other (which will be discussed in Section 2.3.1).

2.2.3 Modifications for a Continuum

The problem considered in Section 2.2.1 is for independent spins in a material. However, as discussed in Section 2.2.2, in a continuum there are a variety of internal micro-magnetic interactions between the spins that alter the dynamics. Using the effective field approach

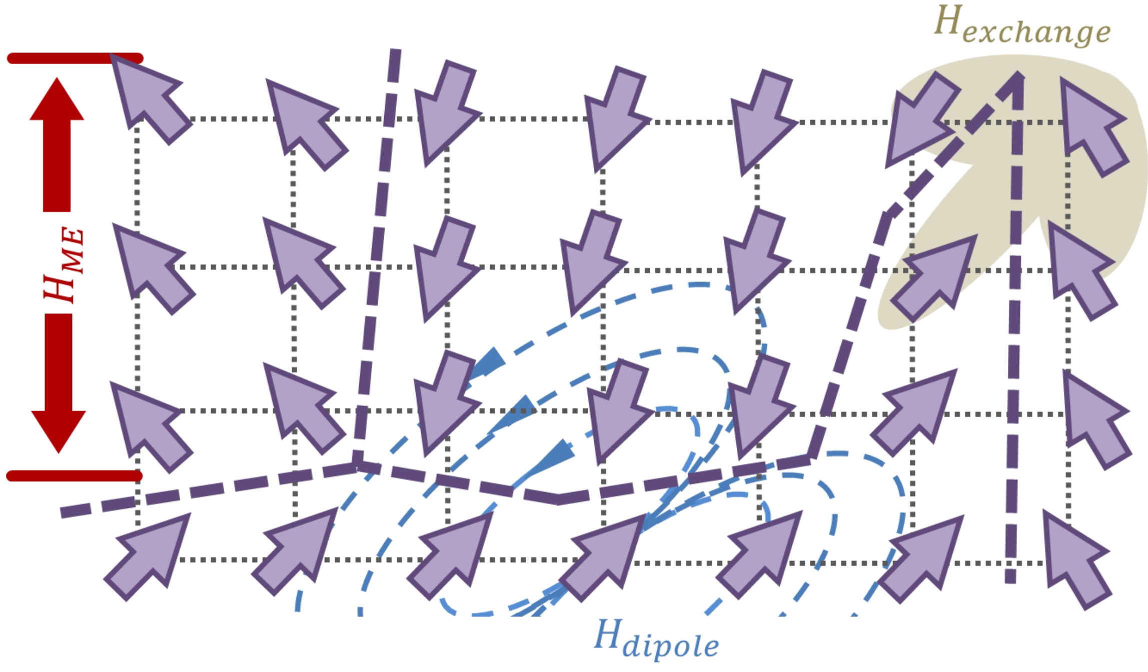

Figure 2.5: Types of micro-magnetic interactions present in an amorphous ferromagnetic material. These are discussed in depth in Section 2.3. Notice that the material is broken up into several domains.

discussed in Section 2.2.2, Equation 2.14 can simply be modified by replacing the magnetic field term with a sum of the internal and external magnetic fields, both real and effective.

$$\underline{H} = H_0\underline{\widehat{M_0}} + \underline{h}_{MM} + \underline{h}_{ext} \tag{2.16}$$

In this expression H_0 is the sum of the DC internal and applied fields, $\underline{h}_{MM}$is the sum of all AC internal magnetic fields, and $\underline{h}_{ext}$ is the AC external magnetic field. As shown in Figure 2.2, inside of a magnetic material the magnetization can vary as a function of space, meaning that the variables H_0, $\underline{\widehat{M}_0}$, $\underline{m}$, $\underline{h}_{MM}$, and $\underline{h}_{ext}$ can all vary as a function of space as well. To be completely accurate, these terms should truly be written as $H_0(\underline{x})$, $\underline{\widehat{M_0}}(\underline{x})$, $\underline{m}(\underline{x})$, $\underline{h}_{MM}(\underline{x})$, and $\underline{h}_{ext}(\underline{x})$ to indicate they are a function of position. However, to keep notation uncluttered, this will be omitted throughout this text.

Inserting Equation 2.16 into Equation 2.14 gives the following second order differential equation for the magnetization dynamics within the system.

$$\begin{aligned}\underline{\ddot{m}} = -\left[\omega_0^2\left(\underline{m} - \left(\underline{m}\cdot\underline{\widehat{M_0}}\right)\underline{\widehat{M_0}}\right)\right] + \left[\omega_0\omega_M\left(\underline{h}_{MM} - \left(\underline{h}_{MM}\cdot\underline{\widehat{M_0}}\right)\underline{\widehat{M_0}}\right)\right] \\ - \left[\omega_M\left(\underline{\widehat{M_0}}\times\underline{\dot{h}}_{MM}\right)\right] + \left[\omega_0\omega_M\left(\underline{h}_{ext} - \left(\underline{h}_{ext}\cdot\underline{\widehat{M_0}}\right)\underline{\widehat{M_0}}\right)\right] \\ - \left[\omega_M\left(\underline{\widehat{M_0}}\times\underline{\dot{h}}_{ext}\right)\right]\end{aligned} \tag{2.17}$$

As this is a linear second order differential equation, insight can be gained by writing the equation as if it was a mass-spring system.

$$\begin{aligned}\underbrace{\underline{\ddot{m}}}_{Inertial\ Term} + \\ \underbrace{\left\{\left[\omega_0^2\left(\underline{m} - \left(\underline{m}\cdot\underline{\widehat{M_0}}\right)\underline{\widehat{M_0}}\right)\right] - \left[\omega_0\omega_M\left(\underline{h}_{MM} - \left(\underline{h}_{MM}\cdot\underline{\widehat{M_0}}\right)\underline{\widehat{M_0}}\right)\right] + \left[\omega_M\left(\underline{\widehat{M_0}}\times\underline{\dot{h}}_{MM}\right)\right]\right\}}_{Restoring\ Force\ Term} \\ = \underbrace{\left\{\left[\omega_0\omega_M\left(\underline{h}_{ext} - \left(\underline{h}_{ext}\cdot\underline{\widehat{M_0}}\right)\underline{\widehat{M_0}}\right)\right] - \left[\omega_M\left(\underline{\widehat{M_0}}\times\underline{\dot{h}}_{ext}\right)\right]\right\}}_{Driving\ Force\ Term}\end{aligned} \tag{2.18}$$

The first term represents a local inertial term, similar to the acceleration term in a mass-spring system. The second term is a restoring force term, which is a complicated expression of the internal fields, equilibrium magnetization, and AC magnetization. An effective spring constant could be derived for a given domain structure, similar to how a modal spring constant in an elastic structure depends on the materials present and the boundary conditions. The external force term depends on the distribution of the external field, similar to how a distributed load will drive a cantilever differently than a point load. With all the similarities present between Equation 2.18 and a mass-spring system, it should be of no surprise that a magnetic material has internal resonances that can be driven by applied magnetic fields, and that these internal resonances depend on the applied fields and equilibrium domain structure. These will be discussed more in depth in Sections 2.4.3 and 2.4.2, as well as Chapter 4 and Chapter 5.

2.3 Interactions Within an Amorphous Ferromagnet

2.3.1 Dipolar Interactions

A spin in a magnetic material is a magnetic dipole, meaning that it generates its own magnetic field. This magnetic field is felt by every other spin in the system, which are all generating their own magnetic fields as well. The magnetic fields generated by each spin (called dipolar fields) exert a force on all the other spins in the system, a phenomenon known as the dipolar interaction.

The dipole field is a real magnetic field and thus requires a simultaneous solution to Maxwell's equations in addition to Equation 2.18, which greatly complicates the analysis [190], [191]. Since magnetic devices are often much smaller than the electromagnetic wavelength of their operation frequency, the wave dynamics can be ignored and the magnetostatic

approximation can be taken. In this approximation it is assumed that $\underline{\nabla} \times \underline{H} \approx 0$, meaning that there is no radiation and that the magnetic field can be defined as a gradient of a magnetostatic potential, $\phi(\underline{x})$. In this approximation, the total dipolar field distribution can be found by summing the contributions of the magnetization throughout the material and is given by the following two equations [192].

$$\underline{H}_{dipole}(\underline{x}) = -\underline{\nabla}\phi(\underline{x}) \tag{2.19}$$

$$\phi(\underline{x}) = -\frac{1}{4\pi}\int_{\mathbb{V}} \frac{\underline{\nabla}' \cdot \underline{M}(\underline{x}')}{|\underline{x} - \underline{x}'|} d^3\underline{x}' + \frac{1}{4\pi}\int_{\mathbb{S}} \frac{\underline{M}(\underline{x}') \cdot \underline{\hat{n}}}{|\underline{x} - \underline{x}'|} d^2\underline{x}' \tag{2.20}$$

Here $\underline{x}$ is the position at which the magnetic field is measured, $\underline{x}'$ is the position of the magnetic dipole, $\underline{\nabla}'$ is the Del operator in the $\underline{x}'$ coordinate system, and the integrals represent the summation of the contributions of all the individual magnetic dipoles (from inside the volume $\mathbb{V}$ and on the surface $\mathbb{S}$) to the dipolar field seen at position $\underline{x}$.

From Equation 2.20, it is evident that the contributions to the dipolar field from within the volume of the material is due to any nonuniformity of the magnetization. In a uniformly magnetized material, the only contribution to the dipolar field is the magnetization at the material's surfaces. In the special case of a uniformly magnetized ellipsoid, there is a very simple expression for the dipolar field:

$$\underline{H}_{dipole}(\underline{x}) = -(N_x\hat{x} + N_y\hat{y} + N_z\hat{z}) \cdot \underline{M} \tag{2.21}$$

$$N_x + N_y + N_z = 1 \tag{2.22}$$

where N_x, N_y, and N_z are the demagnetization constants for the specific material shape for the three cartesian axes. The name demagnetization constant is due to the fact that the dipolar field generated is always opposite the magnetization, which is also why these fields are often called demagnetization fields. Because different directions have different constants that depend on the shape, this interaction has also been called shape anisotropy. Figure 2.6 gives

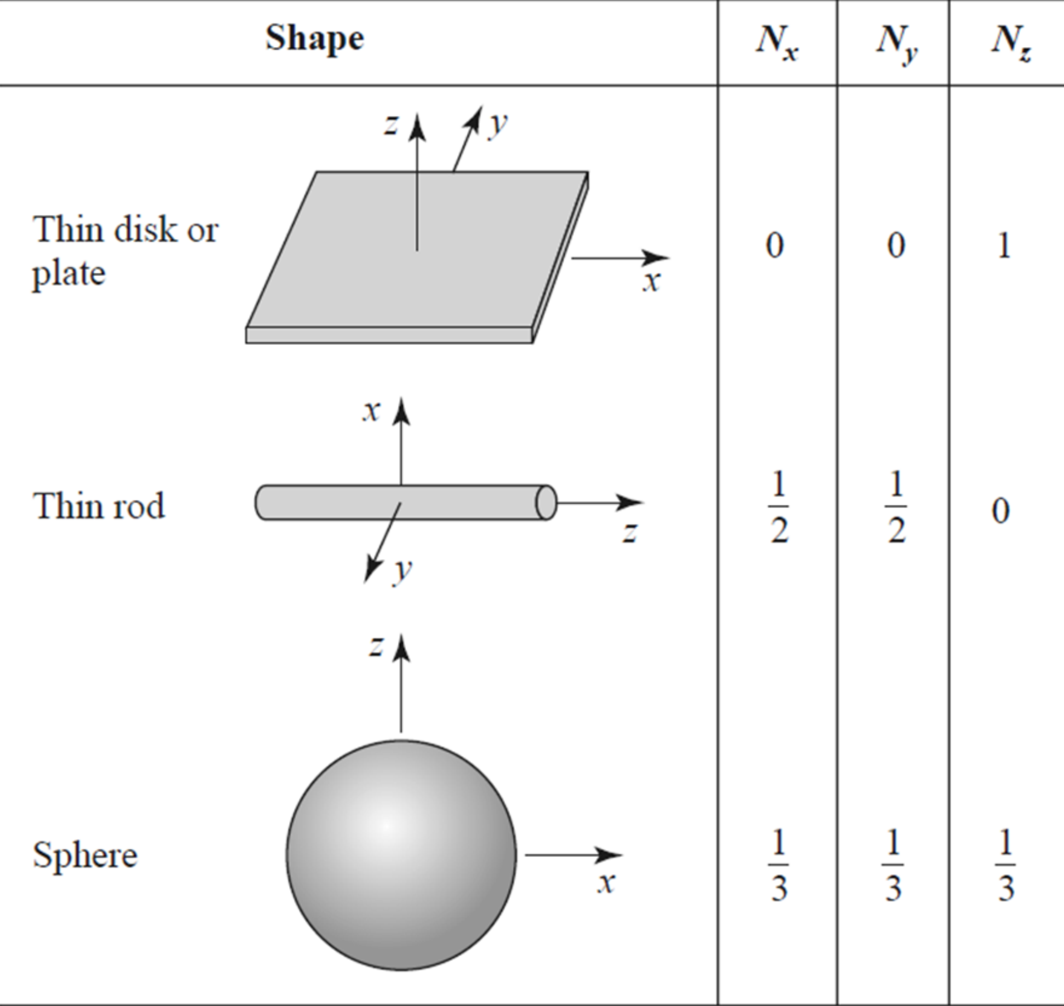

Demagnetization Factors for Some Simple Shapes

Shape	N_x	N_y	N_z
Thin disk or plate	0	0	1
Thin rod	$\frac{1}{2}$	$\frac{1}{2}$	0
Sphere	$\frac{1}{3}$	$\frac{1}{3}$	$\frac{1}{3}$

Figure 2.6: Demagnetizing constants for a thin plate, thin rod, and sphere. The plate is assumed to be infinitely thin and the rod is assumed to be infinitely long. Figure from [52].

demagnetization constants for common ellipsoidal shapes used in practice. Approximate demagnetization constants can also be calculated for nearly ellipsoidal geometries [199].

2.3.2 Exchange Interactions

Electrons, like all fermions, must follow the Pauli Exclusion Principle [200]. This physical law states that no two fermions may occupy the same quantum state and is a purely quantum mechanical interaction with no macro-scale analog. As a result, neighboring electrons exert a

“force” on each other so that they are oriented such that their quantum states do not overlap. This is the exchange interaction and is responsible for which of the three classes of magnetic materials shown in Figure 2.3 a material will belong to.

For the ferromagnetic materials focused on in this work, the energy for the exchange interaction is minimized when neighboring dipole moments are aligned [192]. The exact expression for the exchange energy and effective field depends on the structure of the material. In an amorphous ferromagnet, the effective field felt by the local magnetization depends on the relative orientation of its neighbors and is given by

$$\underline{H}_{exchange}(\underline{x}) = \frac{D}{\gamma \mu_0 M_s} \nabla^2 \underline{M}(\underline{x}) = \frac{D}{\gamma \mu_0} \nabla^2 \underline{\widehat{M}}(\underline{x}) \tag{2.23}$$

where D is the spin stiffness, also known as the exchange constant [70], [71], [201]. As this is an effective field, it does not factor into electromagnetic field calculations.

2.3.3 Magneto-Elastic Interactions

Exchange interactions discussed in the last section, as well as magneto-crystalline interactions in anisotropic materials, depend on the relative spacings between the spins in the material. If the spacings are perturbed, by straining the crystal lattice for example, then the equilibrium magnetization must change as the internal interactions have also been perturbed. This is the basis of the magneto-elastic interaction, where strains applied to a magnetic material will cause the magnetization to reorient. In an amorphous magnetostrictive material, the magneto-elastic energy density is given by

$$U_{ME} = \frac{B_{ME}}{M_s^2} \sum_{p=x,y,z} \sum_{q=x,y,z} M_p M_q S_{pq} \tag{2.24}$$

where B_{ME} is the magneto-elastic energy constant, and S is the local mechanical strain [71]. Using Equation 2.15, the effective field of an applied strain can then be calculated.

$$\underline{H}_{ME} = -\frac{B_{ME}}{\mu_0 M_s^2}\left[\left(M_x S_{xx} + 2M_y S_{xy} + 2M_z S_{xz}\right)\hat{x} \right.$$
$$+ \left(2M_x S_{xy} + M_y S_{yy} + 2M_z S_{yz}\right)\hat{y} \tag{2.25}$$
$$\left. + \left(2M_x S_{xz} + 2M_y S_{yz} + M_z S_{zz}\right)\hat{z} \right]$$

Just as a magnetic dipole has a magnetic field associated with it, a magnetic dipole in a magnetostrictive material has a stress and strain associated with it. When a magnetic field is applied, the magnetization will rotate and deform the material. To calculate the magnetostrictive stress from this process, a similar approach to Equation 2.15 can be taken.

$$T_{pq} = -\frac{\partial U_{ME}}{\partial S_{pq}} = -B_{ME}\frac{M_p M_q}{M_s^2} \qquad for \qquad p, q = x, y, z \tag{2.26}$$

An important fact to note is that the magnetostrictive stress (and the associated strain) will saturate with magnetic field. As the magnetic field increases, the magnetization will align to it and the strain in that direction will increase. Once the material is saturated to its saturation magnetization, its magnetostrictive strain will also saturate at a value called the saturation magnetostriction, λ_s (Figure 2.7).

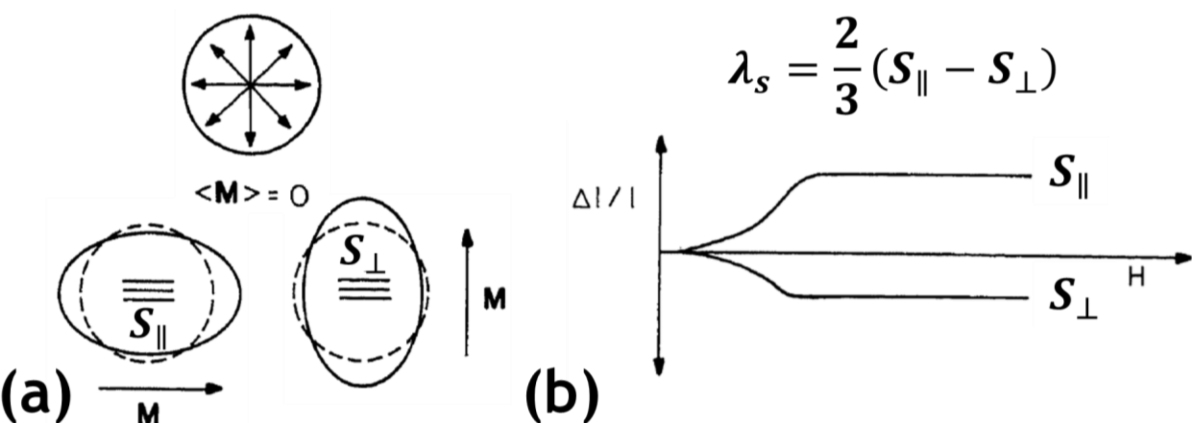

Figure 2.7: (a) Deformation of a sphere via magnetostrictive strains. (b) Saturation of strain in a magnetostrictive material. Adapted from [192].

Drawing another analog to dipole interactions, the stresses created by the magneto-elastic interactions are real. Therefore, a complete analysis of a magneto-elastic problem requires a simultaneous solution of Equation 2.18 and the elastodynamic equations of motion.

2.3.4 Dissipative Interactions

As a magnetic dipole rotates, it undergoes a variety of interactions that will cause it to dissipate energy [71], [192], [202]. These interactions redistribute the energy of the rotating dipole until it eventually stops moving and settles into an equilibrium position. As can be seen in Figure 2.8, there are several ways the energy can be redistributed by these interactions. Transient electric fields created by the rotating dipoles can stimulate dielectric losses or transfer energy to mobile charges, generating eddy currents. Defects in the material can cause energy to be scattered from the driven magnetization mode to other modes not useful for device operation. No matter the exact interaction (or series of interactions), the end result is that the energy eventually flows to the lattice and generates heat.

As can be surmised from Figure 2.8, exact modelling of losses is a very complicated problem. However, losses can be added to Equation 2.18 by use of phenomenological effective field that resists the rotation of the magnetization.

$$\underline{H}_{loss} = -\frac{\alpha}{M_s}\underline{\dot{M}} \tag{2.27}$$

Here α is known as the Gilbert damping constant and is found by fitting measurement data. The proportionality to $\underline{\dot{M}}$ ensures that the field is only present when the magnetization is moving, and the negative sign ensures that the torque produced always opposes the change in the magnetization.

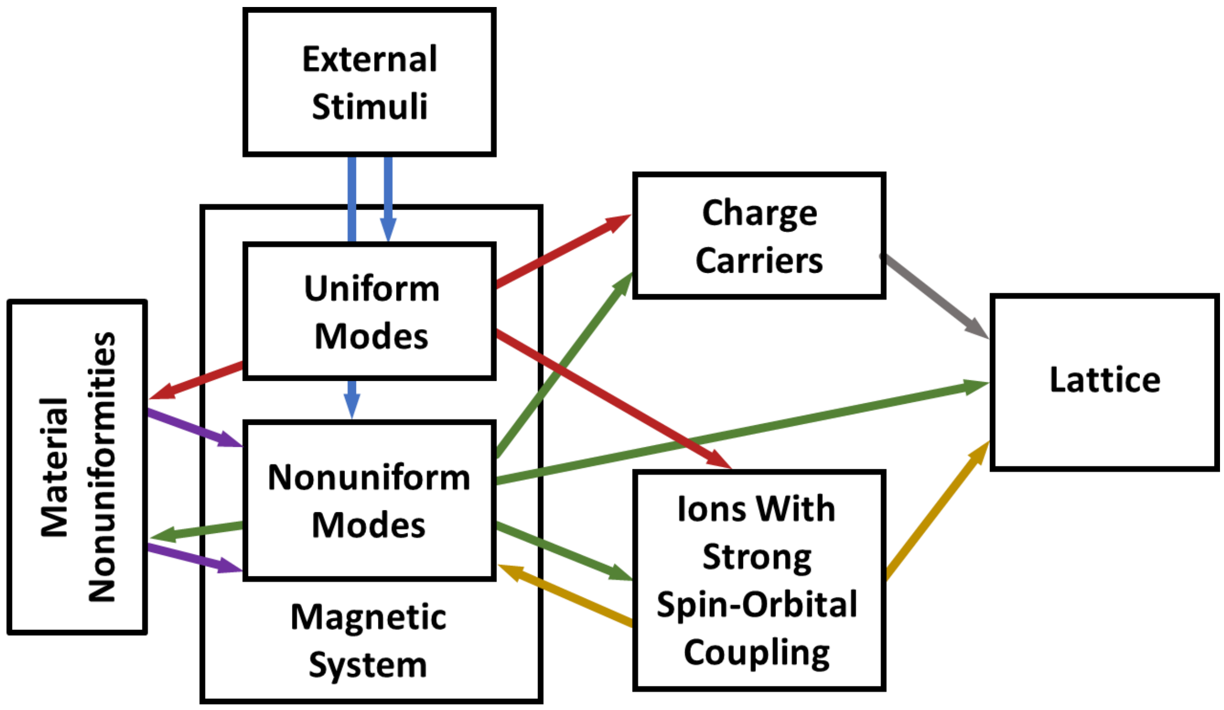

Figure 2.8: Schematic of various mechanisms of energy redistribution inside a magnetic material. Adapted from [71].

As discussed in Section 2.1, there are two types of magnetization changes, large changes caused by domain wall motion (Figure 2.2b) and small changes from dipole rotation (Figure 2.2c). The sources of damping for these two cases are the same but manifest differently because of the differences in dynamics. Small changes happen continuously and are thus continuously damped. Large changes in magnetization happen predominantly via localized discontinuous and rapid motion of the domain walls, called Barkhausen jumps [202]. Because of this, it is often useful to treat the damping of both processes separately when modelling.

2.4 Solutions to the Equation of Motion

2.4.1 Simplifications for Independent Spins

Exact analytical solutions to Equation 2.18 are difficult to derive, but it is instructive to solve the equation in a few approximate cases. Consider an undamped system of independent

spins uniformly magnetized by a DC bias field $\underline{H} = H_0\hat{x} = H_{ext}\hat{x}$, but with no AC magnetic field. Because the spins are independent, there are no internal interactions between them. Equation 2.18 can then be written as follows:

$$\underline{\ddot{m}} + [\omega_0^2(\underline{m} - (\underline{m} \cdot \underline{\hat{x}})\underline{\hat{x}})] = 0$$

$$\begin{bmatrix} \ddot{m}_x + 0 \\ \ddot{m}_y + \omega_0^2 m_y \\ \ddot{m}_z + \omega_0^2 m_z \end{bmatrix} = \begin{bmatrix} 0 \\ 0 \\ 0 \end{bmatrix} \tag{2.28}$$

Equation 2.28 is a system of second order differential equations similar to that of a harmonic oscillator with a natural frequency of $f = \frac{\omega}{2\pi} = \frac{\omega_0}{2\pi} = \frac{\gamma\mu_0 H_{ext}}{2\pi}$. This frequency is called the Larmor precession frequency or, in ferromagnetic materials, the ferromagnetic resonance (FMR) frequency. The assumption that the material is uniformly magnetized means that the material must be saturated, meaning that the minimum bias field applicable for this model is $H = H_{sat}$ and the minimum FMR frequency is $f_{min} = \frac{\gamma\mu_0 H_{sat}}{2\pi}$. FMR in unsaturated materials will be discussed in Chapter 4.

Since the DC magnetic field, and thus the DC magnetization, is along the x-axis, the magnetization does not move at all in the x direction. The magnetization only moves in the yz-plane, precessing about the bias field with a frequency of ω_0, as shown in Figure 2.9. In a real system, damping is present and the precessional motion will eventually lose energy until it aligns with the bias field in the $+x$ direction.

If a small AC magnetic field is applied to the spins (perpendicular to the DC field, as discussed in Section 2.2.1), the amplitude of the magnetization change is maximized when the frequency of the AC field is ω_0. This magnetization change manifests itself as a peak in the measured susceptibility, as shown in Figure 2.10. As the amplitude of the magnetization is maximized here, the loss measured is also maximized. The increase in damping is exploited to

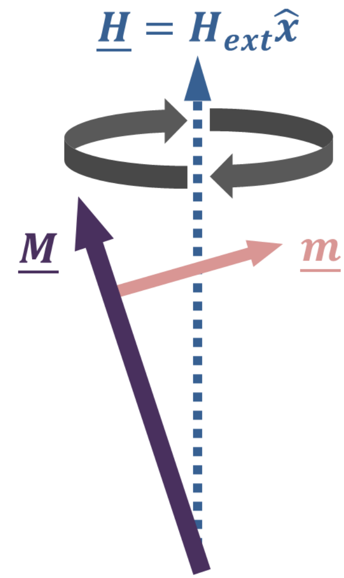

Figure 2.9: Precessional motion of magnetization about the DC bias field.

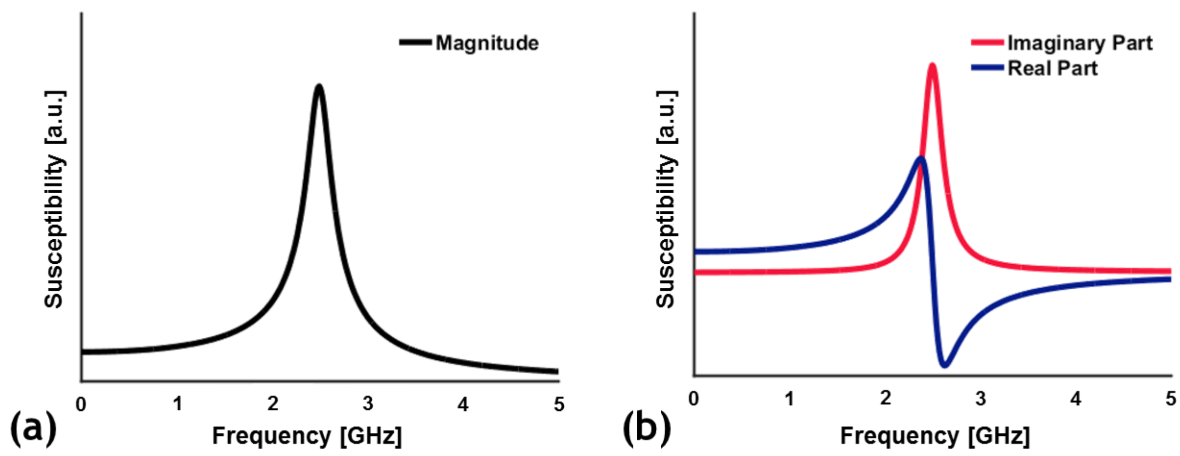

Figure 2.10: (a) Magnetic susceptibility magnitude peaking at FMR. (b) Real and imaginary parts of susceptibility. The imaginary part peaks at FMR, indicating that damping is maximized at this point.

characterize FMR in magnetic materials, by measuring the bandwidth and frequency of the damping peak [173], [174].

2.4.2 Simplifications for a Single Domain Thin Film

For micro-magnetic problems, a more realistic scenario is that of a magnetic thin film uniformly magnetized in-plane. In this case, in addition to the externally applied DC magnetic

field, $\underline{H}_{ext} = H_{ext}\hat{x}$, there are now contributions from AC dipolar fields. Referring to Figure 2.6, the sum of the external and dipolar fields can easily be calculated.

$$\begin{aligned} \underline{H} &= \underline{H}_{ext} + \underline{H}_{dipole} = H_{ext}\hat{x} - N_z\hat{z}\cdot\underline{M} \\ &= H_{ext}\hat{x} - N_z\hat{z}\cdot\left(M_s\hat{x} + \underline{m}\right) = H_{ext}\hat{x} - m_z\hat{z} \end{aligned} \tag{2.29}$$

Substituting this into Equation 2.18, yields the equation of motion for the magnetic thin film (in the absence of damping and an AC stimulus).

$$\ddot{\underline{m}} + \left[\omega_0^2\left(\underline{m} - \left(\underline{m}\cdot\hat{x}\right)\hat{x}\right)\right] - \left[\omega_0\omega_M\left(\underline{h}_{MM} - \left(\underline{h}_{MM}\cdot\hat{x}\right)\hat{x}\right)\right] + \left[\omega_M\left(\hat{x}\times\dot{\underline{h}}_{MM}\right)\right] = 0$$

$$\ddot{\underline{m}} + \left[\omega_0^2\left(\underline{m} - \left(\underline{m}\cdot\hat{x}\right)\hat{x}\right)\right] - \left[\omega_0\omega_M(-m_z\hat{z} + (m_z\hat{z}\cdot\hat{x})\hat{x})\right] - \left[\omega_M\left(\hat{x}\times(\dot{m}_z\hat{z})\right)\right] = 0$$

$$\ddot{\underline{m}} + \left[\omega_0^2\left(\underline{m} - \left(\underline{m}\cdot\hat{x}\right)\hat{x}\right)\right] + \left[\omega_0\omega_M m_z\hat{z}\right] + \left[\omega_M\dot{m}_z\hat{y}\right] = 0$$

$$\begin{bmatrix} \ddot{m}_x + 0 \\ \ddot{m}_y + \omega_0^2 m_y + \omega_M\dot{m}_z \\ \ddot{m}_z + \omega_0(\omega_0 + \omega_M)m_z \end{bmatrix} = \begin{bmatrix} 0 \\ 0 \\ 0 \end{bmatrix} \tag{2.30}$$

Equation 2.30 is similar to a system of harmonic oscillators, except now the motion of m_y has a dependence on $\dot{m}_z$. Because the DC bias is along the x-axis, there is no change in m_x. The m_y and m_z components of the magnetization change with time, but the addition of shape anisotropy along the z-axis gives rise to different equations of motion for m_y and m_z.

We see in Equation 2.30 that the natural frequency of m_z has been modified in the presence of dipolar fields.

$$f = \frac{\omega}{2\pi} = \frac{1}{2\pi}\sqrt{\omega_0(\omega_0 + \omega_M)} = \frac{\mu_0\gamma}{2\pi}\sqrt{H_{ext}(H_{ext} + M_s)} \tag{2.31}$$

Equation 2.31 is known as Kittel's equation [52]. It can be seen, by comparing the FMR frequency found here versus that in the last section, that a uniformly in-plane magnetized thin film has a higher FMR frequency than a system of independent spins for the same bias field.

This is because the demagnetization field caused by the m_z component is in the opposite direction of m_z, resisting the change in m_z and stiffening the magnetic system, which raises the resonance frequency. This is an advantage for thin film systems, as lower bias fields are easier to achieve in practice.

2.4.3 Simplifications for Domain Wall Dynamics

Applying Equation 2.18 to domain wall motion in a multi-domain state is complicated by many issues, such as nonuniformity of the internal fields, Barkhausen jumps, and pinning from defects. However, it has been shown that the average domain wall motion in a material can be modelled with a simple second order differential equation [71], [192], [202], [203].

$$m_w \ddot{\xi} + \beta_w \dot{\xi} + \alpha_w \xi = M_s \cdot h_{ext} \tag{2.32}$$

Here m_w is the domain wall effective mass (derived from the kinetic energy of a moving domain wall), β_w is the domain wall damping, and α_w is the domain wall stiffness, which all depend on the current internal domain structure of the material. The variable ξ is the average domain wall displacement. Solutions for this equation can then be used to derive a dynamic susceptibility for a domain wall. Assuming harmonic forcing ($h_{ext} = |h_{ext}|e^{j\omega t}$), the dynamic susceptibility is:

$$\chi = \frac{\chi_{DC}}{1 - \frac{\omega^2}{\omega_{0w}^2} + j\frac{1}{Q_w}\frac{\omega}{\omega_{0w}}} \tag{2.33}$$

$$\omega_{0w} = \sqrt{\frac{\alpha_w}{m_w}} \tag{2.34}$$

$$Q_w = \frac{\sqrt{\alpha_w m_w}}{\beta_w} \tag{2.35}$$

Here χ_{DC} is the DC susceptibility, ω_{0w} is the domain wall resonance frequency, and Q_w is the quality factor.

Figure 2.11 shows measured multi-domain susceptibilities at different DC magnetic fields [204]. The domain wall resonance frequency (also known as the relaxation frequency) is a cutoff frequency for the domain response. At frequencies much lower than ω_{0w} the domain walls move quickly, and the response is flat. At frequencies much higher than ω_{0w}, the domain walls cannot move fast enough to respond to the stimulus, and the susceptibility drops to zero. A key feature of the measurements shown in Figure 2.11 is that changing the bias magnetic field changes the frequency response of the instantaneous permeability, because of the change in the internal domain structure. Higher bias fields lead to lower DC susceptibilities but increase the range over which the instantaneous susceptibility is flat. This is a manifestation of Snoek's law, which dictates that the higher the DC permeability of the material, the lower the cut off frequency will be [203]. This is an important tradeoff to consider when choosing the optimal bias point for the material, as a bias point with a higher permeability comes at the cost of a lower bandwidth. Note that the loss also changes as a function of the applied magnetic field, as shown in Figure 2.11b.

2.4.4 Regimes of Dynamic Magnetization

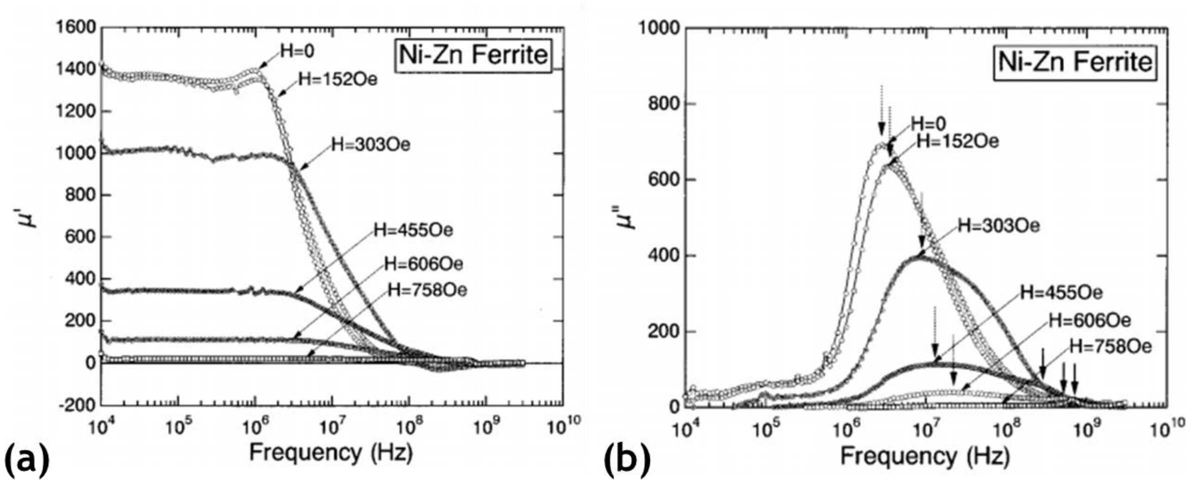

Figure 2.11: Measured (a) real and (b) imaginary parts of permeability for Ni-Zn Ferrite for several bias magnetic fields. Note that the frequency axis is in log-scale. Figures from [204].

As can be gleaned from the last three examples, the dynamics of the magnetization is a strong function of both the frequency and the magnetic structure [203]. In general, the broadband frequency response of a magnetic material follows the trend shown in Figure 2.12. This curve can be conceptually divided into three parts. At low frequencies, the susceptibility does not vary and matches the DC value. This is the quasi-static zone and is predominantly driven by domain wall motion. As discussed in the last section, domain walls have a cut off frequency, typically at a few 100's of MHz, after which they cannot move quickly enough to keep pace with the applied field. This is cut-off zone and past this zone the domain wall response is practically zero. At higher frequencies, typically near 1 GHz or higher, the predominant contribution to the susceptibility is spin precession. The response is low until the frequency approaches the FMR frequency, at which point the response peaks. After FMR, the response again drops to close to zero. However, above the FMR frequency it is now possible to

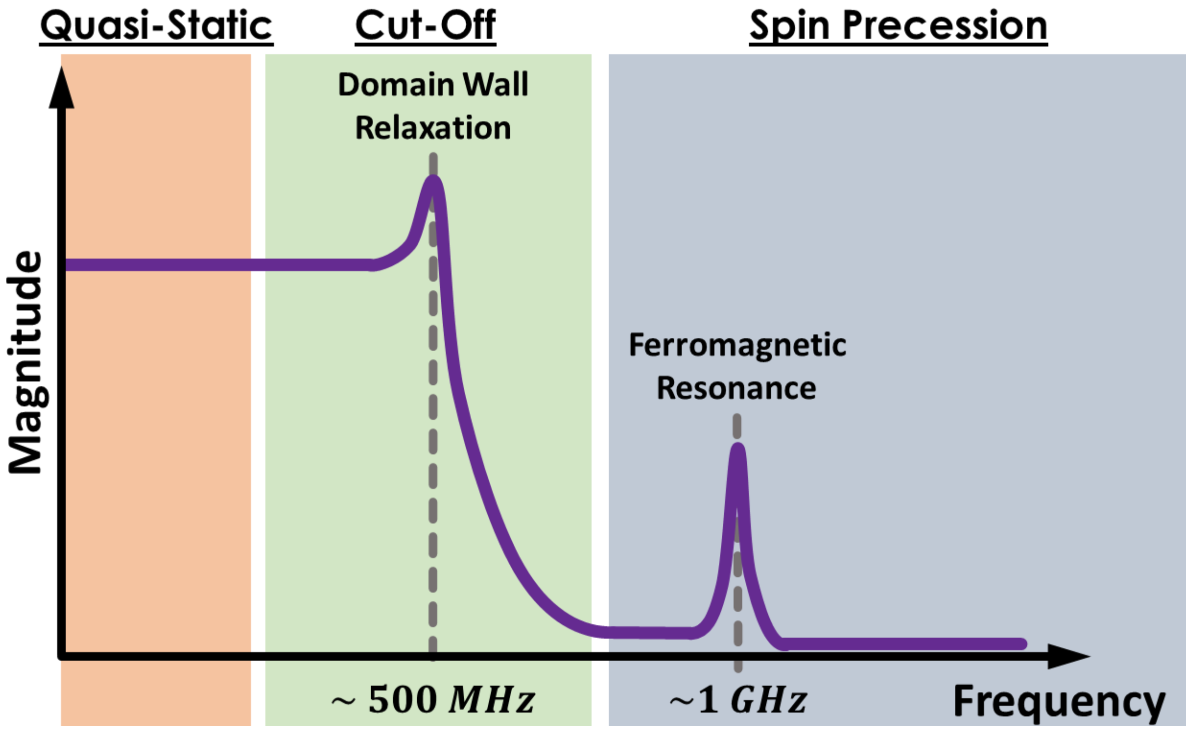

Figure 2.12: Trend for the instantaneous susceptibility of an arbitrary magnetic material. This is broken up into three zones depending on the frequency: Quasit-Static, Cut-Off, and Spin Precession.

drive waves of magnetization called spin waves [54], [55]. As domain wall motion does not contribute at these frequencies (their presence may even cause more dissipation), the response in this zone is maximized when the material is completely saturated.

Summarizing these points, dynamic magnetization can broadly be categorized into six regimes categorized by which of the three zones in Figure 2.12 (quasi-static, cut-off, or spin precession), and which of the two possible internal states (single domain or multi-domain) the magnetic material is operating in. The importance of this is that the characterized dynamics in one regime does not necessarily carry over to the others. Meaning that, if characterization and analysis is to be done on a magnetic system, it is paramount to do this in the same regime that the system is intended to operate in. Values derived or measured in one regime will not necessarily accurately predict a system’s performance in another.

Chapter 3 Nonlinear MF Actuation

3.1 Wirelessly Actuated Multiferroic Devices

3.1.1 Linear Multiferroic Devices

As discussed in Section 1.4.1, a large amount of research in dynamic multiferroics is driven by interest in wireless devices. Magnetic fields are heavily used in wireless near-field systems because they penetrate much deeper into lossy dielectrics, such as salt water and the human body [205]. Strain-coupled multiferroic devices are a route towards the efficient miniaturization of these systems due to their ability to sense and generate magnetic fields via capacitive transducers, combined with the fact that mechanical resonators can achieve much higher quality factors than what is possible with electronics [170], [206]. Large changes in magnetization are needed to sense and generate magnetic fields with high efficiency, meaning that the wireless devices that have been successfully demonstrated have all operated in a multi-domain state, in the quasi-static frequency regime [10], [12], [164]–[166], [207]–[210]. These devices have focused on the sensing of magnetic fields, as measurement of magnetic fields radiated by small-scale multiferroic devices remains a challenge, due to parasitic radiation from the characterization equipment [171], [172]. However, a macro-scale proof-of-concept of multiferroic radiation has recently been demonstrated by Schneider et al. [12].

Wireless multiferroic transduction has found applications in transformers/gyrators [207], [208], energy harvesting [164]–[166], antennas [10]–[12], and sensors [209], [210].

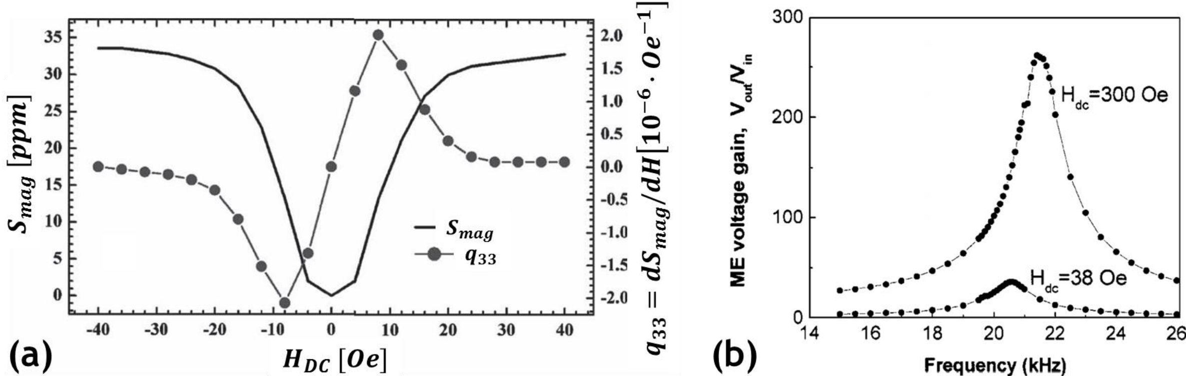

Figure 3.1: (a) Variation of magnetostrictive strain,S_{mag}*, and piezomagnetic constant,* q_{33}*, as a function of bias magnetic field. Adapted from* [209]. *(b) Frequency dependence of multiferroic transduction at two different bias magnetic fields in a multiferroic transformer. The coupling peaks at the mechanical resonance frequency. Figure from* [207].

Maximizing the piezomagnetic coupling in these devices requires the maximization of the domain wall mobility. As discussed in Section 2.4.3, the mobility of the domain walls depends on the domain structure, making the piezomagnetic coupling tunable via an applied magnetic field (Figure 3.1a). Further enhancement of the magnetization change can be achieved by using mechanical resonance, where the amount of elastic strain energy is maximized in the structure (Figure 3.1b).

3.1.2 Nonlinear Multiferroic Devices

While wireless multiferroic resonators have the advantage of high sensitivity due to the large strains they can generate, they have a major disadvantage in that they are very narrow bandwidth. However, the inherent nonlinearity in magnetostrictive and ferroelectric materials can be leveraged so that broadband devices can be made while retaining the narrowband amplification of mechanical resonance [211]–[213]. In these devices, instead of a DC bias, a large amplitude modulation signal (either a magnetic or electric field) is applied to the device. When an AC magnetic field is measured by the device, the nonlinearity causes the frequency to mix with the modulation frequency and generate an upconverted signal at the mechanical resonance frequency. If the modulation frequency is swept, it can be made that any measured

magnetic field can excite the mechanical resonance, yielding a high amplitude broadband response. The added benefit of this approach is that $1/f$-noise and noise from ambient vibrations that are typical problems in linear sensing of low frequency signals [206].

Upconversion of the measured magnetic field frequency does not necessarily require the use of a dynamic modulation field. At low bias fields linear piezomagnetic coupling is weak and a quadratic term dominates, meaning that any measured magnetic fields will yield a strain at double this frequency [214]–[216]. This kind of passive frequency doubling is incredibly useful in the measurement of magnetic fields in noisy environments. For instance, it can be used to implement a harmonic RFID system [217]. When an RFID reader interrogates a passive RFID tag, it must find a way to differentiate the tag signal from back scattering of the original interrogation signal (Figure 3.2a). In a harmonic RFID system, the RFID tag passively doubles the frequency of the interrogation signal and reradiates a signal at this new frequency. With some basic filtering, the RFID reader can now easily sort out the tag signal from backscatter.

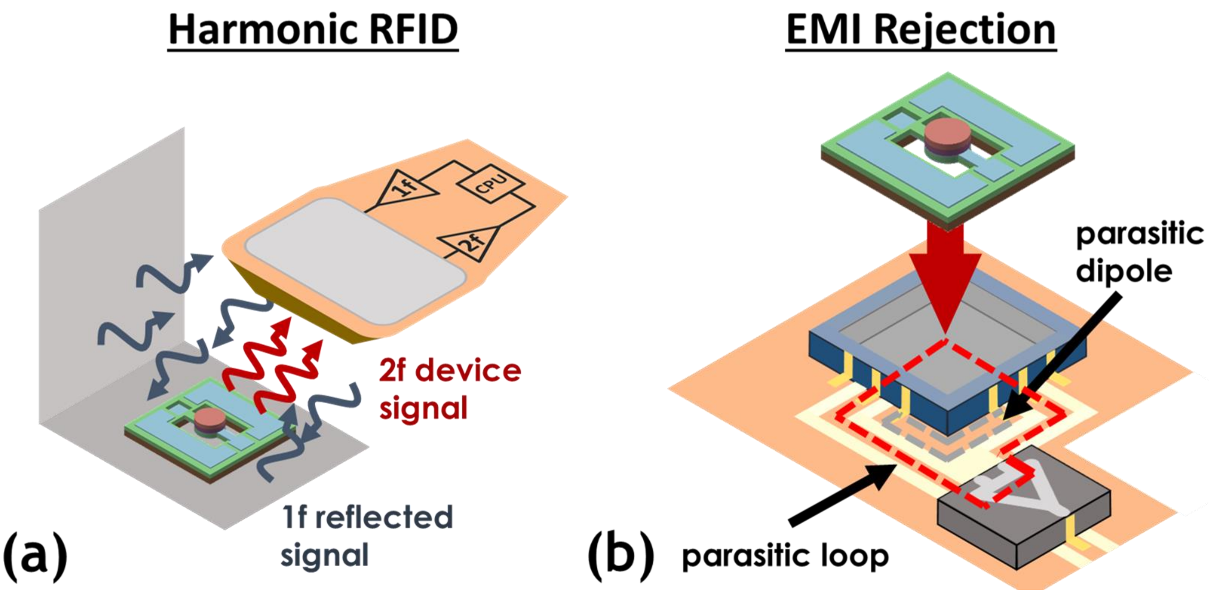

Figure 3.2: (a) Schematic of harmonic RFID system. The reader emits a $1f$ signal, and the passive RFID tag reradiates a $2f$ signal to distinguish itself from backscatter. (b) Package of a test device with parasitic antennas identified. These antennas receive electromagnetic signals and make it difficult to characterize the true device response.

Another application is in the characterization of magnetic devices and fields (Figure 3.2b). The layout of the device packaging can result in parasitic antennas that generate currents when exposed to dynamic magnetic fields, making it difficult to decouple the electromagnetic interference of the parasitics from what is measured by the device. However, if the signal generated by the device doubles the frequency of the magnetic field, simple filtering is all that is required to separate the device signal from the parasitics.

3.2 Nonlinearity from Perpendicular Poling

The devices discussed up until now all utilize parallel magnetic poling, where the bias magnetic field is applied parallel to the AC magnetic field. While this is traditionally what is done to optimize the response of the linear piezomagnetic coupling, there are several downsides when nonlinear piezomagnetic coupling comes into play. As discussed above, passive frequency conversion can only be achieved with low bias fields, meaning that if the device is exposed to even a moderately strong stray magnetic field, the operating point can shift appreciably. This limits tunability of the nonlinear coupling as higher bias fields push the magnetic material into the linear piezomagnetic regime, meaning active nonlinearity through bias modulation must be used. Even higher bias fields eliminate the piezomagnetic coupling all together (Figure 3.1a).

If the bias field is applied perpendicular to the direction of the AC magnetic field, the symmetry of the system ensures nonlinear operation. This can be seen with a simple model for the magnetostrictive stress generated by a magnetic field. Using Equation 2.26, consider the extensional strain along the x-axis.

$$T_{xx} = -\frac{\partial U_{ME}}{\partial S_{xx}} = -B_{ME}\frac{M_x M_x}{M_s^2} \tag{3.1}$$

In the simple approximation where there is no back-action from the magneto-elasticity on the change in the magnetization, if the sample is biased along the y-direction and an AC small magnetic field is applied in the x-direction, the extensional strain is now given below.

$$T_{xx} = -B_{ME}\frac{(M_{0x} + m_x)^2}{M_s^2} = -\frac{B_{ME}}{M_s^2}(M_{0x}^2 + 2M_{0x}m_x + m_x^2) \tag{3.2}$$

However, this is only the localized stress in the material. If the material is assumed to be amorphous, this equation can be averaged across the volume to find the effective stress felt by the material.

$$\langle T_{xx}\rangle = -\frac{B_{ME}}{M_s^2}(\langle M_{0x}^2\rangle + 2\langle M_{0x}m_x\rangle + \langle m_x^2\rangle) \tag{3.3}$$

The first term is a DC stress within the material and is irrelevant to the dynamics. The second term is the linear piezomagnetic coupling term. Since the material is amorphous, anisotropy can only be along the y-axis because of the bias magnetic field, meaning that there must be equal amounts of M_{0x} pointing in the positive and negative directions due to the symmetry of the x-direction. Because of this, the second term will average to zero and now all that is left is the third term, which is quadratic in the change in magnetization.

$$\langle T_{xx}\rangle = -\frac{B_{ME}}{M_s^2}\langle m_x^2\rangle \tag{3.4}$$

The underlying mechanism for this nonlinearity can be understood pictorially through Figure 3.3. When zero field is applied, the magnetization is predominantly aligned towards the y-direction and the magnetostrictive strain is along the y-axis. When a positive field is applied along the x-direction, the magnetization on average rotates towards it and projects the magnetostrictive strain along this direction, leading to long axis compression. When the field is removed, the material returns to its initial state. When the field is reversed to point in the

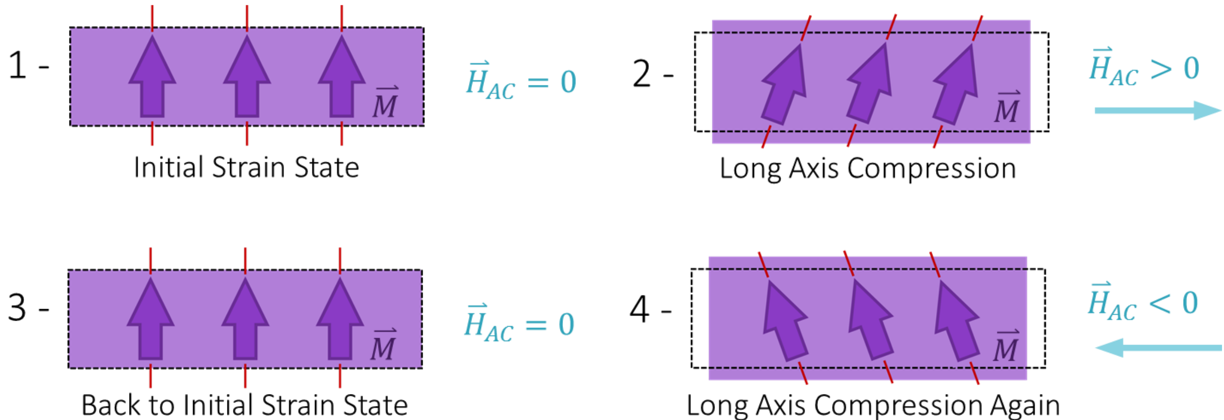

Figure 3.3: Pictorial representation of magneto-elastic frequency doubling through perpendicular poling. The purple arrows are the magnetic dipoles in the material and the red lines represent the magnetostrictive strain associated with the magnetic dipoles. The material is assumed to have negative magnetostriction, so the red axis is associated with compressive strain.

negative x-direction, the magnetization rotates towards it and projects the magnetostrictive strain along the x-axis, again leading to long axis compression. At zero field, the material once again returns to its initial state. For one cycle of magnetic field (zero, positive, zero, negative) there are two cycles of strain (undeformed, compression, undeformed, compression), which is another way of saying that the frequency of the magnetic field is doubled via the strain output.

As can be seen pictorially in Figure 3.3 and by the derivation of Equation 3.4, as long as the DC symmetry in the x-direction is maintained, the magneto-elastic coupling will remain quadratic. This showcases the advantage of perpendicular poling; passive nonlinear coupling can be leveraged but a bias magnetic field can still be used to add robustness to the system.

3.3 Experimental Approach

3.3.1 Device Design and Fabrication

To demonstrate frequency doubling behavior, resonant multiferroic MEMS cantilevers were designed and fabricated (Figure 3.4). These cantilevers are bimorphs with aluminum

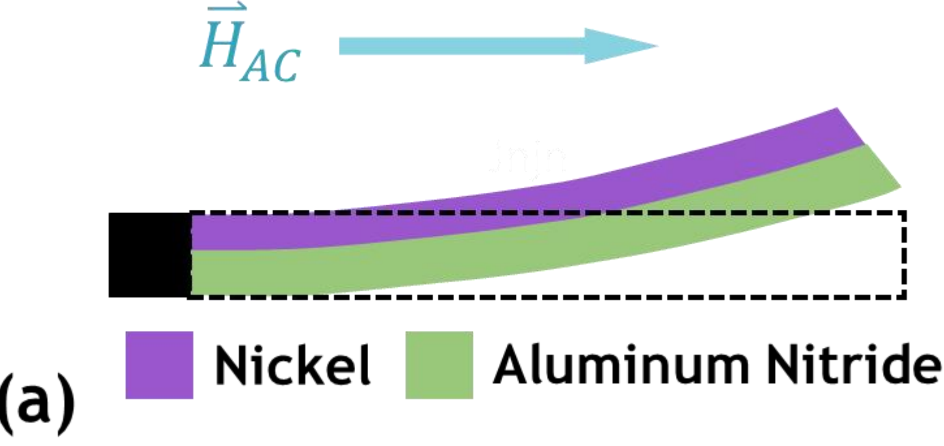

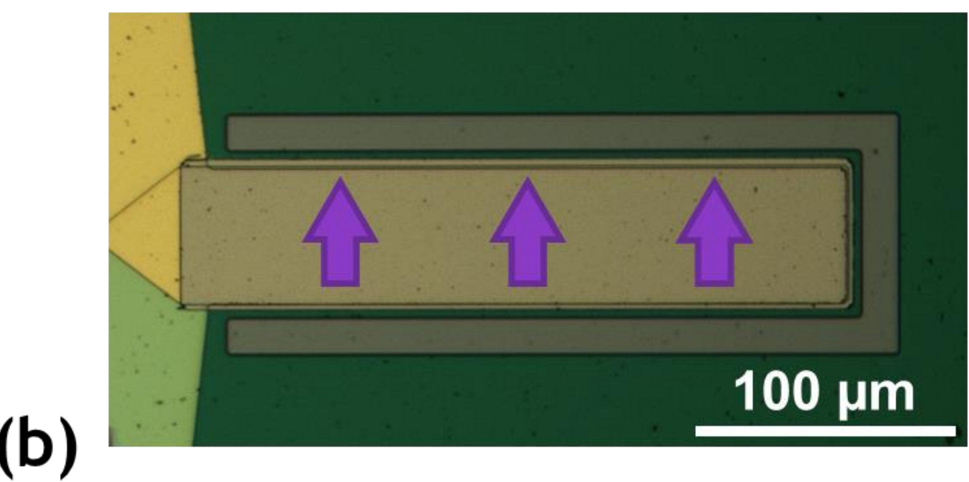

Figure 3.4: (a) Cross section of a multiferroic bimorph cantilever. Depicted is the resonant mode excited by an AC magnetic field along the long axis of the cantilever. The dotted lines represent the undeformed state. (b) Multiferroic cantilever before silicon etching to release the MEMS structure. The purple arrows indicate the intended direction of the DC magnetization during the experiments.

nitride serving as the piezoelectric material and nickel as the magnetostrictive material. When the nickel is poled along the short axis of the cantilever, nonlinear transduction of the fundamental cantilever resonant mode is driven by an AC magnetic field along the long axis.

The fabrication process (Figure 3.5) begins with 4” (100) high resistivity silicon substrates. Platinum (170 nm) is deposited (with 10 nm of titanium as an adhesion layer) for the bottom electrode by evaporation using a CHA Solution Electron Beam evaporator and is patterned via a lift-off process. An aluminum nitride (400 nm) blanket film is then reactively

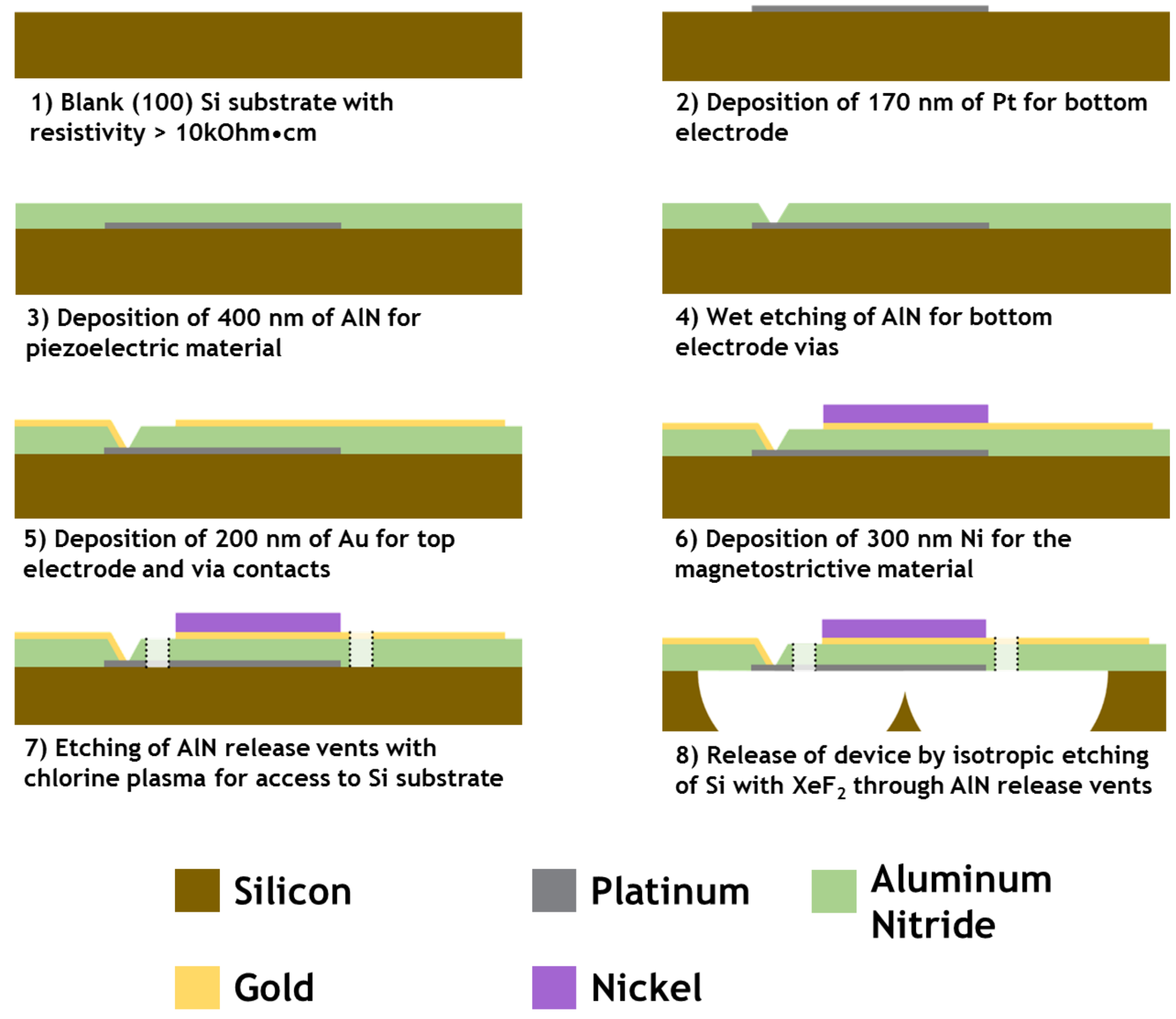

Figure 3.5: Cross sections of the fabrication process flow for the multiferroic MEMS cantilevers.

sputtered with a Tegal AMS Aluminum Nitride Sputtering System at the Claire & John Bertucci Nanotechnology Laboratory at Carnegie Mellon University. Vias for bottom electrode contact are then wet etched with AZ 300 MIF photoresist developer using a KMPR 1005 mask. Titanium (10 nm) / gold (200 nm) for the top electrodes and via contacts is deposited by evaporation with a CHA Mark 40 system and is patterned by lift-off. For the magnetostrictive layer, titanium (20 nm) / nickel (300 nm) is deposited by evaporation with a CHA Mark 40 system and is again patterned by lift-off. To define the edges of the resonator, the devices are plasma etched using a chlorine gas chemistry with a Unaxis SLR770 ICP system using a KMPR 1005 mask. The wafer

is then diced, and the devices are released at the die level by isotopically etching the silicon substrate using XeF_2 gas with a custom etching system.

3.3.2 Device Characterization

The magnetic hysteresis loop of the deposited nickel film is characterized using a superconducting quantum interference device (SQUID) and is shown in Figure 3.6a. The nickel is found to saturate in fields greater than approximately 2000 Oe. To electrically characterize the sample, the die is mounted on a printed circuit board (PCB) and electrical contact is made by wire-bonding (Figure 3.6b). The devices are placed in a Janis ST-500 cryostat with custom

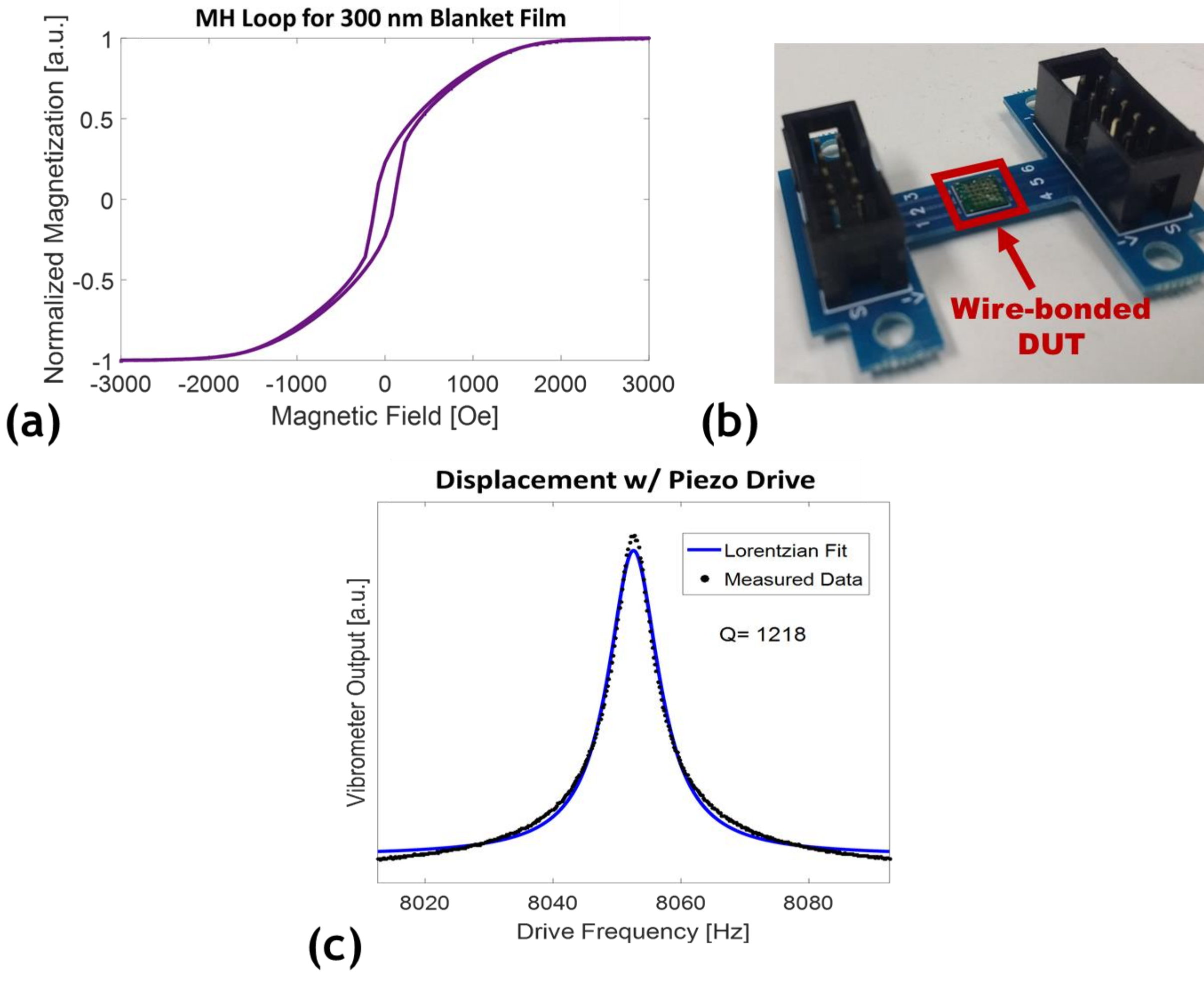

Figure 3.6: (a) Normalized measured hysteresis loop for the deposited nickel thin film. (b) PCB with a device to be tested in the vacuum chamber. (c) Measured frequency response of the MEMS multiferroic cantilever when driven with the piezoelectric layer.

electrical interfacing for the device PCB, and the cryostat is pumped down to below 10^{-4} mbar to minimize air damping. To determine the cantilever quality factor and resonance frequency, a frequency swept voltage is applied to the aluminum nitride layer and the displacement is measured using a HP4195A spectrum analyzer and a Polytec OFV-5000 laser Doppler vibrometer (LDV). The cantilever quality factor is found to be about 1200 and the resonance frequency is 8052.6 Hz (Figure 3.6c). As the vacuum chamber is not able to apply a bias magnetic field perpendicular to the device, the devices are poled along the short axis in a magnetic field greater than 2500 Oe before being placed in the vacuum chamber, and the devices are tested in the remanent magnetization state to achieve quadratic magnetostrictive behavior.

Figure 3.7 shows a schematic of the experimental set up to measure the frequency doubling. To magnetically actuate the devices, Helmholtz coils are placed into the vacuum chamber and are driven by an Agilent 33120A function generator. The field generated by these coils is parallel to the cantilever long axis. The cantilever displacement is again measured using

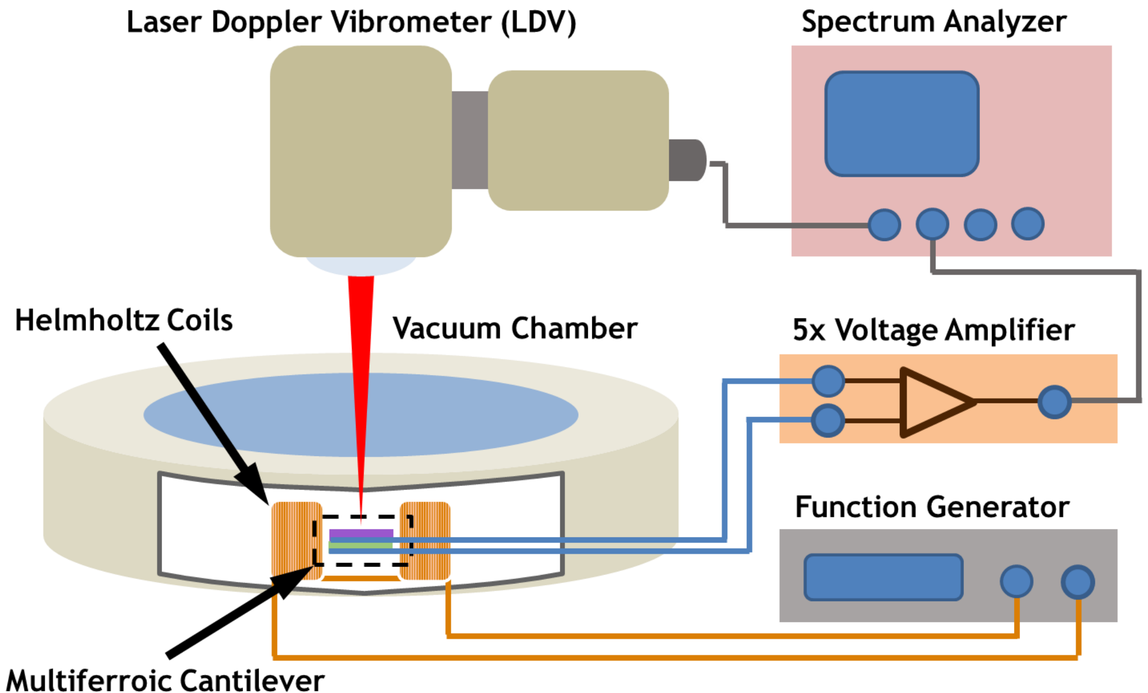

Figure 3.7: Schematic of the test set up used to characterize multiferroic MEMS cantilevers.

the LDV and spectrum analyzer. The output voltage generated by the multiferroic device is measured using a Stanford Research Systems SR560 low-noise voltage preamplifier and the spectrum analyzer. The coil drive frequency is swept from 4019.3 Hz to 4033.3 Hz and the sweep is done for four different function generator output amplitudes: 250 mV_{pp}, 500 mV_{pp}, 750 mV_{pp}, and 1000 mV_{pp}.

3.4 Experimental Results

The results of the experiment are summarized in Figure 3.8. The displacement of the cantilever as a function of frequency is plotted in Figure 3.8a for several AC voltages applied to the Helmholtz coils. The bottom axis is the drive frequency, which is the frequency of the magnetic field generated by the Helmholtz coils. The top axis is the sense frequency, which is the frequency at which the displacement is measured and is twice the drive frequency. As the drive frequency increases, the cantilever displacement also increases until it reaches a peak value at a drive frequency of 4026.3 Hz, which is half of the resonant frequency found for the device. Afterwards the displacement falls, as would be expected for a resonator. Figure 3.8b plots the peak cantilever displacement as a function of the voltage applied to the Helmholtz coils, which is linearly proportional to the magnetic field generated. Peak cantilever displacement is found to increase with the square of the coil driving voltage, as expected since the magnetostrictive strain depends quadratically on the applied AC magnetic field due to the perpendicular poling.

As mentioned in Section 3.1.2, passive upconversion can be a very helpful technique to alleviate issues with electromagnetic interference during characterization of small-scale wireless devices (Figure 3.2b). To demonstrate this, the output voltage was measured at both

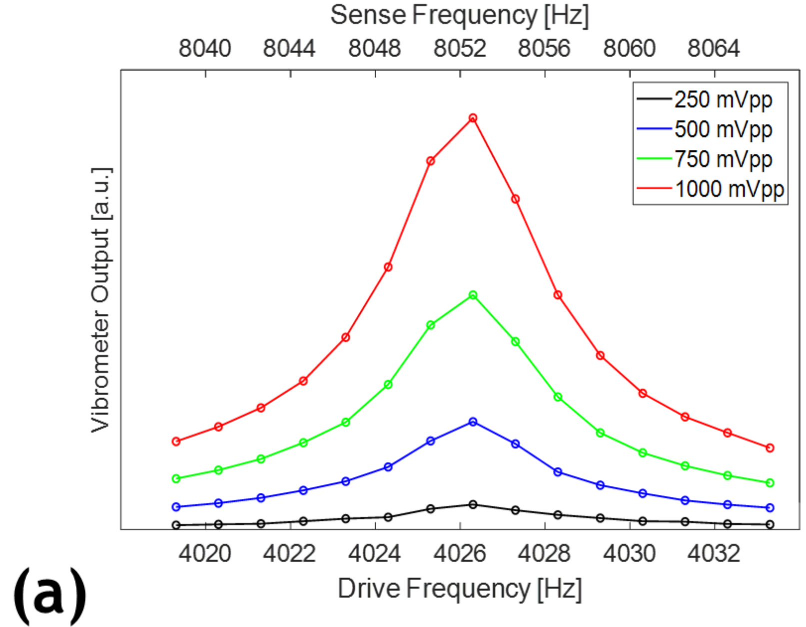

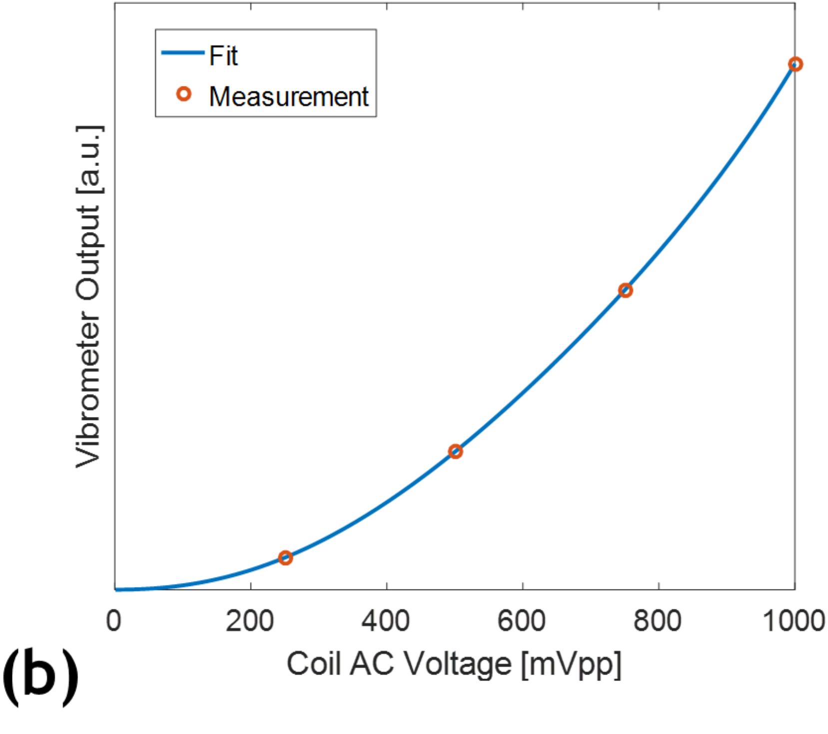

Figure 3.8: (a) Displacement measured at twice the frequency of the magnetic field generated by the Helmholtz coils, showing a peak when the drive frequency is half of the resonance frequency. (b) Peak amplitude measured as a function of the AC voltage applied to the coil. Because the coupling is nonlinear, the displacement varies quadratically with amplitude.

the drive frequency and twice the drive frequency (i.e. the sense frequency). These results are summarized in Figure 3.9. The resonance frequency of the device is slightly different in these plots because the samples were left out in air for over one month between this measurement and the one done in Figure 3.8. As can be seen in Figure 3.9a, the displacement measured at the drive frequency is negligible, but the displacement measured at the sense frequency (Figure 3.9b) is orders-of-magnitude higher as the cantilever resonates in this frequency range. However, examining the voltage output at the drive frequency in Figure 3.9c, there is a flat measured voltage of approximately 10 mV. This voltage can only be due to the electromagnetic crosstalk between the wiring in the vacuum chamber and the Helmholtz coils because the cantilever does not have any appreciable motion in this frequency range. However, in Figure 3.9d, it can be seen that at the sense frequencies, a voltage is measured that follows the same trend as the displacement in Figure 3.9b. This voltage is several orders-of-magnitude smaller

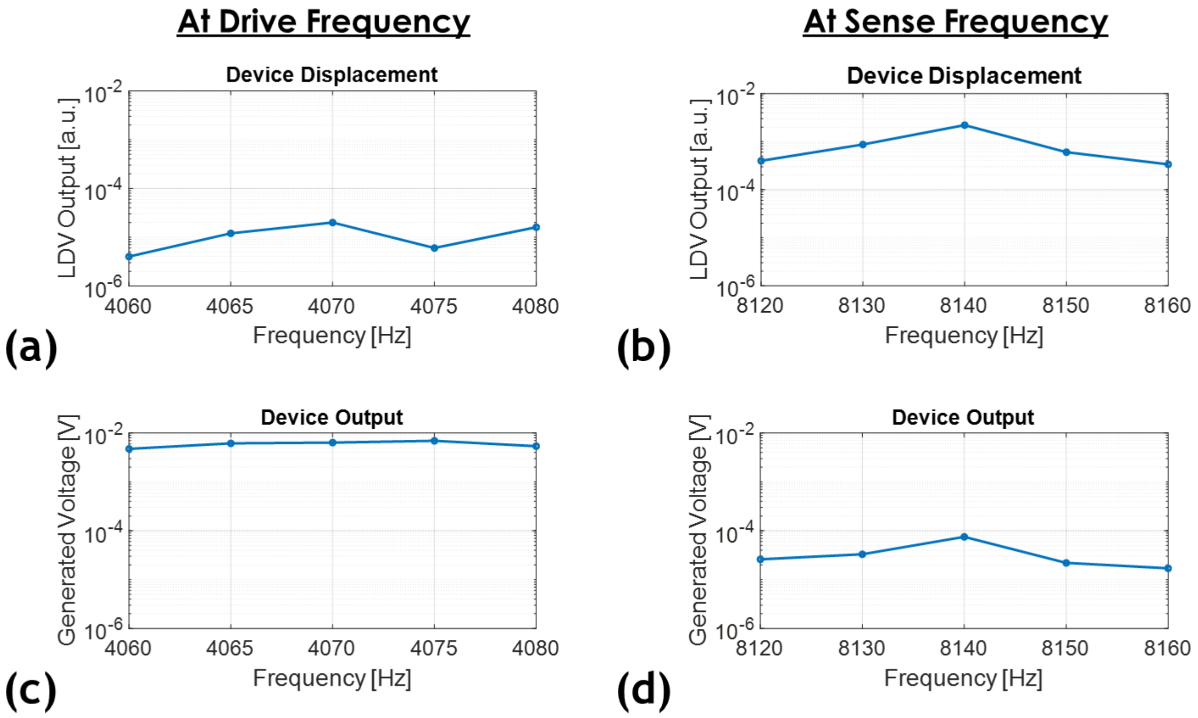

Figure 3.9: (a) Displacement of the cantilever measured at the magnetic field frequency. (b) Displacement of the cantilever at twice the magnetic field frequency. (c) Measured output voltage at the magnetic field frequency. (d) Measured output voltage at twice the magnetic field frequency.

than the voltage measured at the drive frequency (Figure 3.9c). If linear multiferroic coupling would have been used, this measured voltage would have been completely obscured by the electromagnetic interference at the drive frequency. However, because passive nonlinearity was achieved through the perpendicular poling, the device output voltage was able to be measured, demonstrating that this is a viable approach for measuring weak signals from small-scale wireless devices.

3.5 Future Work

The experiments presented in this chapter were only done on samples that were in the remanent magnetic state because no magnetic field was able to be applied inside the vacuum chamber. Future experiments should be done as a function of bias magnitude and angle, to quantitatively study the effect of the magnetic bias on the nonlinear coupling and compare the relative strengths of the nonlinear coupling in both parallel and perpendicular poling.

As these experiments exclusively used multiferroic devices to measure magnetic fields, future designs and experiments should be done to measure field generated by these devices and implement a harmonic RFID system.

There are a number of nonlinear forces and processes that have been demonstrated using flexural MEMS devices [218]. Additional modelling and experiments should be done on how combining the magneto-elastic nonlinearity and the traditional nonlinearities found in MEMS influence the dynamics of these beam structures.

As discussed in Section 3.1.1, wireless multiferroic devices that have been studied have predominantly used devices in the quasi-static regime. For the development of future radio

frequency devices, the behavior of nonlinear multiferroic coupling should be investigated at higher frequencies, specifically in the cut of regime discussed in Section 2.4.4.

Chapter 4 FMR Below Saturation

4.1 Ferromagnetic Resonance in Saturated Films

4.1.1 Acoustically Driven Ferromagnetic Resonance

Recalling the example shown in Section 2.4.2, biasing a magnetic film in-plane will cause it to precess around the bias axis with a natural frequency given by Equation 2.31. If a small AC magnetic field is applied that matches this frequency, the material is driven into ferromagnetic resonance (FMR) and high swings in magnetization are generated (Figure 2.10). This precession is the source of the “rotation” discussed in Section 1.2.1 that is integral to the function of many radio frequency (RF) magnetic devices. Because electromagnetic waves are used to drive FMR, the devices must be on par with the electromagnetic wavelength to operate properly.

Acoustic waves can drive FMR in magnetic thin films through magneto-acoustic interactions, making them a viable option for the miniaturization for RF magnetic devices. Studies on acoustically driven FMR (ADFMR) in multiferroic composites predominantly utilize surface acoustic wave (SAW) devices [173], [174]. A schematic of these devices is shown in Figure 4.1a. The magnetic film thickness is much smaller than the SAW wavelength, so it is approximated that only surface strains couple to the film. If the film is biased in-plane, the effective magnetic field caused by the surface strains is given by simplifying Equation 2.25.

$$\left|\underline{H}_{ME}\right| = -\frac{B_{ME}}{\mu_0 M_s^2} M_x S_{xx} = -\frac{B_{ME}}{\mu_0 M_s^2} M_s \cos(\theta) \cdot S_{xx} = -\frac{B_{ME}}{\mu_0 M_s} \cos(\theta) \cdot S_{xx} \qquad (4.1)$$

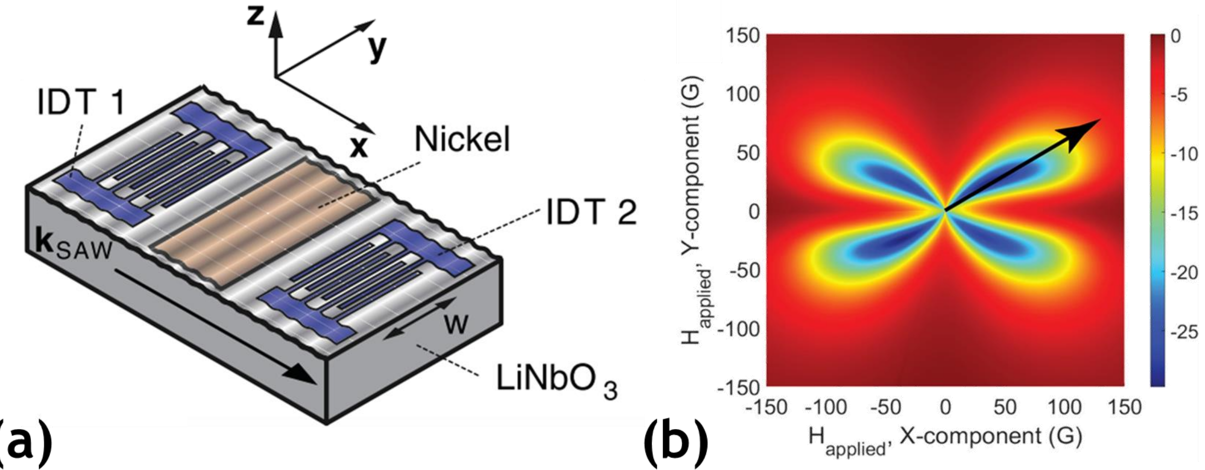

Figure 4.1: (a) Typical SAW device used for ADFMR experiments. Nickel is used as the magnetostrictive thin film and $LiNbO_3$ is the piezoelectric substrate. Adapted from [174]. *(b) Angular dependence of SAW attenuation in ADFMR. Peak attenuation is measured at about 40°. Figure from* [173].

Here, θ is the angle of the magnetic bias relative to the x-direction, which is the direction of SAW propagation. However, as discussed in Section 2.2.1, only the component of magnetic field perpendicular to the bias direction has any effect on the dynamics.

$$\left|\underline{H}_{ME,\perp}\right| = -\frac{B_{ME}}{\mu_0 M_s}\cos(\theta)\cdot S_{xx}\cdot\sin(\theta) = -\frac{B_{ME}}{2\mu_0 M_s}S_{xx}\cdot\sin(2\theta) \tag{4.2}$$

As is the case of regular magnetic field driven FMR, strains parallel to the magnetic bias direction cannot drive the magnetization. However, due symmetry of axial strains (a material has the same strain whether it is examined from the positive or negative direction), a strain that is perfectly perpendicular to the magnetization will also be unable to drive FMR. In ADFMR devices using SAWs, the maximal effective field is achieved when the magnetic field is 45° from the strain axis. This has been seen in ADFMR experiments by characterizing magnetic field dependent acoustic wave attenuation, where the highest amount of attenuation (corresponding to the highest magnetization amplitude) is found to be approximately 45° (Figure 4.1b).

4.1.2 Coupled Magneto-Elastic Resonance

When a magnetostrictive material is strained, this strain causes a reorientation of the magnetization. However, by Equation 2.26, the changing magnetization will also generate a magnetostrictive stress. This leads to a back-action, where the changing magnetization modifies the mechanical strains that caused the magnetization to change in the first place. This bidirectional coupling between the equations of motion for mechanics and magnetics can be ignored in situations where the interaction is weak, but accurate modelling of high coupling systems require that it is included [219].

Because of their narrow bandwidth, high quality factor multiferroic resonators can resolve dynamics that are unseen in ADFMR experiments using SAW delay lines. One such experiment is that done by Alekseev et al. using high overtone bulk acoustic wave resonators (HBARs) [184]. The HBAR resonators where yttrium iron garnet (YIG) and tilted zinc oxide (ZnO) are used as the magnetostrictive and piezoelectric layers, respectively. Tilted ZnO is used here because of its ability to generate both shear and longitudinal bulk acoustic waves. The waves in the HBAR structure travel out of the plane of the film, so shear waves are useful because they can drive FMR with an in-plane bias. At the mechanical resonance frequency, the strains in the device are maximized, inducing the highest possible magnetostrictive magnetization change. At FMR, the magnetization change is also maximized, inducing the highest possible magnetostrictive strains. When the magnetic bias field is chosen such that these frequencies overlap, due to the strong bidirectional multiferroic coupling in the device, mechanical resonance and FMR act as a pair of coupled resonators and split into a pair of coupled magneto-elastic resonance modes. Figure 4.2 summarizes the results of Alekseev et al. As the magnetic field increases, the FMR frequency aligns with the mechanical resonance frequency, and the pair of magneto-elastic resonances manifest as dips in the return loss. As the bias is increased

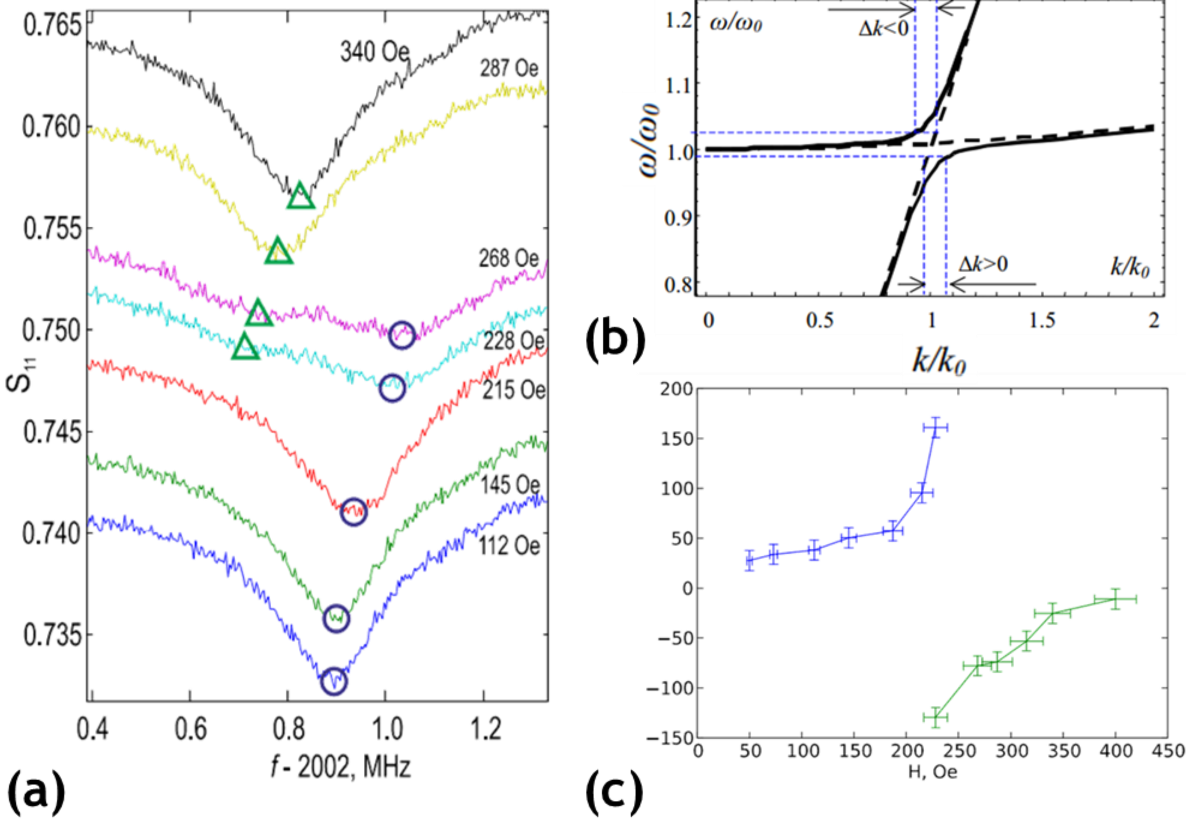

Figure 4.2: (a) Return loss of a multiferroic HBAR resonator in the regime of maximized multiferroic coupling. (b) Dispersion relation of magneto-elastic waves. (c) Plotted resonance frequency shift versus bias magnetic field. The trends here recreate the magneto-elastic dispersion curve, indicating strong bidirectional coupling between the mechanical resonance and FMR. Adapted from [184].

further, the pair of magneto-elastic modes increase in frequency until the coupling is so weak that all that is seen is a single mechanical resonance mode at the original frequency. Plotting the frequency of the dips in the return loss versus magnetic field (Figure 4.2c), the curves recreate the trends of the magneto-elastic wave dispersion curves shown in Figure 4.2b.

4.2 Ferromagnetic Resonance in Multi-Domain Films

While the findings of the ADFMR experiments done to date are critical for the design of future magneto-acoustic devices, these experiments have the common limitation of requiring

a saturated magnetic film. This puts a lower limit on the operating frequency of any device requiring ADFMR.

While saturation maximizes the FMR response, it is not necessary to achieve FMR. Spins will precess at whatever frequency the local magnetic field dictates. Below saturation, the material will break into multiple domains and the internal field will vary as a function of space, meaning the FMR frequency in each domain will be different. This is further complicated by the fact that the domains will dynamically couple to each other [71].

Full analysis of an arbitrary multi-domain material using Equation 2.18 is very complex, but several examples have been worked out in [71] for simple domain structures. Figure 4.3 summarizes the results for an unsaturated ferromagnetic single crystal sphere with a cubic crystal structure. The material is initially in a layered domain state of two different types of domains, and the material converges to a single domain state as the bias field increases toward saturation. Below saturation, there are now two different FMR modes in the magnetic material. One corresponds to the typical FMR mode, which is actuated by an AC magnetic field perpendicular to the bias magnetic field. The second mode is unique to the unsaturated state and is driven by an AC magnetic field parallel to the bias magnetic field. As the bias field

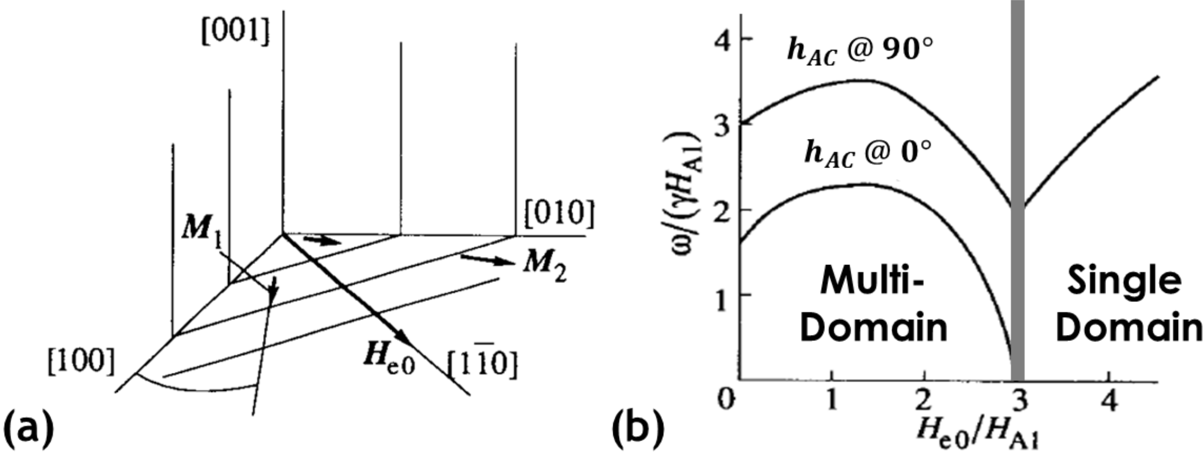

Figure 4.3: (a) Layered domain structure in a single crystal ferromagnet with a cubic crystal structure. (b) Magnetic resonant modes of (a) below and above saturation. Adapted from [71].

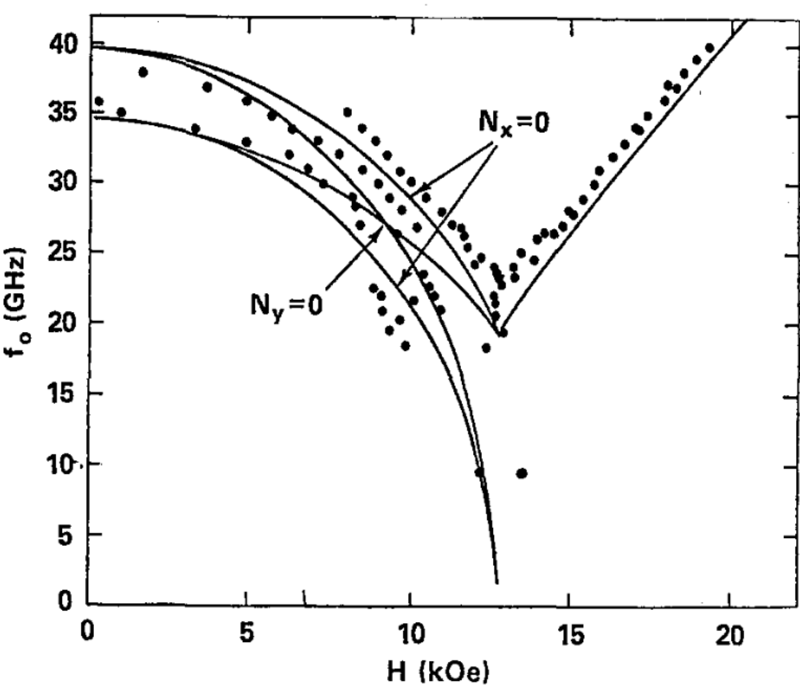

Figure 4.4: Measured magnetic resonance frequencies versus magnetic field for a single crystal sample below and above saturation. The two curves are for applied fields in two different directions. Figure from [220].

increases, the frequency of this new parallel mode decreases until it completely disappears at saturation and leaves only the traditional perpendicular mode associated with single domain materials. This is a major advantage for operating below saturation as it relaxes the constraints of traditional FMR devices on their geometry because the AC magnetic field must be perpendicular to the bias. The presence of these two modes have been experimentally verified in several experiments, with the results of an experiment similar to configuration in Figure 4.3 plotted in Figure 4.4 [220].

The results shown in Figure 4.3 and Figure 4.4 are for single crystal materials. In a polycrystalline material, the domain structure will be very irregular and randomly oriented. As a result, the clean curves shown in Figure 4.3b will be smeared and instead of two resonances, all that will be seen is one single very broad peak.

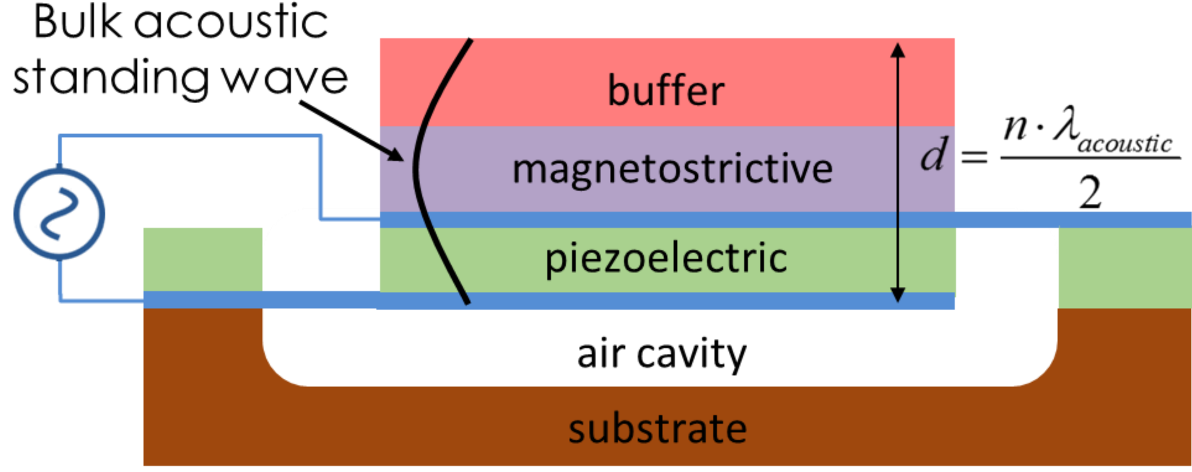

Figure 4.5: Schematic of the thin film bulk acoustic wave resonator used to characterize spin precession in a multi-domain ferromagnetic material.

4.3 Experimental Approach

4.3.1 Device Design and Fabrication

To investigate multiferroic coupling in a multi-domain magnetic material in the spin precession regime (i.e. at FMR), thin film bulk acoustic wave resonators (FBARs) were designed (Figure 4.5) and fabricated (Figure 4.6). The device is a three-layer FBAR, with aluminum nitride and nickel as the piezoelectric and magnetostrictive layers, respectively. The aluminum nitride is used to generate an oscillating out-of-plane extensional strain throughout the device. The topmost layer is a silicon nitride buffer layer whose purpose is to push the peak of the acoustic wave closer to the center of the device, to increase the magneto-elastic coupling to the nickel. The nickel is also patterned into stripes in an attempt to lower eddy current damping.

First, titanium (10 nm) / platinum (100 nm) is evaporated on 4” (100) high resistivity (>10 kΩ·cm) silicon wafers, using a CHA Solution Electron Beam evaporator, to serve as the bottom electrode for the device and is patterned via a lift-off process. The titanium serves as an adhesion layer for the metal. Next, 720 nm of aluminum nitride blanket film is reactively

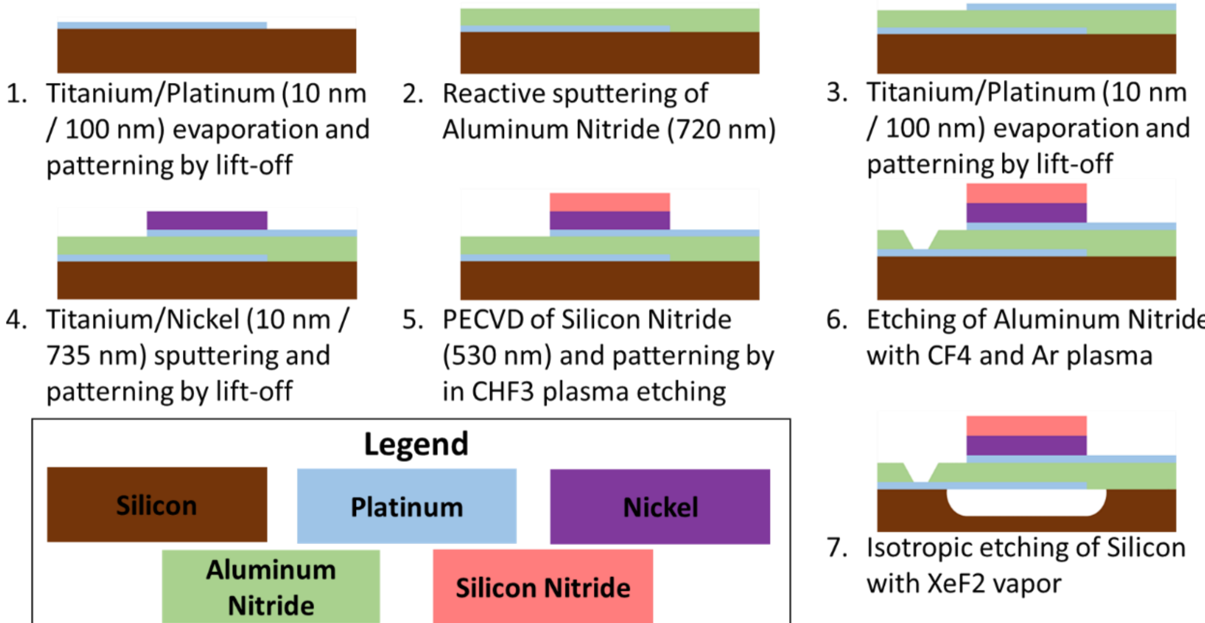

Figure 4.6: Process used for the fabrication of multiferroic FBARs.

sputtered using a Tegal AMS Aluminum Nitride Sputtering System at the Claire & John Bertucci Nanotechnology Laboratory at Carnegie Mellon University. Titanium (10 nm)/ platinum (100 nm) is then evaporated, again using a CHA Solution Electron Beam evaporator, and lifted-off to pattern the top electrode layer. During the patterning of the photoresist for this step, the aluminum nitride was exposed to a TMAH based photoresist developer. TMAH etches aluminum nitride and lead to the roughness seen in the final result [221].

Sputter deposition of titanium (10 nm) / nickel (735 nm) layer follows using an Ulvac JSP 8000 sputtering system, which is also patterned through a lift-off process. The gas pressure for the nickel deposition was tuned to minimize residual film stress and to avoid the "winging" effects typical of sputter lift-off process by keeping the mean free path of the sputtered nickel long (Figure 4.7). Following nickel deposition, 530 nm of silicon nitride is deposited via PECVD with an STS Multiplex PECVD system and then etched in CHF_3 plasma using an STS MESC Multiplex Advanced Oxide Etcher. The aluminum nitride layer is then etched in a mixture of CF_4 and Ar

plasma using an STS MESC Multiplex Advanced Oxide Etcher to expose the silicon and bottom electrode pads.

The devices are then released from the substrate using XeF2 gas phase etching of the silicon using a custom etching system. During this step, the silicon nitride was unintentionally

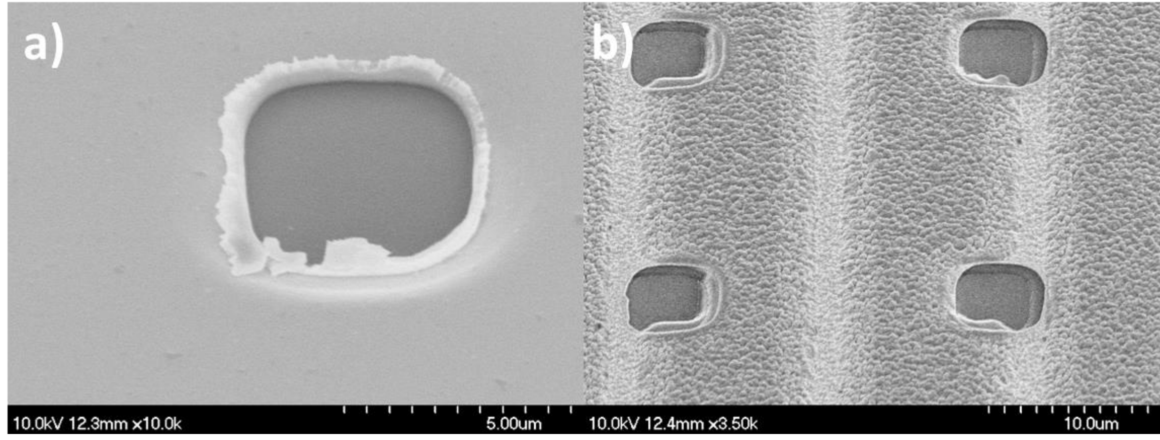

Figure 4.7: (a) Nickel lift-off pattern showing "winging" effects due to conformal sputter deposition. (b) Nickel lift-off of stripes with deposition process tuned to give larger Ni mean free path during deposition. The effects of shadowing can be seen on the edges of the stripes by the discoloration.

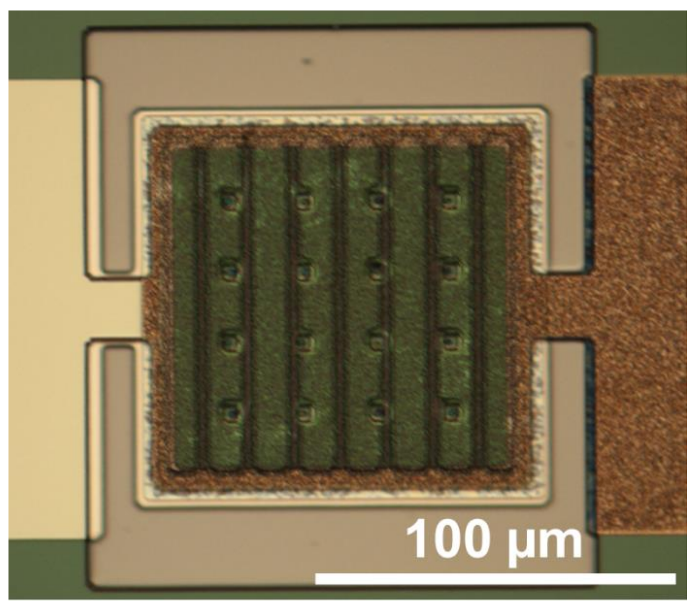

Figure 4.8: Microscope image of a multiferroic FBAR device before XeF2 etching. Notice that the top electrode appears brown despite it being platinum. This is due to the roughening of the aluminum nitride surface from its exposure to TMAH.

etched to a thickness of approximately 300 nm. Figure 4.8 shows a completed device before the release step.

4.3.2 Device Characterization

The electrical response of the device was measured using a two-port measurement with a vector network analyzer (VNA) and ground-signal-ground (GSG) probes. Figure 4.9 shows the reflection and transmission coefficients of the device. Three resonant modes are observed: 1.8 GHz, 3.2 GHz, and 5 GHz. Off resonance, the device simply behaves as a capacitor. The

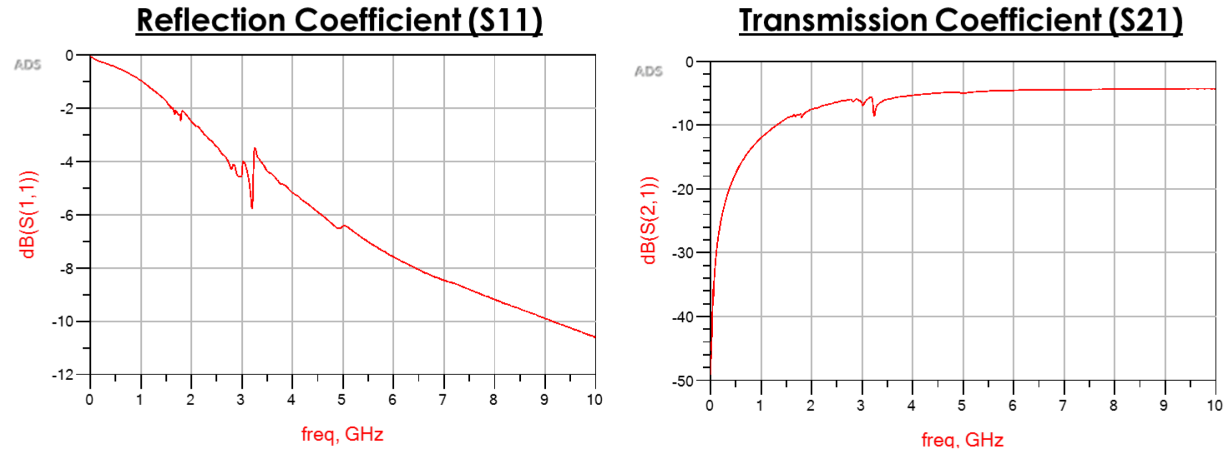

Figure 4.9: Measured reflection and transmission coefficients of the fabricated multiferroic FBAR.

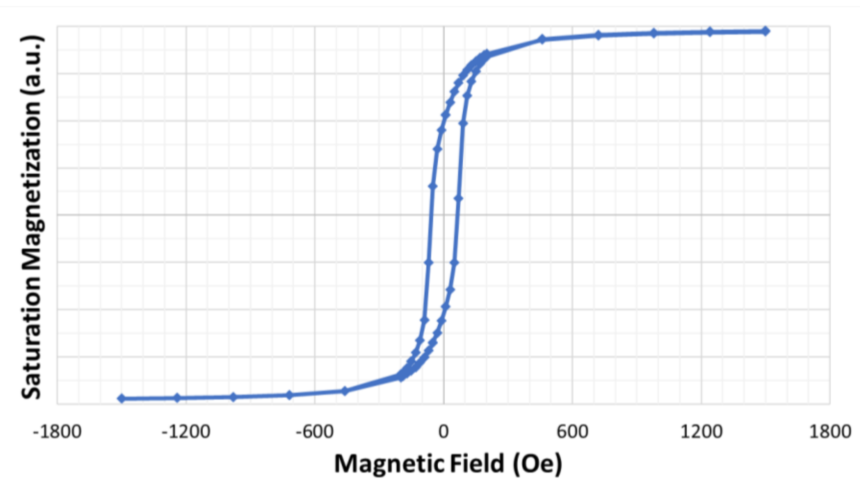

Figure 4.10: Magnetic hysteresis loop for a characteristic nickel sample. Measured using SQUID.

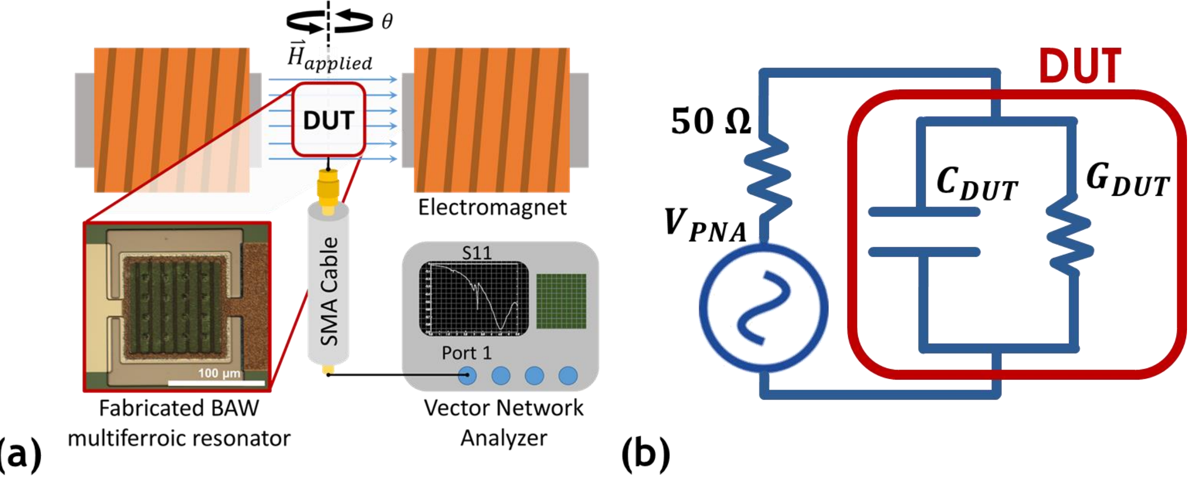

Figure 4.11: (a) Characterization test set up used to measure the S_{11} as a function of bias magnetic field magnitude and angle. (b) Simple circuit model used for data analysis.

magnetic hysteresis loop for a blanket film of nickel on a silicon substrate (using the same nickel deposition process as these devices) is shown in Figure 4.10.

To facilitate measurement with a magnetic bias field, a fabricated device was packaged as the terminating load of a coplanar waveguide (CPW) transmission line, which connects to a VNA via a flange mount SMA connector (Figure 4.11a). As the device is a two-port device, one set of GSG electrodes is shorted via wire bonds to turn it into a one-port device for the electromagnet testing. The packaged device was then placed in an electromagnet where its reflection coefficient, S_{11}, was measured as a function of the applied magnetic field magnitude and angle. Control of the bias angle was made possible by 3D printed mounts. Measurements were made at angles of 0°, 45°, and 85° relative to the plane of the device. To analyze the data, the simple model in Figure 4.11b is used. Change in device conductance, G_{DUT}, is used as to estimate mechanical damping from ADFMR. This model does not consider the electrical response of the CPW line and the wire bonding.

4.4 Experimental Results

Figure 4.12 shows colormaps of the percent change in conductance of the packaged system as a function of the bias magnetic magnitude and the frequencies near the first two resonant modes. The percent change is measured relative to the frequency response at approximately zero magnetic bias, perfect zero bias being unachievable due to nonzero magnetic remanence of the electromagnet poles.

For an in-plane bias, the fundamental resonant mode (1.8 GHz) shows no field dependence of the device conductance (Figure 4.12a). The changes in conductance seen here at high bias were determined to be due to trace magnetic material in the SMA connectors and cables. However, for the same bias field range there are changes seen for the second

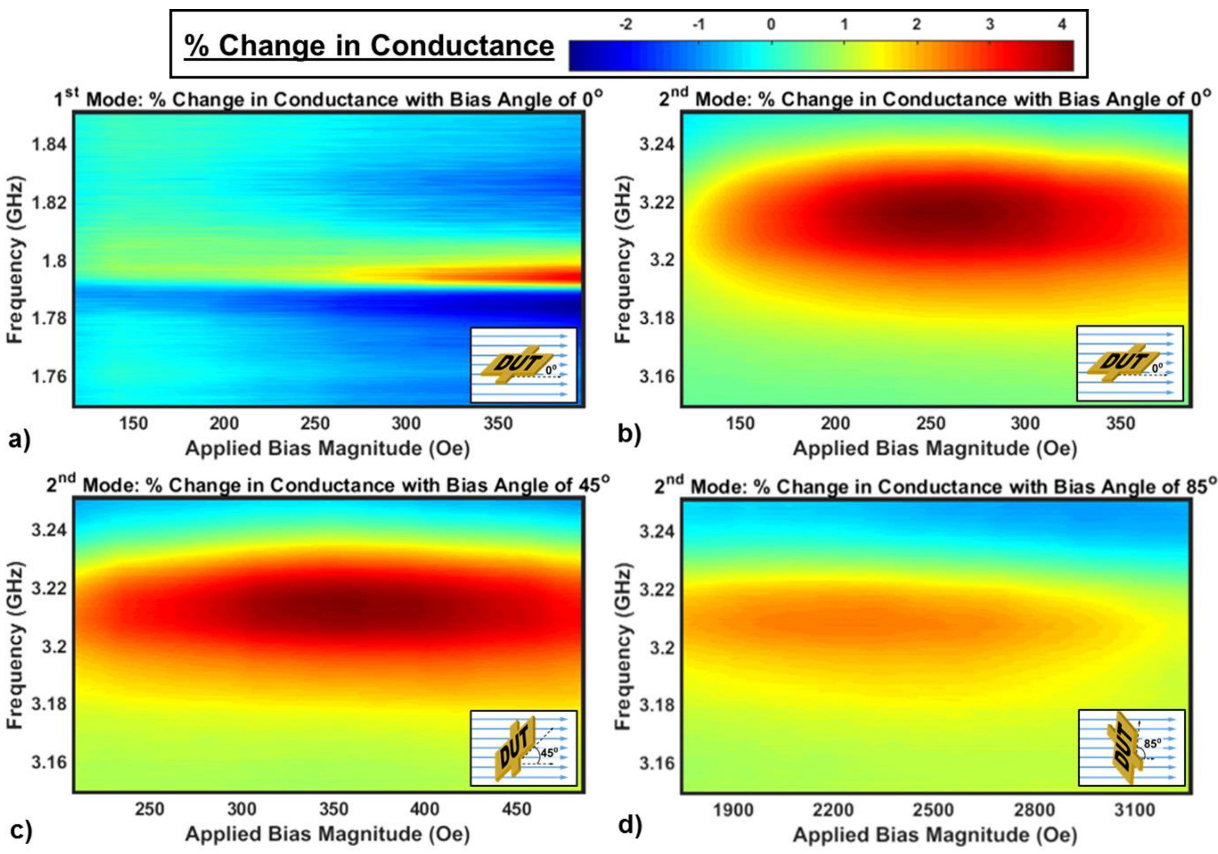

Figure 4.12: Percent change in conductance as a function of frequency and magnetic field. a) At 0° applied magnetic field near 1.8 GHz. b) At 0° applied magnetic field near 3.2 GHz. c) At 45° applied magnetic field near 3.2 GHz. d) At 85° applied magnetic field near 3.2 GHz.

mechanical resonance mode at 3.2 GHz (Figure 4.12b), confirming the frequency dependence of the magneto-mechanical coupling. Here the highest change was found at an applied magnetic bias of 237 Oe, indicating that this bias stimulates FMR at 3.2 GHz. This bias is below saturation for the characterized sample films (Figure 4.10), indicating the device is in the multi-domain state. Coupling is only possible at this angle because the material is in a multi-domain state, as no magneto-elastic coupling is seen at 0° for a single domain film (Figure 4.1b).

When the bias moves out-of-plane a higher magnetic field is needed to stimulate FMR due to the increase in demagnetization energy. As discussed in Section 2.3.1, the internal demagnetization field opposes the external field, which lowers the total bias magnetic field felt by the spin. To stimulate FMR at the same frequency, a larger external field must then be applied. For a thin film, this demagnetization field only exists out-of-plane and gets stronger as the external field rotates more out-of-plane. At 45°, the peak conductance at 3.2 GHz was found to be at 361 Oe. At 85° a much higher field is needed, with the peak conductance occurring at a bias of 2320 Oe.

To confirm that this effect is due to magneto-elasticity, micro-magnetic simulations were done in the Object Oriented MicroMagnetic Framework (OOMMF) developed by NIST to estimate the magnetic susceptibility of the film [222]. To keep the simulation time manageable, a simplified magnetic structure is used in the model. Nickel squares of 50 μm × 50 μm (instead of stripes) and 500 nm thick (instead of 735 nm) were simulated with an approximate cell size of 100 nm × 100 nm × 50 nm were used to make simulations faster, at the cost of accurately accounting for the short-range exchange interactions.

The nickel thin film is stimulated by an RF magnetic field at the frequency of the resonant mode of interest. The magnitude of the applied DC magnetic field is then stepped through values within the range applied during measurement. Once the average magnetization

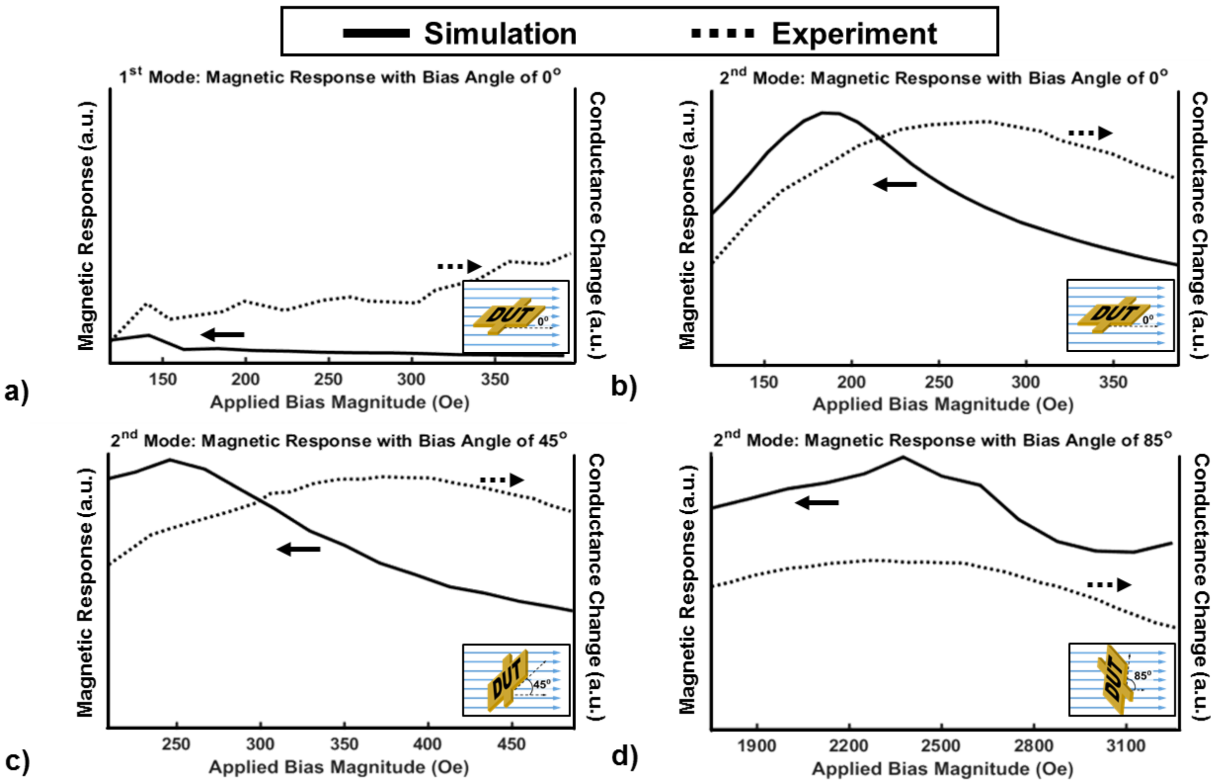

Figure 4.13: Simulated magnetization response (solid line) compared to percent change in conductance at the mode frequency (dashed line) as a function of magnetic field.

reaches as steady-state oscillation for several cycles, amplitude of the steady-state oscillation is then recorded as a function of magnetic field. These values are shown as solid lines in Figure 4.13. The dashed lines in these plots are the normalized absorption of the measured devices at the mechanical resonance frequencies. Maxima in these curves indicate a bias that aligns the magnetic resonance to the mechanical resonance frequency. At 1.8 GHz no significant magnetic response was seen in the model (Figure 4.13a), as was the case for the experiment (Figure 4.12a). This is likely due to the bias required to achieve FMR at 1.8 GHz being too low to put the material in a domain state with enough order to achieve coherent oscillation.

The bias fields corresponding to the maximum change in conductance follow the same trends of the FMR response estimated by the OOMMF model and match the simulated values within 30% or less. Discrepancies between measurement and modelling are expected as

crystallographic, geometric, and exchange effects are not included in the model. However, the matching trends of maximum conductance and simulated susceptibility with respect to bias angle strongly suggests that this effect is due to FMR within the magneto-elastic layer.

4.5 Future Work

Future work should focus on more accurate extraction of the ADFMR coupling in the FBAR devices. Specifically, a deembedding method must be developed to remove the electrical response of any wire bonds and the testing PCB. Modelling should be done to anticipate the effect of the ADFMR coupling on the measured electrical response, and an equivalent circuit model for the measured data should be developed. This would prove useful for any future system level designs that would incorporate multiferroic resonators. Experiments should be done at several power levels to examine any effects of nonlinearity.

Multiferroic FBARs should be fabricated with an improved version of the fabrication process used in this work to minimize surface roughness. Higher quality devices would have sharper resonances and have the possibility of revealing the coupled magneto-elastic modes discussed in Section 4.1.2.

If the domain structure of the magnetic film was set in a controllable way, the distributed ADFMR modes within the device could be predetermined. This would useful for potential applications as frequency selective limiters. These devices achieve broader bandwidths by using a field gradient to have a spatially varying FMR frequency, which allows for the damping of a larger range of frequencies than the narrowband response of FMR.

Chapter 5 Magneto-Acoustic Waves

5.1 Operation Beyond ADFMR

5.1.1 Deviations from ADFMR Model

Acoustically driven ferromagnetic resonance (ADFMR) has been a popular method to study dynamic multiferroic coupling [173]–[175], [223]–[225]. These experiments utilize surface acoustic waves (SAWs) to excite ferromagnetic resonance (FMR) in magnetic thin films via magneto-elasticity. The devices have the advantage of being relatively easy to design, fabricate, and characterize, making experiments based on these devices very attractive for studying dynamic multiferroic coupling. However, there have been several experiments that have delivered results inconsistent with the models developed for ADFMR.

One such inconsistency is the angle of maximum acoustic wave attenuation. The angle for highest coupling in an ADFMR experiment, as derived in Section 4.1.1, is predicted to be 45°. However, there have been experiments where this angle has been measured to be 35° [224] and 40° [173]. Figure 5.1 shows the angular dependence of the ADFMR attenuation of a nickel film for increasing thicknesses. As thickness increases, it can be seen that the deviation from 45° becomes more prominent [226]. In the same work, it has been reported that the same trends occur when increasing the frequency for a fixed film thickness.

Another incontinency is the bias field needed to align the FMR frequency with the SAW frequency. For the ADFMR experiment done in [173], the bias required to align FMR with the

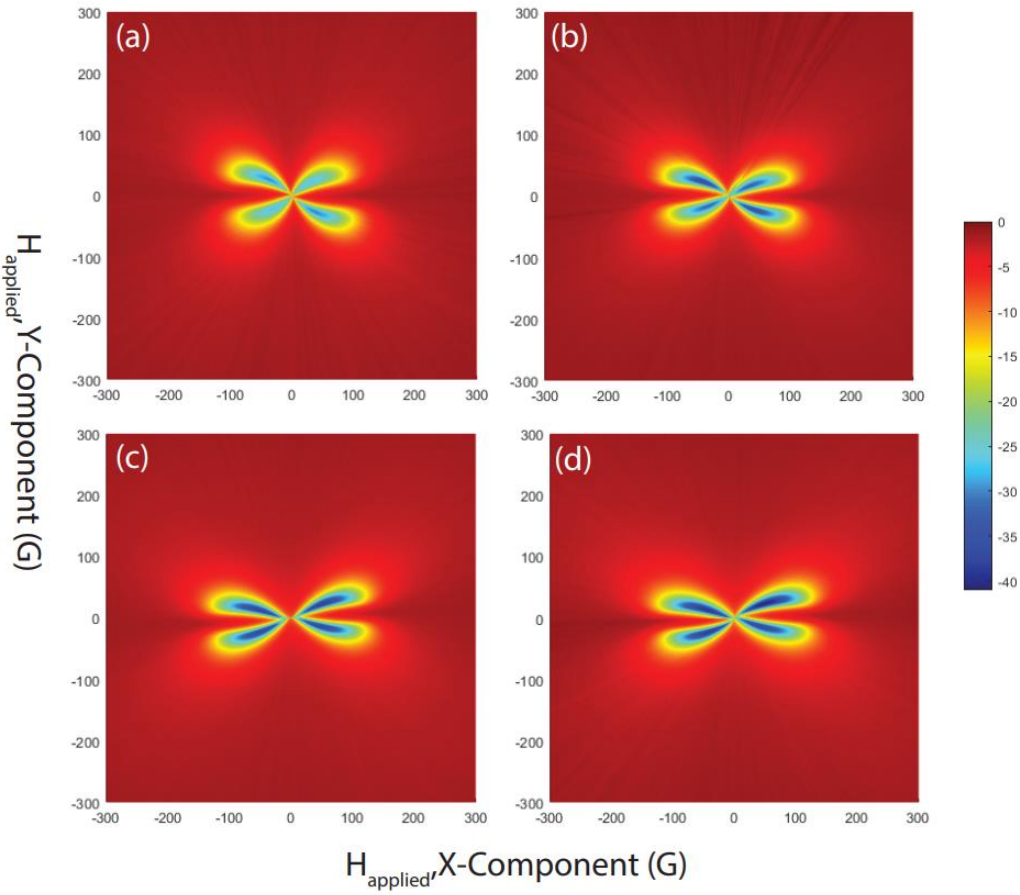

Figure 5.1: Attenuation of SAW by ADFMR for four nickel film thicknesses at 2 GHz: (a) 20 nm, (b) 30 nm, (c) 40 nm, (d) 50 nm. All Samples have a 5 nm gold capping layer. Color bar in units of dB/mm. Figure from [226].

SAW frequency of 1.9 GHz was found to be 50 Oe. However, calculating it for a thin film using the Equation 2.31, the bias should be 75 Oe if excited with a magnetic field. Schneider et al. measured both the bias needed for peak ADFMR damping and the bias needed to excite FMR in their film electromagnetically, and these values were found to be 60 Oe and 100 Oe respectively [223]. Once again, the bias required to excite FMR with a magnetic field is found to be higher than what was measured via ADFMR.

5.1.2 Approximations in ADFMR

As device frequencies and film thicknesses increase, it is clear that the initial models developed for ADFMR break down [226]. In a single domain material, at FMR all spins uniformly

process about the DC magnetic field direction. When using AC magnetic fields to excite FMR, it is required that this field be uniform throughout the material so that all the spins are excited with the same phase. ADFMR is no different, and the models for ADFMR dynamics make two assumptions to ensure a uniform strain throughout the magnetic film [174], [188]. When frequencies and film thicknesses increase, these assumptions become less valid and the magnetic film is no longer driven into a true FMR mode.

The first assumption is that of long wavelength [174]. During an ADFMR experiment, the phase of the acoustic wave will vary down the length of the film and drive each spin with a slightly different time delay (Figure 5.2). If the wavelength is assumed to be long, the phase variation along the length of the film is small, and all the spins will approximately oscillate in unison. However, as frequencies increase, the wavelengths of the acoustic waves will naturally get shorter. In this regime, the oscillations of the spins will no longer be uniform. Recalling the difference between spin precession with (Section 2.4.2) and without demagnetization (Section

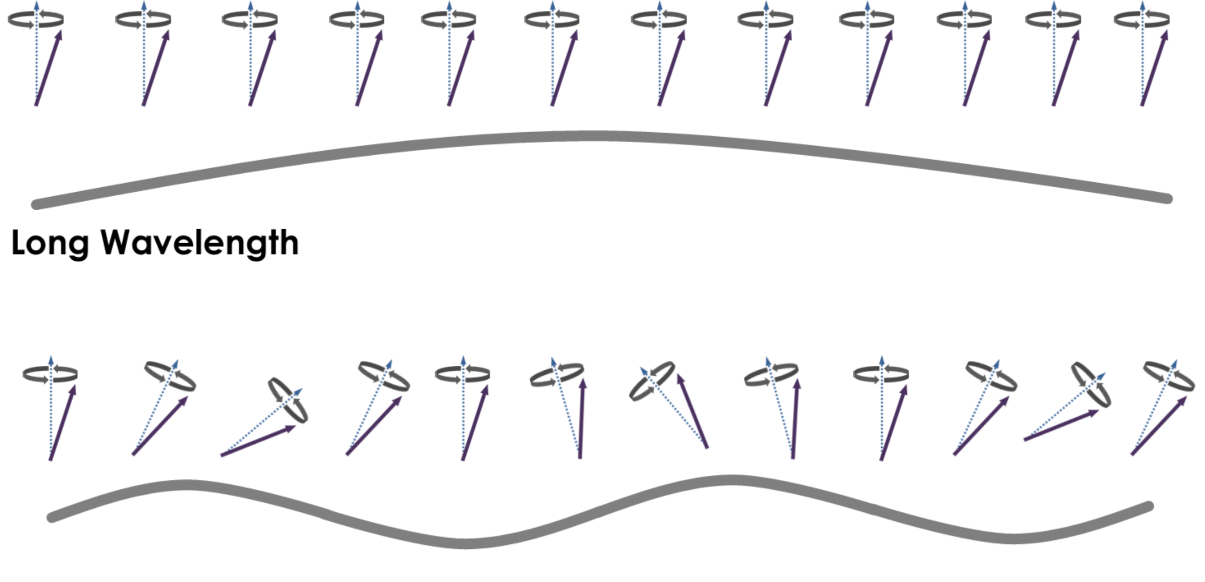

Figure 5.2: Illustration of the difference between the long wavelength and short wavelength regimes on the uniformity of the spin precession.

2.4.1), the presence of dipolar fields results in a shift in the bias field needed for FMR. Gradients in the magnetization results in additional dipolar fields (Equation 2.20), which will lead to an additional shift in the bias field needed for ADFMR absorption. The shorter the wavelength, the larger the gradient and the more appreciable the shift in bias [188]. In addition to dipolar fields, gradients in the magnetization also generate exchange fields (Equation 2.23), but it has been estimated that exchange interactions may not lead to appreciable bias shifts [174].

The second assumption is that of an infinitely thin film [174], [188]. Referring back to the structure used in ADFMR experiments (Figure 4.1), the acoustic wave is predominantly carried in the piezoelectric substrate and only strains near the surface of substrate are transferred to the magnetic thin film. The penetration depth of a SAW into the substrate is on the order one wavelength [86]. If the film is much thinner than the SAW wavelength, then it can be assumed to be infinitely thin. The strain in the magnetic layer is then uniform through the film cross section and is presumed to be identical to the surface strain of the SAW device if the magnetic film was not present. This strain is purely extensional in the direction of SAW propagation, and the effective field is given by Equation 4.2. If the film thickness is increased or the frequency is increased (which decreases the wavelength), the film thickness is no longer a negligible and the assumption breaks down. For a finite thickness, the particle displacement of the SAW will vary through the film cross section and give rise to shear strains in the material. This will add an additional component to the effective field from the magneto-elastic energy, which can be found by using Equation 2.25 (assuming that the bias magnetic field is in-plane at an angle θ relative to the propagation direction).

$$\underline{H}_{ME} = -\frac{B_{ME}}{\mu_0 M_s^2}\left(M_x S_{xx}\hat{x} + 2M_x S_{xz}\hat{z}\right) = -\frac{B_{ME}\cdot\cos(\theta)}{\mu_0 M_s}\left(S_{xx}\hat{x} + 2S_{xz}\hat{z}\right) \qquad (5.1)$$

Recall that only the component orthogonal to the bias magnetic field will have any contribution to the dynamics (Section 2.2.1), making the useful portion of the effective magneto-elastic field given by Equation 5.2.

$$\begin{aligned} \underline{H}_{ME} &= -\frac{B_{ME}}{\mu_0 M_s}\left(\frac{1}{2}\sin(2\theta)\cdot S_{xx}\hat{x} + 2\cos(\theta)\cdot S_{xz}\hat{z}\right) \\ &= -\frac{B_{ME}}{\mu_0 M_s}\left(a_{xx}S_{xx}\hat{x} + a_{xz}S_{xz}\hat{z}\right) \end{aligned} \tag{5.2}$$

The presence of shear adds an effective field in the out-of-plane direction of the film. Figure 5.3 plots the relative angular dependence of the field components in Equation 5.2. The shear component of the magneto-elastic field is seen to peak along the axis of acoustic wave

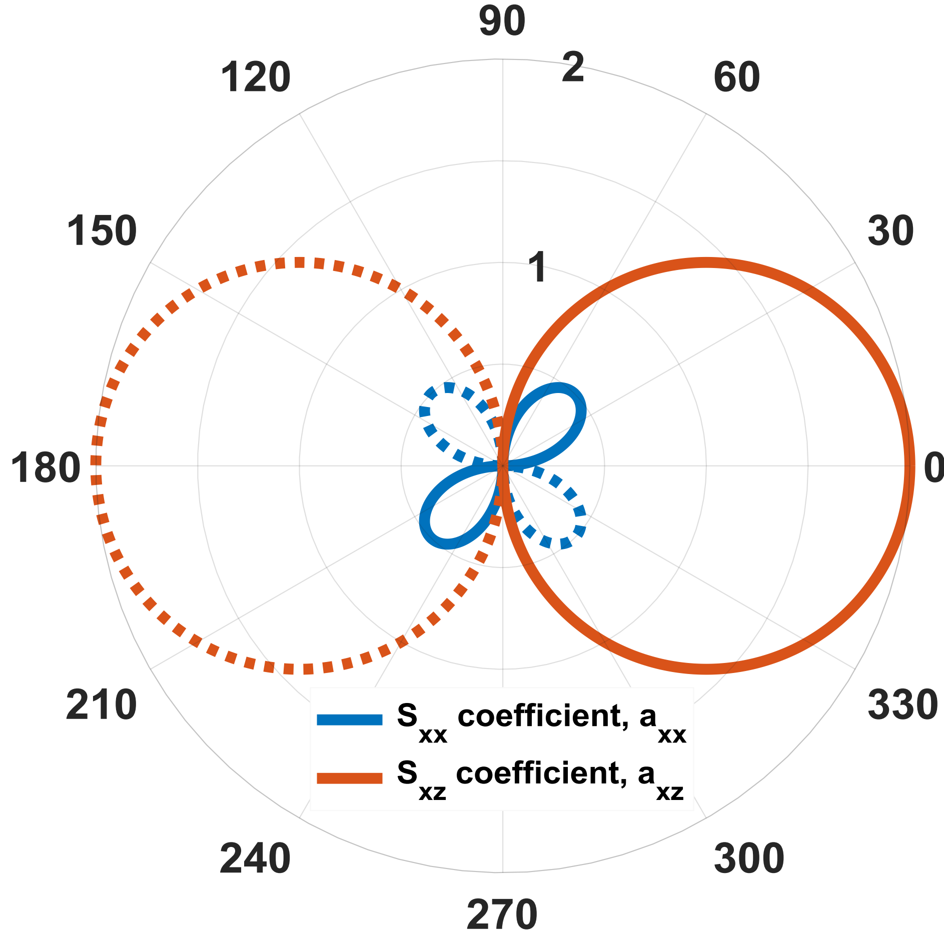

Figure 5.3: Angular dependence of the effective magnetic fields from extensional and shearing strains. Dotted lines represent negative numbers.

propagation. The effect of this is that the peak magneto-elastic coupling will now be at an angle less than 45° relative to the propagation direction, consistent with the experiments discussed in Section 5.1.1. In addition to modifying the angular dependence of the coupling, shear components have also been found to be responsible for nonreciprocal magneto-elastic attenuation in ADFMR experiments [181], [182].

5.2 Acoustic Wave / Spin Wave Coupling

As was discussed in the last section, since the driving strain is nonuniform, a true FMR mode is not possible in a magneto-elastic film. What can be actuated are nonuniform magnetization oscillations, called spin wave modes. Spin waves are waves of magnetization that exist in the spin precession frequency regime beyond FMR [54], [55], [70], [71], [201]. As opposed to FMR, which is transduced with uniform magnetic fields, spin waves are typically induced with meander inductors because they require nonuniformity in the driving magnetic field (similar to the IDT transducers required to generate SAW waves). The wavelength of the magnetic field transduced spin wave is set by the periodicity of the meander inductor, and the frequency will depend on the inductor periodicity and the DC magnetic field. In the case of a magneto-elastic film, the effective field generated by an acoustic wave can be the source of the nonuniform driving field and generate spin waves with strain instead of a meander inductor.

Ignoring any bidirectional coupling between the acoustic wave and spin wave, the dispersion relation for spin waves can be derived by Equation 2.18 by allowing for the AC magnetization to vary as a function of position. Because the magnetization is allowed to vary in space, the gradients of the AC magnetization will give rise to AC micro-magnetic fields from the exchange and dipolar interactions. If, for simplicity, the film edges are ignored and the

material is assumed to be single domain, then the dispersion relation is approximately given by the equation below.

$$\omega = \gamma\mu_0 H_0 + Dk^2 + \frac{1}{2}\gamma\mu_0 M_s \, sin^2\,\theta \tag{5.3}$$

Here θ the angle between the spin wave propagation and the bias magnetic field, and k is the wave vector. One large distinction between Equation 5.3 and FMR frequency derived earlier, is that the frequency of the spin wave depends not only on the bias magnitude but the relative angle between the bias and the spin wave. Ignoring film edges means this material is identical to that of the independent spin system considered in Section 2.4.1, which has an FMR frequency of $\omega_0 = \gamma\mu_0 H_0$. Examining Equation 5.3, it is obvious that the frequency of the spin waves will always be above that of FMR for fixed bias. Conversely, if the frequency is fixed, then ADFMR absorption due to spin waves would happen at lower bias fields than expected for FMR absorption, which is consistent with the experiments detailed in Section 5.1.1. Actuation of spin wave modes instead of FMR has previously been suggested as the reason for this discrepancy by Nygren et al. [175].

The spin wave must match the periodicity of the driving acoustic wave, so it can be assumed that the spin wave will have the same frequency of the acoustic wave and the wave vector must be some odd multiple of the acoustic wave vector. Assuming the wave vector and frequency are fixed, then rearranging Equation 5.3 will yield the relation between the bias needed for the spin wave mode to exist as a function of the bias angle.

$$H_0 = \frac{\omega - Dk^2}{\gamma\mu_0} - \frac{1}{2} M_s \sin^2\theta \tag{5.4}$$

The trend for Equation 5.4 is plotted in Figure 5.4. As the angle increases, the bias field required for the spin wave mode to exist is found to decrease until it hits 90°, at which point it will begin to increase again.

Trend of Bias Magnitude vs Angle for Spin Wave
Fixed Frequency and Wavelength

Bias Magnetic Field [a.u.]

0 15 30 45 60 75 90

Bias Angle [degrees]

Figure 5.4: Analytical model for the dependence of the bias magnetic field magnitude needed for the existence of a spin wave mode as a function of the angle between the bias magnetic field and the spin wave propagation direction, keeping the spin wave frequency and wavelength fixed.

5.3 Experimental Approach

5.3.1 Device Design and Fabrication

To investigate coupling of spin waves with acoustic waves in a single domain material and in the spin precession frequency regime, Lamb mode delay lines were designed and fabricated. An illustration of the device is shown in Figure 5.5. Lamb wave delay lines were chosen because the acoustic waves propagate through a thin film plate, as opposed to SAW devices where the waves propagate along the surface of a substrate. In SAW devices, the waves penetrate about one wavelength deep into the substrate. Lamb wave devices, in contrast, the strains penetrate through the entire thickness of the thin film plate because the plate can be fabricated to be much thinner than the acoustic wavelength. This allows the magnetic thin film

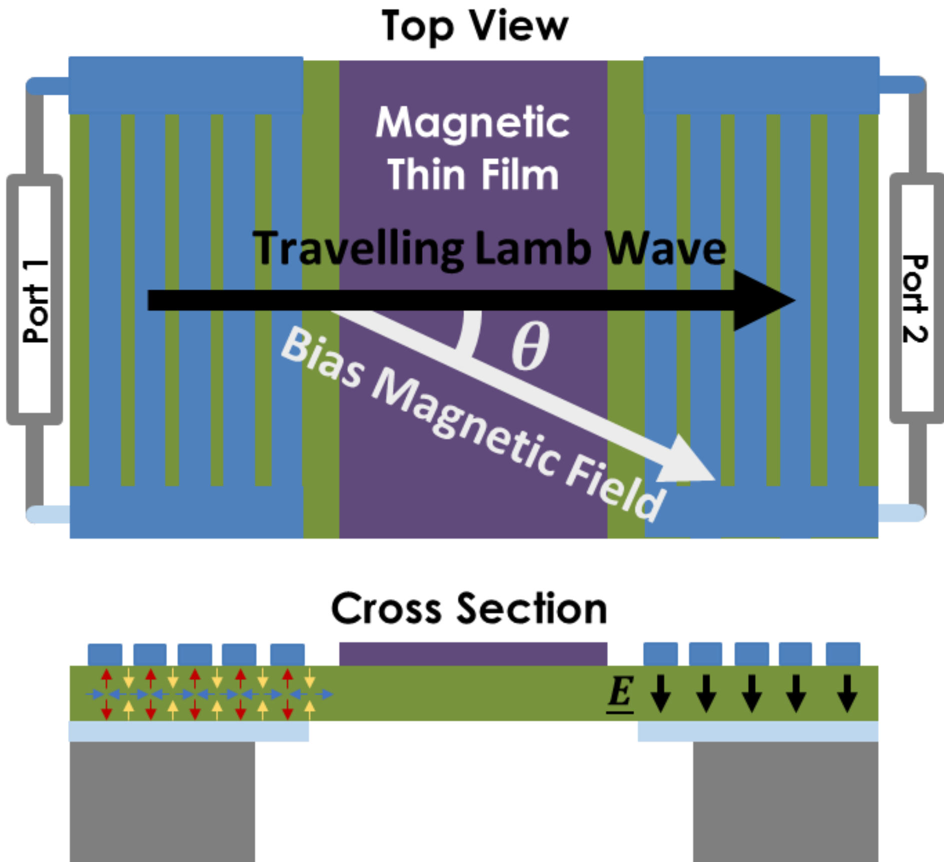

Figure 5.5: Schematic of Lamb wave delay line used for characterization. The angle between the acoustic wave propagation direction and the bias magnetic field applied by the electromagnet is shown as θ. These devices use a shorted grating for the top electrode and a plate for the bottom electrode. The electric field ($\underline{E}$) generated by the electrodes create an axial extensional stress under the electrode strips (red arrows). By the Poisson effect, this creates an in-plane stress (blue arrows). This in-plane stress then creates a negative axial stress between the electrode stripes (yellow arrows). The fundamental mode will have the wavelength half that of a design using traditional IDTs with the same dimensions.

to be a more significant portion of the device cross section and leads to the presence of strong extensional and shearing strains. Instead of IDTs, a shorted grating is used as the top electrode and a plate is chosen as the bottom electrode to actuate higher frequencies while still using contact lithography, at the cost of lower electromechanical coupling. The gap and electrode widths are 3 μm.

The fabrication process (Figure 5.6) begins with 4” (100) high resistivity silicon substrates. Platinum (50 nm) is deposited (with 10 nm of titanium as an adhesion layer) for the

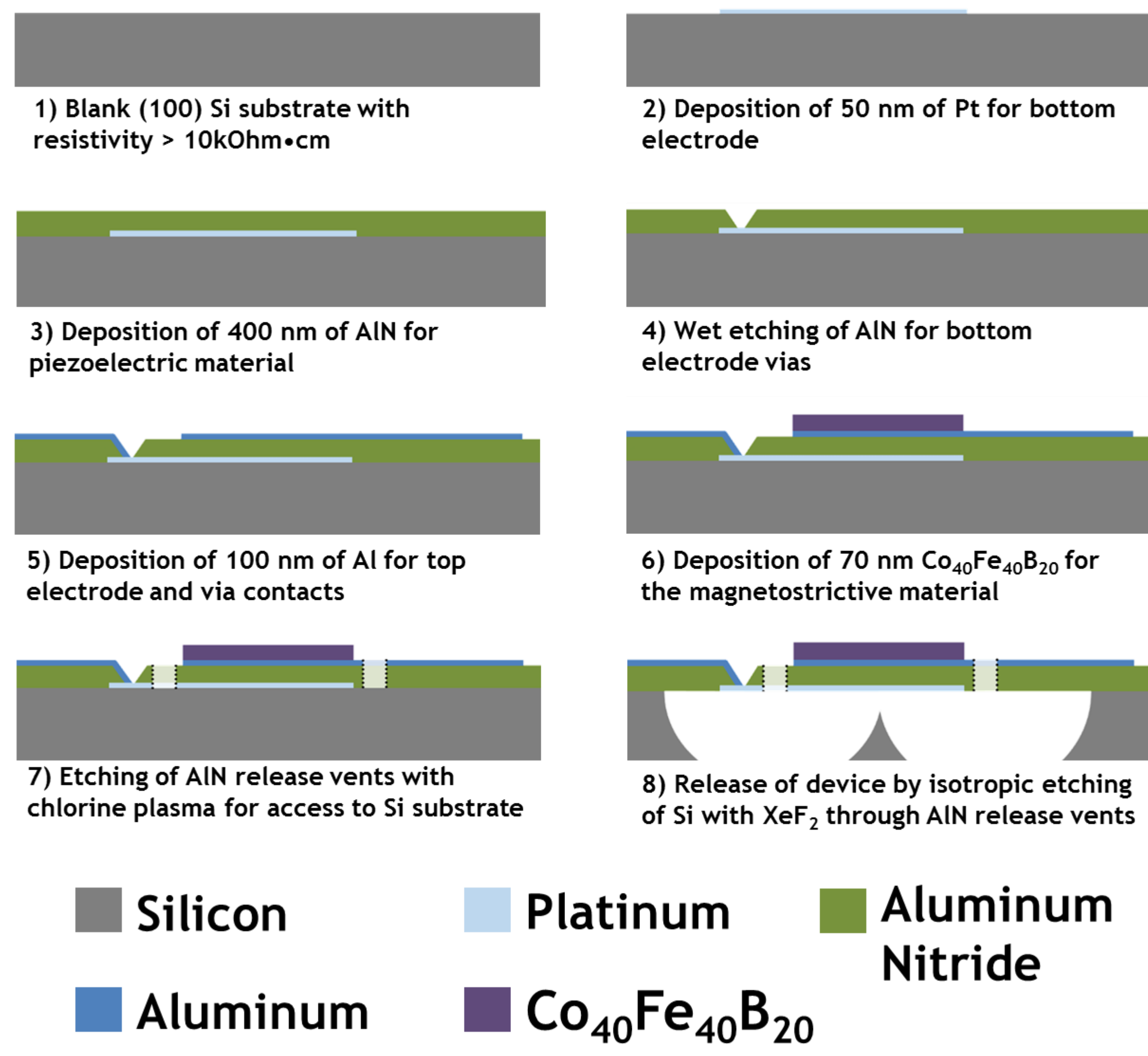

Figure 5.6: Cross sections of the fabrication process for multiferroic Lamb wave delay lines.

bottom electrode by evaporation using a CHA Solution Electron Beam evaporator and is patterned via a lift-off process. An aluminum nitride (400 nm) blanket film is then reactively sputtered with a Tegal AMS Aluminum Nitride Sputtering System at the Claire & John Bertucci Nanotechnology Laboratory at Carnegie Mellon University. Vias for bottom electrode contact are then wet etched with AZ 300 MIF photoresist developer using a KMPR 1005 mask. Titanium

(10 nm) / aluminum (100 nm) for the top electrodes and via contacts is deposited by evaporation with a CHA Mark 40 system and is patterned by lift-off. For the magnetostrictive layer, tantalum (3 nm) / $Co_{40}Fe_{40}B_{20}$ (70 nm) / aluminum (10 nm) is deposited by sputtering at the Chemnitz University of Technology and is patterned into a 144 μm × 144 μm square by lift-off. The tantalum layer serves as an adhesion layer for the $Co_{40}Fe_{40}B_{20}$, as well as promoting amorphous growth of the magnetic film. The aluminum layer is a capping layer to prevent oxidation of the $Co_{40}Fe_{40}B_{20}$ after deposition, as well as protecting it from being etched during the silicon etch at the end of the process. To define the edges of the delay line, the devices are plasma etched using a chlorine gas chemistry with a Unaxis SLR770 ICP system using a KMPR 1005 mask. The wafer is then diced, and the devices are released at the die level by isotopically etching the silicon substrate using XeF_2 gas with a custom etching system. An image of a completed device is shown in Figure 5.7.

5.3.2 Device Characterization

Characterization of the Lamb mode transmission was done by using a PNA-L network analyzer and tungsten ground-signal-ground (GSG) probes to measure the device S-parameters

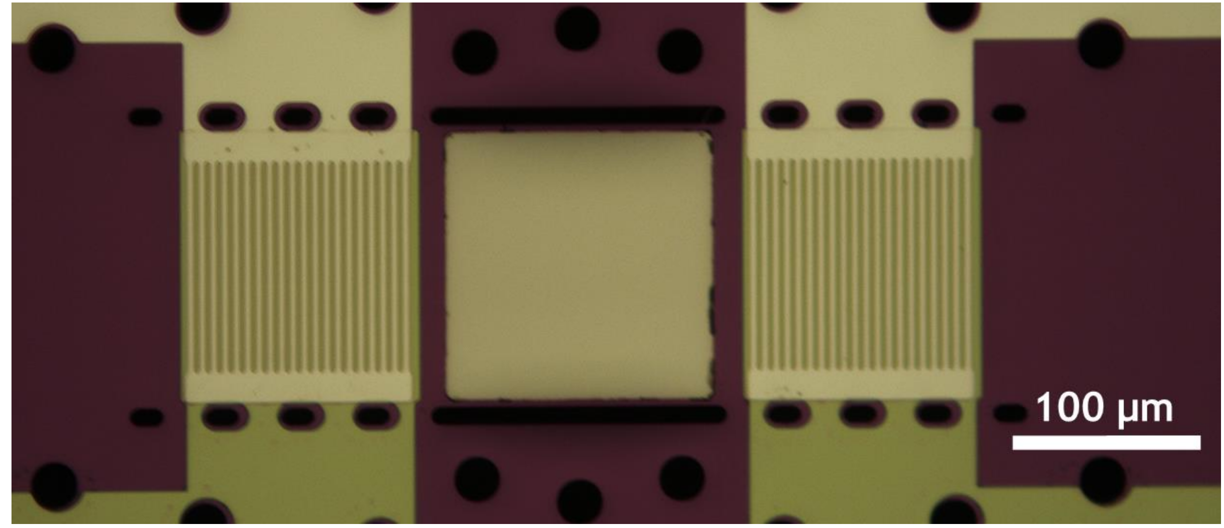

Figure 5.7: Image of released multiferroic Lamb wave delay line. The holes are used to increase the area of the suspended membrane to minimize any acoustic reflections from the edges of the device.

from 5 GHz to 10 GHz. Tungsten probes are necessary to break through the strong native oxide layer that forms on the aluminum electrodes. To maximize the nonuniformity of the strain fields, the device is run at a high harmonic to shorten the acoustic wavelength as much as possible. For this work, a mode at 7.492 GHz is chosen (Figure 5.8a). To remove the effects of electromagnetic feedthrough and acoustic echoes, the S-parameter data is time-gated between 23 ns and 60 ns. COMSOL simulations of the device at this mode reveals an approximately uniform extensional strain and a graded shear strain throughout the magnetic thin film (Figure 5.8bc). The peak magnitudes of the shearing and extensional strains are the same order-of-magnitude.

To test the delay lines under a variable bias magnitude and angle, an RF rotating characterization stage is constructed inside of an electromagnet (Figure 5.9). The device dies are wire-bonded onto CPW lines to make electrical contact and nonmagnetic SMA connectors from Cinch Connectivity Solutions are used to connect to the characterization stage. The characterization stage consists of a Thorlabs CR1 manual continuous rotation stage, a custom 3D printed mount to hold the samples, custom nonmagnetic rigid SMA cables from Phoenix of

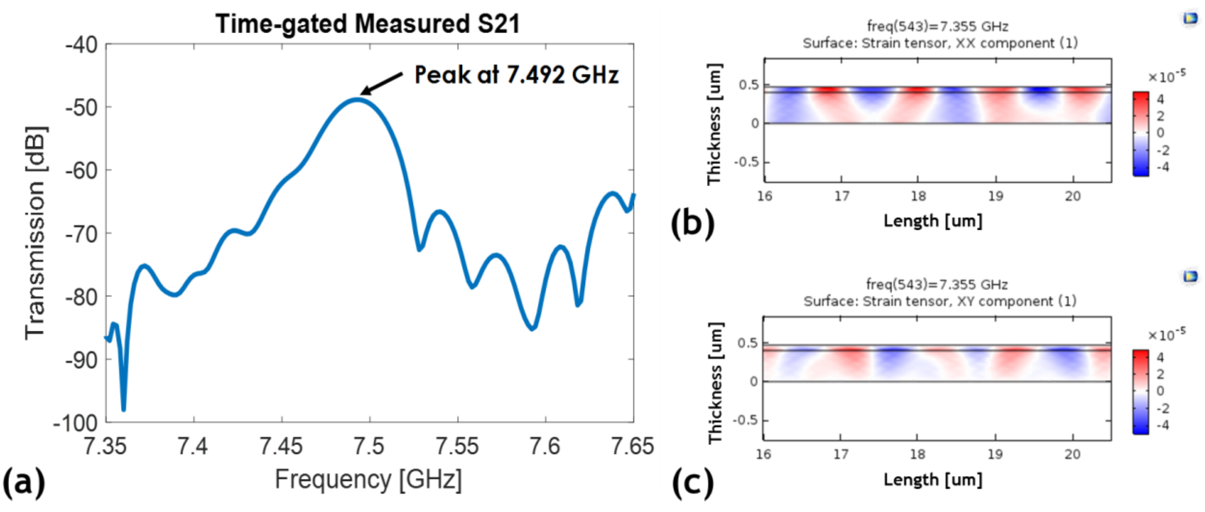

Figure 5.8: (a) Measured Lamb wave transmission, and simulated (b) extensional and (c) shear strains along the length off the delay line for the chosen mode of operation.

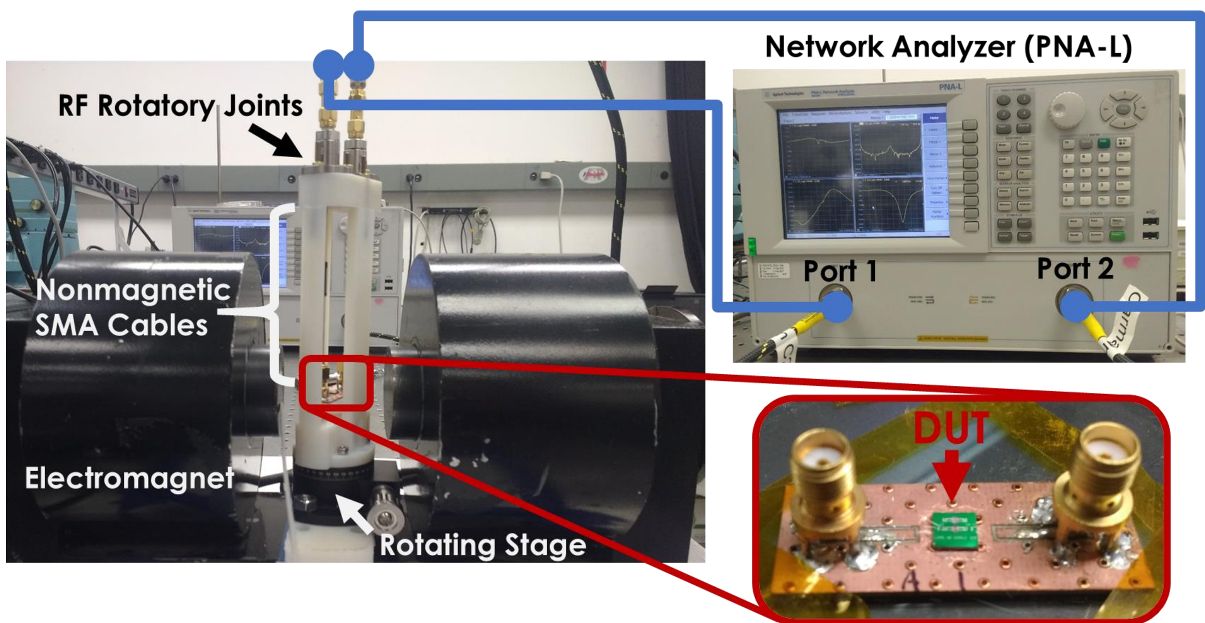

Figure 5.9: Experimental set up used for characterization of Lamb wave delays lines. The inset figure is the device mounted on to the CPW used for characterization.

Chicago, and RF rotatory joints from Pasternack to prevent the cabling from disconnecting during rotation. The rotating characterization stage is then connected to a PNA-L network analyzer to measure the device S-parameters for every combination of magnetic bias magnitude and in-plane angle for the experiment. Time-gating is again used to minimize the impact of electromagnetic feedthrough and acoustic reflections on the measured data.

5.4 Experimental Results

Shown in Figure 5.10 is a representative plot of the measured magnetic field dependence of the transmission coefficient at 7.492 GHz. As the magnetic field is increased, eventually the spin wave matches the acoustic wave in wavelength and frequency. This leads to increased damping of the acoustic wave as energy is dissipated by the spin wave and manifests itself as a dip in the transmission coefficient. The peak is likely caused by an increase in acoustic velocity from the magneto-acoustic back-action [227]. The bias magnetic field at which this dip occurs

Change in Acoustic Transmission as a Function of Field Bias 30 degrees Relative to Propagation Direction

Δ|S21| [dB]

Magnetic Field [Oe]

Figure 5.10: Change in S_{21} of the chosen acoustic mode, 7.492 GHz, as a function of the DC magnetic field at an angle of 30˚. Attenuation of the acoustic wave by the magnetic thin film maximizes near 250 Oe, indicating the presence of a spin wave mode that matches the acoustic wave wavelength and frequency.

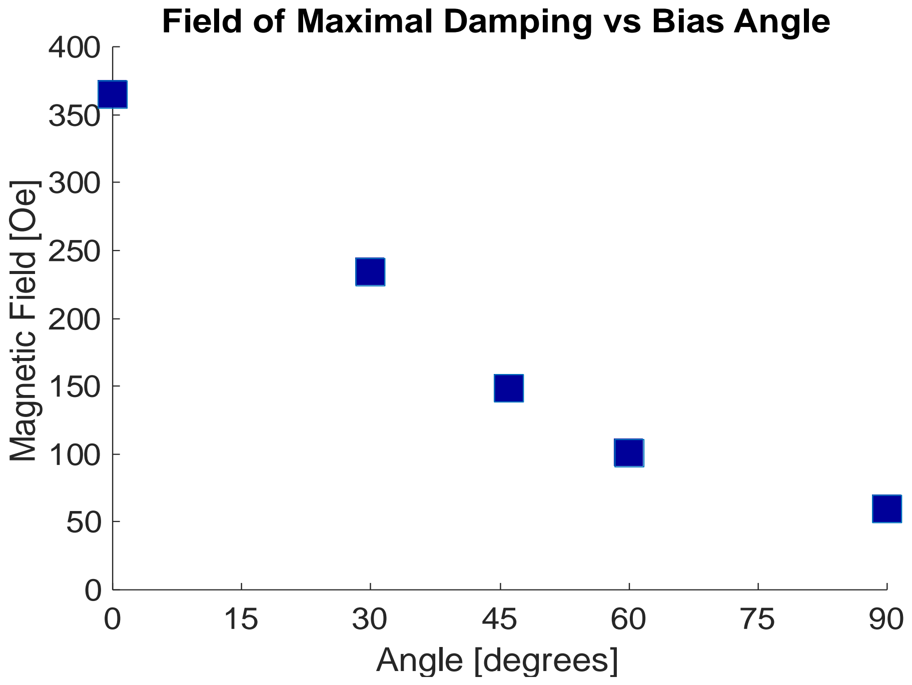

Figure 5.11: Measured magnetic field for maximal damping of the acoustic wave versus angle of the magnetic field relative to the Lamb wave propagation direction.

for each angle of the experiment is plotted in Figure 5.11. As the angle of the magnetic field increases, the bias field of the maximal damping point decreases, which is the same trend as predicted for the spin wave dispersion (Figure 5.4). This is in stark difference with previous work in SAW excitation of FMR, where the bias magnetic field for maximal damping show no dependence on the angle for isotropic materials [173], [174].

5.5 Future Work

To study the dynamics of the spin wave / acoustic wave coupling, models need to be developed to consider the back-action of the magnetic layer on the Lamb wave. In the structures studied in this work, the magnetic layer contributes a significant fraction of the device cross section, making models developed for ADFMR using SAW devices insufficient.

The work presented in this chapter focused on attenuation of the acoustic waves. As shown in [70], [227], magneto-acoustic waves have a velocity dependence on the spin wave coupling. Future work should study the magnetic field dependent phase change of the structures to characterize the velocity shifts. This will also be required to accurately characterize the damping of the magneto-acoustic interactions, as the amount of damping caused by the magnetic film will depend on the velocity of the wave passing through it.

As discussed in Section 5.1.2, shearing strains in SAW based ADFMR experiments have shown to lead to nonreciprocal attenuation of the acoustic waves. Lamb wave delay lines are anticipated to have stronger nonreciprocity because the magnetic film is a more significant portion of the device cross section, yielding larger shearing strains. Work should be done to recreate the experiments done in [181], [182] with Lamb mode devices. Because of their higher

electromechanical coupling, Lamb wave devices hold more promise than SAW devices for the realization of high frequency multiferroic devices.

Chapter 6 Conclusions

Dynamic multiferroic coupling has recently garnered much interest for the development of micro-scale radio frequency magnetic devices. Magnetic devices have not seen nearly as significant miniaturization as their electronic counterparts but, by leveraging past research in magneto-acoustics and recent developments in piezoelectric micro-devices, multiferroics offer a route to significantly reduce the footprint of radio frequency magnetic devices. The dynamics of magnetic materials can be separated into several regimes based on their internal structure and frequency of operation. Thus, to develop future micro-magnetic devices using multiferroics, multiferroic coupling must be investigated across these regimes.

In this work, nuances of dynamic multiferroic coupling in three distinct regimes of dynamic magnetization are studied. Nonlinearity in multi-domain quasi-static cantilevers is demonstrated by poling the magnetization perpendicular to the AC magnetic field. Using this technique, it was found that the passive nonlinearity of this configuration enables measurements of weak signals that would otherwise be drowned in electromagnetic interference. Magneto-elastically driven ferromagnetic resonance in multi-domain samples is investigated, and it was demonstrated that strains orthogonal to the magnetic bias can excite magnetic resonance. This is in sharp contrast with similar experiments done in single domain materials, where no coupling is seen at this angle, and opens the door to alternative geometries for systems where the constraints of the single domain geometry are too restricting. Magento-acoustic interactions in Lamb wave delay lines are studied and it is found that large nonuniformities in the strain fields lead to large deviations from the models traditionally used

for acoustically driven ferromagnetic resonance. These results are important for the future development of high frequency multiferroic devices, where the short wavelengths necessitate the use of nonuniform strain fields.

Appendix A1 Fabrication Notes

A1.1 Lithography

A1.1.1 Silicon

The process given in Figure A1.1 is used for lift-off patterning of thin films on bare silicon substrates. To make lift-off easier, AZ nLof 2020 is chosen because of its pronounced negative

#	Process Step	Notes
1	Wafer cleaning (Acetone, Methanol, IPA, DI water)	Avoid sonication if high aspect ratio features are on the wafer because they can be damaged.
2	Dehydration on hotplate	15 minutes @ 150 °C
3	HMDS vapor coat	10 minutes
4	Spin on AZ nLof 2020	Spray with nitrogen to clean off any debris. 500 RPM @ 100 RPM/s for 5 seconds (spread) 3000 RPM @ 1000 RPM/s for 30 seconds (leveling)
5	Edge bead removal	Use cleanroom swab dipped in acetone. Clean off excess acetone from swab with wipe before cleaning the wafer.
6	Soft bake on hotplate	1 minute @ 100 °C
7	Exposure	4.7 seconds @ 12 mW/cm^2 46.75 mJ/cm^2 total dose
8	Post exposure bake on hotplate	1 minute @ 100 °C
9	Photoresist development	1 minute w/ AZ 300 MIF Rinse with DI water and dry after development.
10	Descum in O_2 plasma	1 minute recipe in Matrix Asher

Figure A1.1: Lithography process developed for nLof 2020 on a bare silicon substrate. Typical minimum feature size of this process is 2 μm.

sidewall slope, which is harder to coat during thin film deposition. This leaves the photoresist easier to remove and the film pattern cleaner. An HMDS vapor coat is used before spinning on the photoresist to promote adhesion of the photoresist to the silicon surface.

A1.1.2 Lithium Niobate

The process given in Figure A1.2 is a lithography process for lift-off patterning on lithium niobate substrates. As lithium niobate is both piezoelectric and pyroelectric [228], care must be taken during any steps at elevated temperatures, such as photoresist baking. If temperature is changed too rapidly, thermal shock can cause the wafers to spark and/or shatter. During baking, it was found that lithium niobate wafers became charged and electrostatically bonded to the hotplates. Both issues were alleviated by placing the wafers on an aluminum block (6 inches × 6 inches × 1/4 inches) and transferring the entire block on and off the hot plate. If the wafers were still electrostatically bonded after cooling, they were carefully removed using a razor blade as a wedge. The aluminum block provides extra thermal mass and slows the rate of temperature change felt by the lithium niobate wafers, reducing the number of shattered wafers. It was found that higher yields were achieved with smaller diameter wafers.

#	Process Step	Notes
1	Wafer cleaning (Acetone, Methanol, IPA, DI water)	Avoid sonication if high aspect ratio features are on the wafer because they can be damaged.
2	Dehydration on hotplate	Place wafer on aluminum block and transfer the block to hot plate. 10 minutes @ 100 °C
3	Cool down	Remove block from hotplate but keep wafers on the block for the entire time. 5 minutes
4	HMDS vapor coat	10 minutes
5	Spin on AZ nLof 2020	Spray with nitrogen to clean off any debris. 500 RPM @ 500 RPM/s for 5 seconds (spread) 3000 RPM @ 500 RPM/s for 60 seconds (leveling)
6	Edge bead removal	Use cleanroom swab dipped in acetone. Clean off excess acetone from swab with wipe before cleaning the wafer.
7	Soft bake on hotplate	Place wafer on aluminum block and transfer the block to hot plate. 1 minute @ 110 °C
8	Cool down	Remove block from hotplate but keep wafers on the block for the entire time. 5 minutes
9	Exposure	7.7 seconds @ 8.5 mW/cm^2 65.45 mJ/cm^2 total dose
10	Post exposure bake on hotplate	Place wafer on aluminum block and transfer the block to hot plate. 1 minute @ 110 °C
11	Cool down	Remove block from hotplate but keep wafers on the block for the entire time. 5 minutes
12	Photoresist development	45 seconds w/ AZ 300 MIF Rinse with DI water after development.
13	Descum in O_2 plasma	30 seconds in Oxford FRIE using desum recipe

Figure A1.2: Lithography process developed for nLof 2020 on a bare lithium niobate substrate. Typical minimum feature size of this process is 2.5 μm.

A1.1.3 Aluminum Nitride / Silicon Nitride

Care must be exercised when performing photolithography on aluminum nitride surfaces. Because of the aluminum content of the film, many common photoresist developers will etch the aluminum nitride during development, such as those that contain TMAH [99] and KOH [229]. Positive tone photoresists using AZ Developer, and other similar developers, have been shown to be compatible with aluminum nitride. However, in developing the processes used in this work, it was found that negative tone photoresists using AZ Developer, specifically Ma-N 490 and AZ 5214E used in image reversal mode, occasionally left residue on the aluminum nitride surface that could not be removed.

The process shown in Figure A1.3 uses KMPR 1005. This is a negative tone resist with nearly vertical sidewalls and is capable to be spun on several micrometers thick. The photoresist thickness is key as it helps compensate for the lack of negative sidewall in the KMPR, making it an acceptable choice for lift-off processing. The process in Figure A1.3 uses SU-8 Developer to pattern the KMPR and has consistently been found to be safe to use with aluminum nitride. Acetone will cause KMPR 1005 to swell and crack but will not remove it. Using AZ 300T to remove the KMPR will attack the aluminum nitride due to the TMAH content. ALEG 380 is advertised as being aluminum safe, but in process development it was found that it can occasionally etch aluminum nitride films. It was consistently found that NMP heated to 80 °C would remove the KMPR without attacking the aluminum nitride. Because aluminum nitride was obtained through an external vendor, lithography testing was done on silicon substrates with a layer of silicon nitride with a thickness equal to the desired aluminum nitride thickness. Lithography recipes developed on silicon nitride were consistently found to have the same resolution when used on aluminum nitride, regardless of the resist.

#	Process Step	Notes
1	Wafer cleaning (Acetone, Methanol, IPA, DI water)	Avoid sonication if high aspect ratio features are on the wafer because they can be damaged.
2	Dehydration on hotplate	15 minutes @ 150 °C
3	Spin on KMPR 1005	Spray with nitrogen to clean off any debris. 500 RPM @ 100 RPM/s for 5 seconds (spread) 3000 RPM @ 1000 RPM/s for 30 seconds (leveling)
4	Edge bead removal	Use cleanroom swab dipped in acetone. Clean off excess acetone from swab with wipe before cleaning the wafer.
5	Soft bake on hotplate	5 minutes @ 100 °C
6	Exposure	7.7 seconds @ 12 mW/cm^2 92 mJ/cm^2 total dose
7	Post exposure bake on hotplate	2 minute @ 100 °C
8	Photoresist development	8 minutes w/ SU-8 Developer Heavy agitation is needed during development. It is recommended to do development in a beaker with a stirring bar. When pulling from the developer, it is recommended to spray the surface of the wafer with fresh developer to clean off stubborn debris. After spraying with fresh developer, it is recommended to spray the surface of the wafer with IPA. Any areas that turn white are underdeveloped. Refer to KMPR 10005 datasheet for exact details on the above procedure. Rinse with DI water and dry after development.
9	Descum in O_2 plasma	1 minute recipe in Matrix Asher

Figure A1.3: Lithography process developed for KMPR 1005 on 400 nm of aluminum nitride (or silicon nitride) on a silicon substrate. Typical minimum feature size of this process is 2 μm.

A1.1.4 Mask Layout

During process development, several elements of the mask layout were found to be greatly helpful in device processing (Figure A1.4).

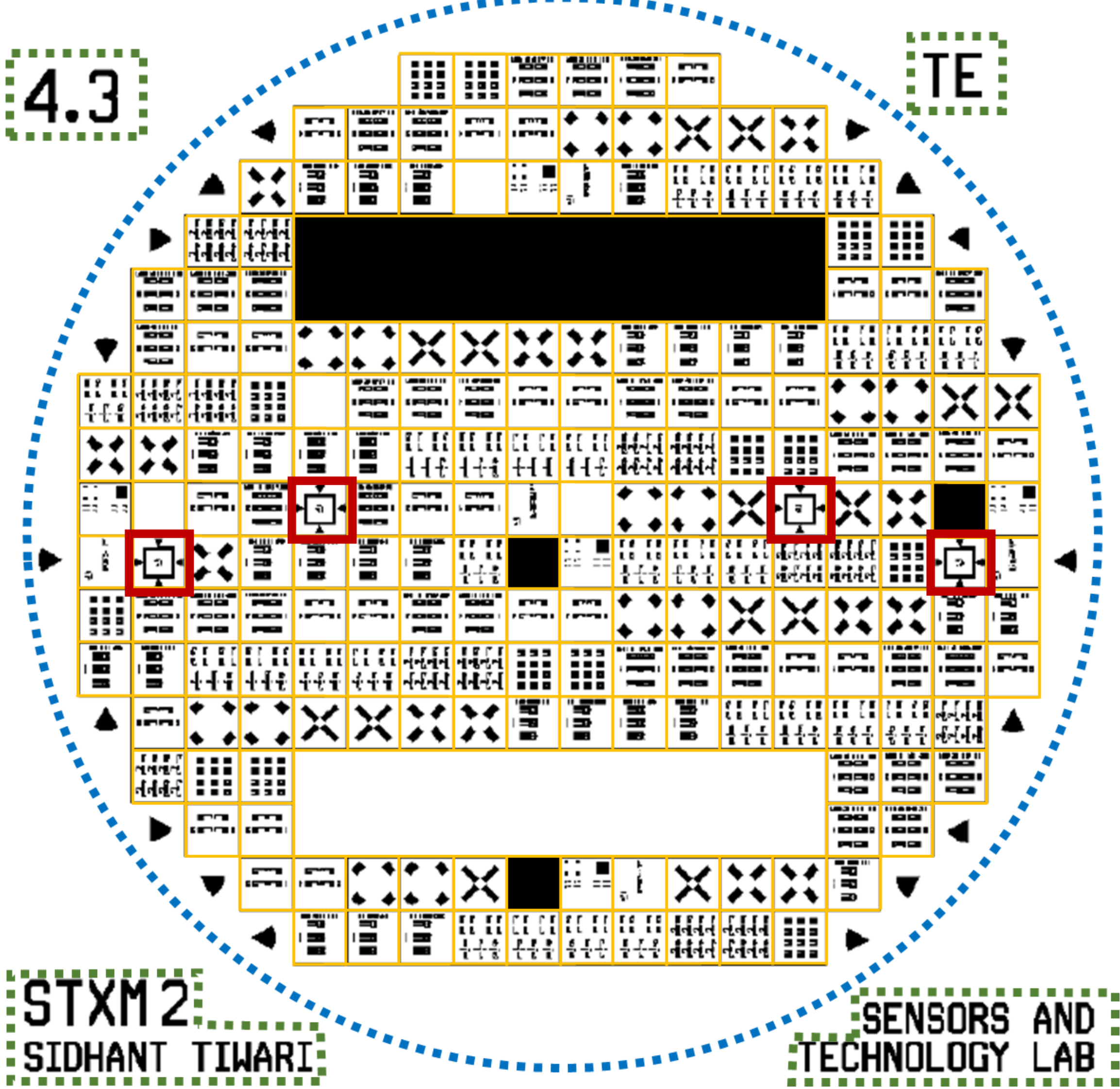

Figure A1.4: Sample lithography mask. Grid lines are highlighted in yellow. Alignment verniers are highlighted in red. The blue dotted circle shows where a 4-inch wafer would sit once aligned to the mask. Green dotted boxes highlight identifying text for the mask.

1. Continuous sheets of material were found to take much longer lift-off. To speed this process up, it is helpful to break up continuous sheets by introducing a grid pattern. This pattern doubles as a guide for wafer dicing after device fabrication is complete. It is not advised to make a grid pattern for any magnetic layers, as characterization of any magnetic patterns on the die will also include measurements of the magnetic material left on the grid after dicing.

2. It is not recommended to place any devices 5 to 10 mm from the edge of the wafer because these areas will often be damaged during device processing, either by equipment or by manual handling.
3. To assist in finding the alignment verniers, it is recommended to place arrows along the periphery of the wafer.
4. It is recommended to have back up alignment verniers in case the originals are damaged during processing.
5. Large text in the corners is not only helpful for mask organization but helps keep track of the mask orientation when setting up the contact aligner, as it can be difficult to tell if the mask is properly oriented under the microscope.
6. It is recommended to label each die with its (x,y) coordinates in the grid. During fabrication, these labels will make it easy to label zones of the wafer that have been damaged during processing. Post dicing these coordinates will act as unique labels to keep the dies organized.

A1.2 Thin Film Deposition

A1.2.1 Electron-Beam Evaporation

Electron-beam evaporation is recommended when possible when using lift-off processes. This deposition method is not very conformal, meaning photoresist sidewalls will be minimally coated, the photoresist can be easily removed, and the film patterns will be clean. It is recommended to only use this process for thinner films, as films greater than approximately 300 nm have shown poor adhesion during the process development for this work. Care must be exercised when depositing films that required high electron-beam powers or slow deposition

rates, such as platinum, as the wafers are known to heat up during deposition. For lift-off processes, excessive heat during deposition could hard bake the photoresist on the wafer, making it nearly impossible to remove.

A1.2.2 Sputtering

Because of the use of plasmas instead of electron-beams, material deposited by sputtering has higher energy upon impact with the wafer surface than evaporated films, leading to better adhesion of thin films to the wafer. This, combined with the faster deposition rate, makes sputtering more advantageous than evaporation for thicker films. In process development, it was found that the upper limit of film thickness to retain good adhesion is approximately 1 μm. Scattering by the plasma (resulting in a less directional trajectory) and higher energy (resulting in higher surface mobility) of the sputtered material means that sputtering is a more conformal process, making it more difficult for lift-off. Sputtering can also simultaneously deposit multiple materials at once, making it useful for deposition of compound thin films [104], [230]. Multiple targets are often needed when depositing compounds because different elements will have different sputtering yields, which makes it difficult to control material composition while using a single target.

Controlling the plasma pressure and power during sputtering gives control of the film microstructure. Deposition processes that produce more porous films (relative to the natural crystal structure) will leave the films with tensile residual stresses. Processes that produce more compact films will lead to films with compressive stresses. Tuning of the process pressure and power during deposition will alter the microstructure and control the residual stresses present in the film (Figure A1.5) [231]. During the process development for this work, it was found that plasma pressure seemed to have more control over the residual film stress and power seemed to have more control over the deposition rate. Metals deposited by DC sputtering were

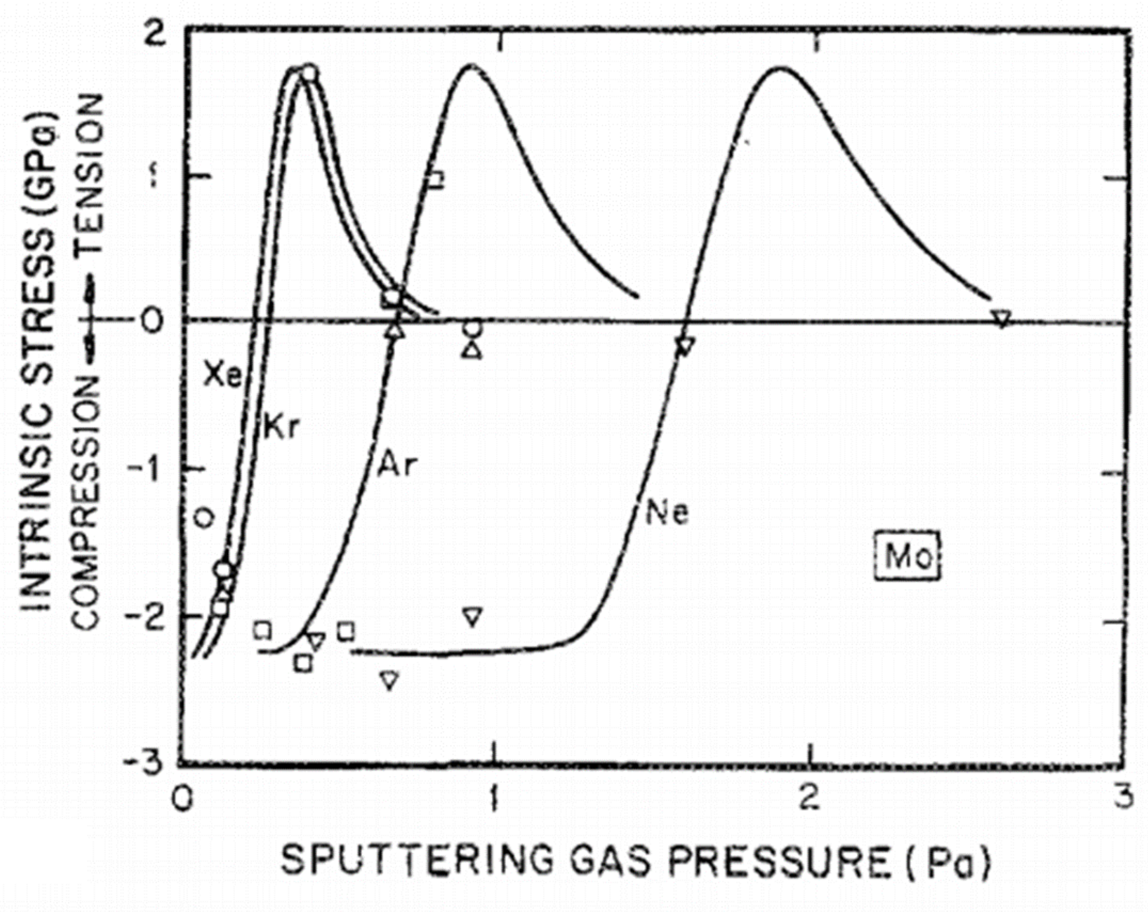

Figure A1.5: Relation between plasma pressure and residual film stress for 100 nm of sputtered molybdenum. Each curve is for a different type of plasma. Figure from [231].

found to have the largest amount of tunability of the residual stress. Deposition of aluminum oxide by RF sputtering was found to have very little tunability and were consistently found to have large compressive stresses. Lower plasma pressure can also help reduce the conformality of the sputter deposition, by reducing the collisions of the sputtered material with the plasma to make the deposition more directional. This is very helpful for lift-off processing as it helps minimize coating of the photoresist sidewalls, as shown in Figure A1.6.

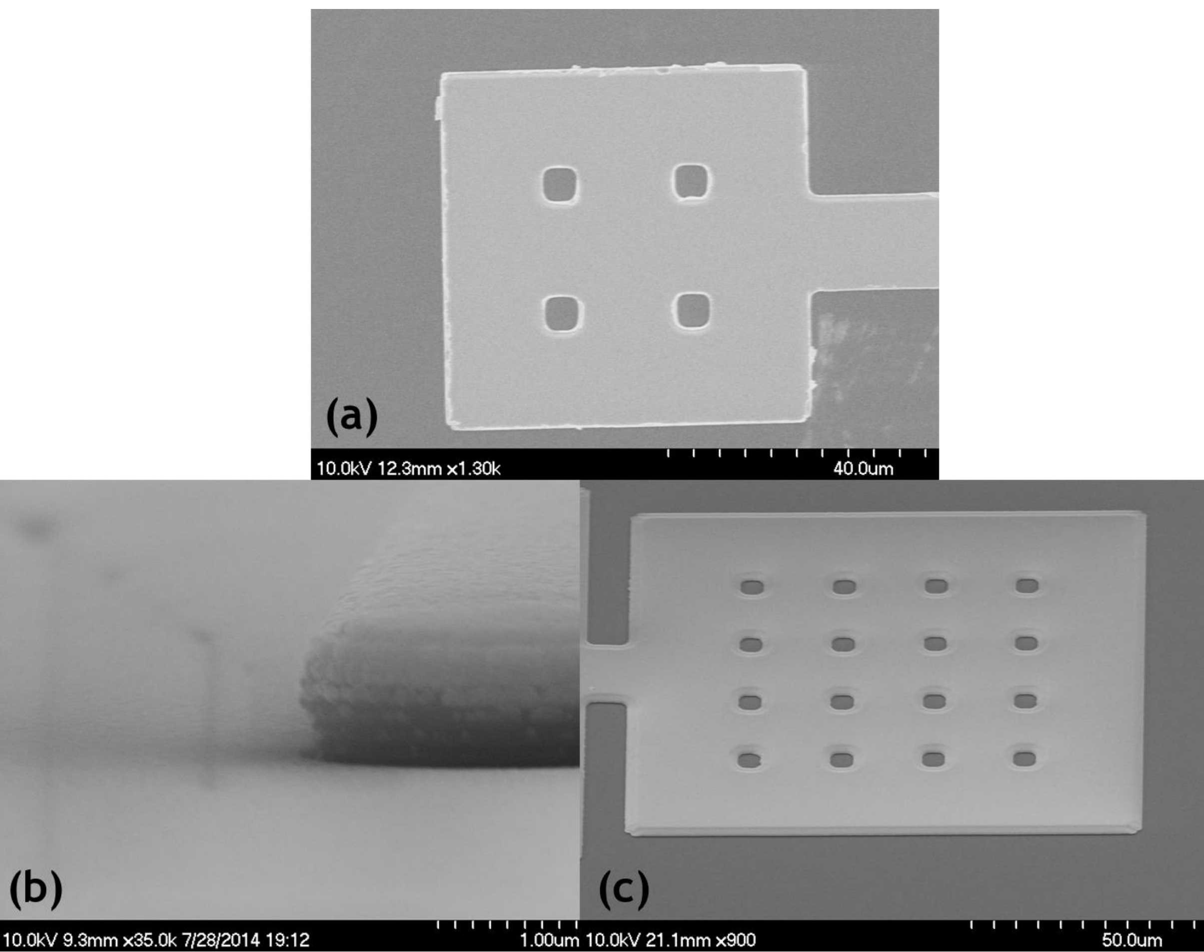

Figure A1.6: (a) Lift-off results for sputtered nickel film with a conformal deposition. The jagged edges are "winging" due to the coating of the photoresist sidewall. (b) Photoresist sputter coated by nickel with a low-pressure sputtering process. Notice how the negative sidewall is not as heavily coated by metal, as shown by its darker color in the image. (c) Lift-off results for nickel using a low-pressure sputtering process. Notice the absence of any winging. Because of the long mean free path of the sputtered material, there is shadowing by the photoresist during deposition. This manifests itself as thinner regions at the pattern edges in the image.

A1.2.3 Adhesion Layers for Metallization

Adhesion of metals to substrates can be very poor. It is recommended to use 2 to 10 nm of some type of reactive metal before the deposition of the desired material (without breaking vacuum between depositions) to bond the desired material to the substrate. Throughout this work, titanium has been the adhesion layer of choice. Underlayers can influence material

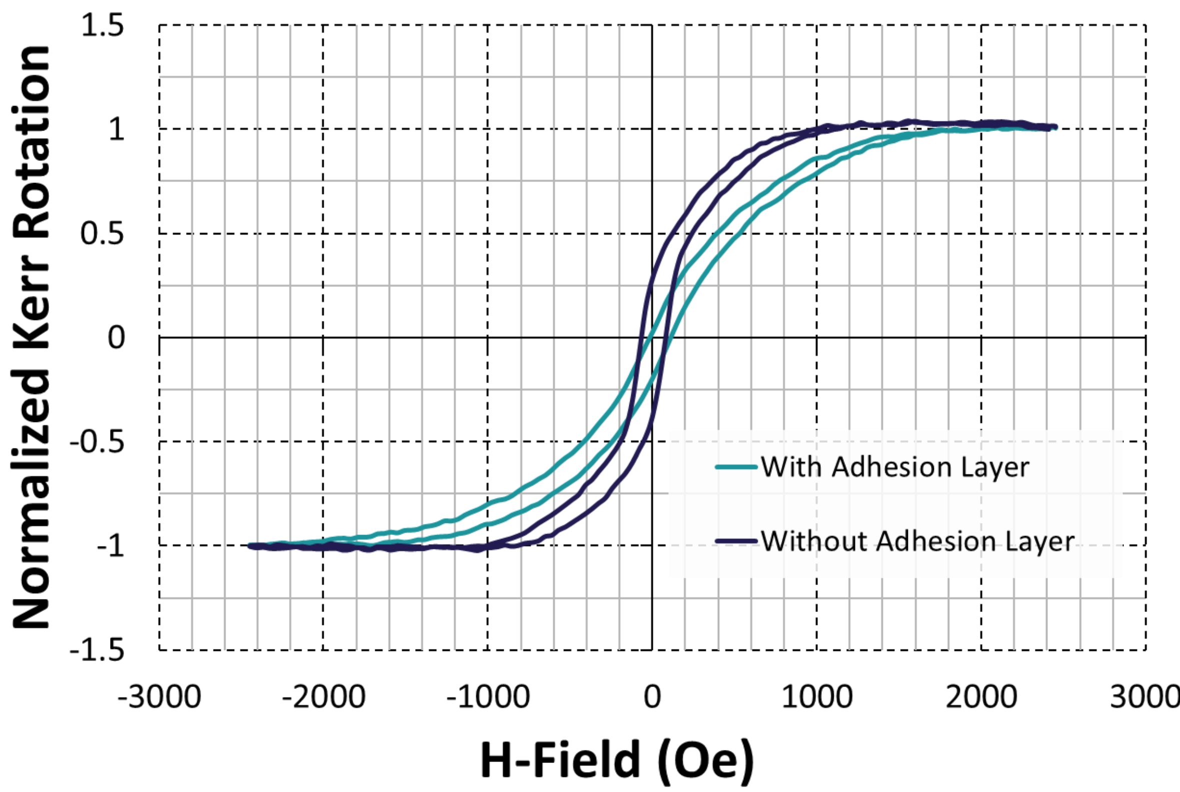

Figure A1.7: Measured magneto-optic Kerr effect (MOKE) response from a nickel thin film deposited with and without a titanium adhesion layer.

structure and properties (Figure A1.7), so it is recommended that all material characterization be done with the exact underlayers to be used in the device, including adhesion layers.

A1.2.4 Reactive Sputtering of Aluminum Nitride

Aluminum nitride thin film is deposited via reactive sputtering, using an aluminum sputtering target and nitrogen gas inside the sputtering chamber. Piezoelectricity requires a lack of inversion symmetry in the crystal structure [33], meaning that control of the crystallinity is key for the growth of quality film. Aluminum nitride has a hexagonal crystal structure and quality polycrystalline films must be grown such that the c-axis of each crystal grain is aligned to maximize the piezoelectric coupling [63], [83]. To characterize these oriented polycrystalline materials, XRD rocking curves are used to measure the angular spread in c-axis.

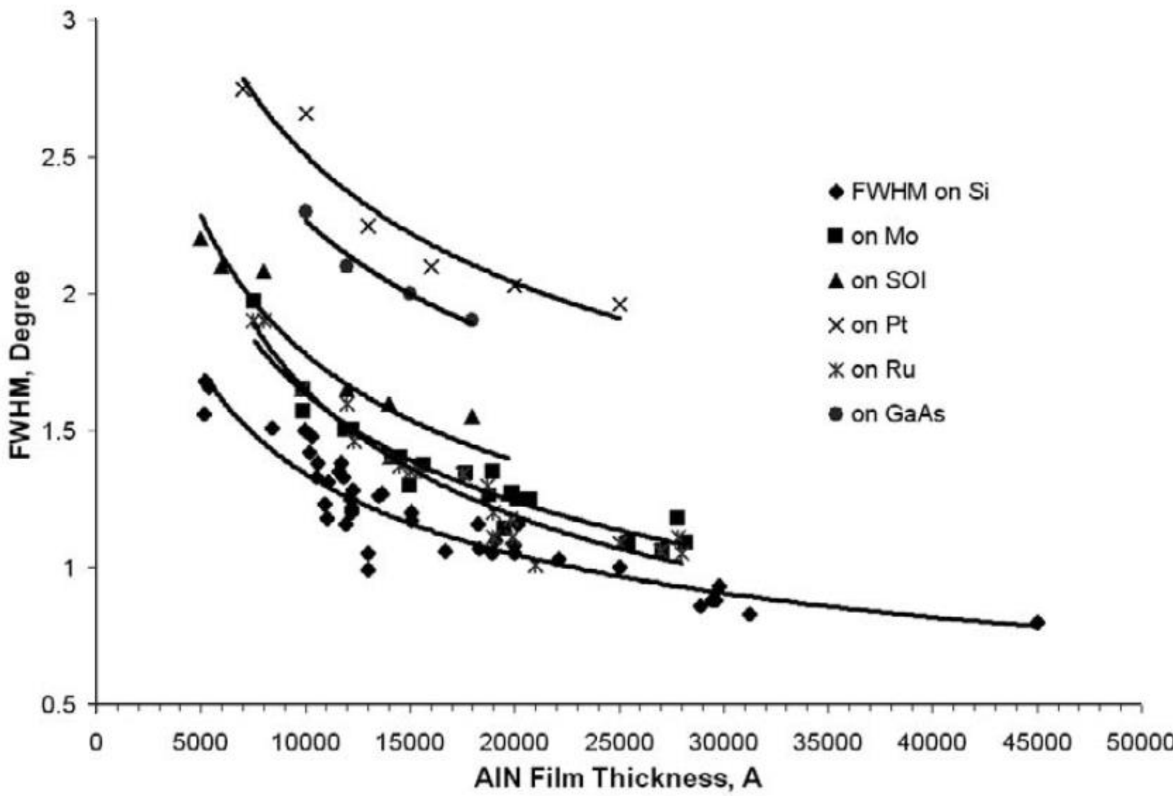

Figure A1.8: Measured c-axis angular spread in aluminum nitride as a function of film thickness and underlayer. Figure from [63].

A proper underlayer must be chosen to promote oriented aluminum nitride growth, with platinum and molybdenum being common choices (Figure A1.8) [63]. The c-axis will typically grow orthogonal to the wafer surface, but tilted aluminum nitride can be grown by changing the angle of incidence of the sputtered material [232], [233]. Tilted aluminum nitride is necessary to achieve thickness shear modes using parallel plate electrodes. Very thin films of aluminum nitride may demonstrate poor quality as the first few layers of growth may contain inverted domains [234].

A1.3 Etching

A1.3.1 Wet Etching of Aluminum Nitride

Chemicals that etch aluminum can be used to etch aluminum nitride, such as TMAH [99], KOH [229], and phosphoric acid [96]. Wet etching is useful for via patterning as it creates a slight slope in the aluminum nitride profile (Figure A1.9), meaning that evaporated films can be used to make contact to exposed metal layers despite the nonconformality of the deposition [96].

In this work, AZ 300 MIF (a TMAH based photoresist developer) is used to wet etch vias. To clear 400 nm of material, it was found to take between 10 and 20 minutes. During the etch, the wafer is removed from the photoresist developer and rinsed with DI water approximately every 2 minutes to check on the progress of the etch. Anecdotally, it was observed that the etch seemed to slow down if the intervals between checks were too long. Developed KMPR 1005 was found to have minimal erosion by AZ 300 MIF, making it an adequate etch mask. The etch rate of the aluminum nitride drastically slows once the etch reaches the inversion domains in the first few layers [234]. The rate of etching for the last few layers can vary from wafer to wafer as it depends on the density of the inversion domains. This is important when designing

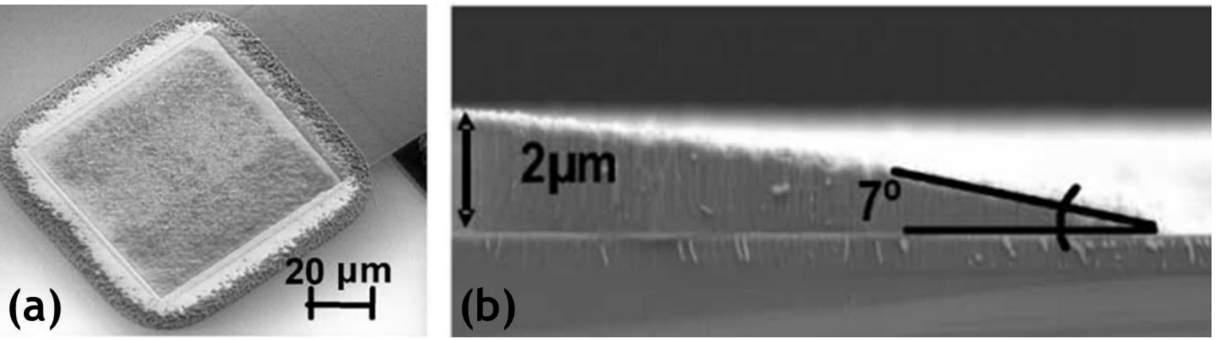

Figure A1.9: (a) Via etched in aluminum nitride with hot phosphoric acid. The spotty surface of the via is indicative of inversion domains. (b) Sidewall slope of wet etched via. Adapted from [96].

devices because the lateral etching of the aluminum nitride will continue at the same rate while the vertical etching slows down dramatically. The etch rate of the inversion domains have also been seen to vary depending on whether the via is over platinum or silicon. Circles are recommended for the via geometries as the lateral etch rate is uniform. In squares and rectangles, the corners were found to etch slower than the sides.

A1.3.2 Plasma Etching of Aluminum Nitride

To etch aluminum nitride, it is recommended to use chlorine-based plasmas. The chlorine chemically etches the aluminum in the film while the nitrogen is removed via physical bombardment by the plasma [98]. This is recommended over fluorine-based plasmas, which produces a nonvolatile byproduct of the reaction between aluminum and fluorine [235], [236], limiting the speed of the etch. In development of the processes used in this work, it was found that chlorine plasmas etch aluminum nitride approximately 5 to 10 times faster than fluorine plasmas. The slow etching rate of fluorine can be taken advantage to pattern films on top of the aluminum nitride, as any damage from slight over etch will be minimal.

A1.3.3 Gas Phase Etching of Silicon

In this work, release of the MEMS structures from the substrate was done with isotropic gas phase etching using XeF_2 [237]. This etch process has high selectivity to silicon but has been found to still etch several other materials by a nonnegligible degree [238], [239]. As the XeF_2 can form HF vapor in the presence of moisture, it is paramount to make sure samples are thoroughly dehydrated before proceeding with the etch. This will help preserve the high selectivity of the XeF_2, as any HF vapor present in the chamber will also attack the sample. The etch rate is heavily dependent on geometry, with larger areas being slower to etch. As a result, as the etch proceeds, the etch rate will slow down as the exposed silicon surface area increases. While isotropic, the etch is not even and the silicon is left visibly roughened by the etch. The

etch rate is the most consistent if the XeF_2 is regularly replenished, so XeF_2 is pulsed throughout the step. In the processes used in this work, the pulse duration is always 1 minute and the XeF_2 pressure is always set to 2500 mTorr. The total number of pulses is determined separately for each design. XeF_2 has been found to attack other metals, such as FeGaB and titanium, so an aluminum capping layer is recommended when appropriate [240]. On occasion, gold was seen to discolor after exposure to XeF_2 but had no noticeable etching.

References

[1] W. Eerenstein, N. D. Mathur, and J. F. Scott, “Multiferroic and magnetoelectric materials,” *Nature*, vol. 442, no. 7104, pp. 759–765, Aug. 2006, doi: 10.1038/nature05023.

[2] R. Ramesh and N. A. Spaldin, “Multiferroics: progress and prospects in thin films,” *Nat. Mater.*, vol. 6, no. 1, pp. 21–29, Jan. 2007, doi: 10.1038/nmat1805.

[3] C. W. Nan, M. I. Bichurin, S. Dong, D. Viehland, and G. Srinivasan, “Multiferroic magnetoelectric composites: Historical perspective, status, and future directions,” *J. Appl. Phys.*, vol. 103, no. 3, p. 031101, Feb. 2008, doi: 10.1063/1.2836410.

[4] G. Lawes and G. Srinivasan, “Introduction to magnetoelectric coupling and multiferroic films,” *J. Phys. D. Appl. Phys.*, vol. 44, p. 243001, 2011, doi: 10.1088/0022-3727/44/24/243001.

[5] G. P. Carman and N. Sun, “Strain-mediated magnetoelectrics: Turning science fiction into reality,” *MRS Bull.*, vol. 43, no. 11, pp. 822–828, Nov. 2018, doi: 10.1557/mrs.2018.236.

[6] N. A. Spaldin and R. Ramesh, “Advances in magnetoelectric multiferroics,” *Nat. Mater.*, vol. 18, no. 3, pp. 203–212, Mar. 2019, doi: 10.1038/s41563-018-0275-2.

[7] M. Fiebig, T. Lottermoser, D. Meier, and M. Trassin, “The evolution of multiferroics,” *Nat. Rev. Mater.*, vol. 1, no. 8, pp. 1–14, Jul. 2016, doi: 10.1038/natrevmats.2016.46.

[8] N. A. Spaldin and M. Fiebig, “The renaissance of magnetoelectric multiferroics,” *Science (80-.).*, vol. 309, no. 5733, pp. 391–392, 2005, doi: 10.1126/science.1113357.

[9] N. A. Hill, “Why are there so few magnetic ferroelectrics?,” *J. Phys. Chem. B*, vol. 104, no. 29, pp. 6694–6709, Jul. 2000, doi: 10.1021/jp000114x.

[10] J. Xu *et al.*, “A Low Frequency Mechanical Transmitter Based on Magnetoelectric Heterostructures Operated at Their Resonance Frequency,” *Sensors*, vol. 19, no. 4, p. 853, Feb. 2019, doi: 10.3390/s19040853.

[11] T. Nan *et al.*, “Acoustically actuated ultra-compact NEMS magnetoelectric antennas,” *Nat. Commun.*, vol. 8, no. 1, pp. 1–7, 2017, doi: 10.1038/s41467-017-00343-8.

[12] J. D. Schneider *et al.*, “Experimental demonstration and operating principles of a multiferroic antenna,” *J. Appl. Phys.*, vol. 126, no. 22, p. 224104, Dec. 2019, doi: 10.1063/1.5126047.

[13] Y. Zhang, Z. Li, C. Deng, J. Ma, Y. Lin, and C. W. Nan, “Demonstration of magnetoelectric read head of multiferroic heterostructures,” *Appl. Phys. Lett.*, vol. 92, no. 15, p. 152510, Apr. 2008, doi: 10.1063/1.2912032.

[14] T. Wu *et al.*, “Electrical control of reversible and permanent magnetization reorientation for magnetoelectric memory devices,” *Appl. Phys. Lett.*, vol. 98, no. 26, p. 262504, Jun. 2011, doi: 10.1063/1.3605571.

[15] N. D’Souza, M. Salehi Fashami, S. Bandyopadhyay, and J. Atulasimha, “Experimental Clocking of Nanomagnets with Strain for Ultralow Power Boolean Logic,” *Nano Lett.*, vol. 16, no. 2, pp. 1069–

1075, Feb. 2016, doi: 10.1021/acs.nanolett.5b04205.

[16] C. Zhou, C. Zhang, J. Yao, and C. Jiang, “Lateral electric-field-driven non-volatile four-state memory in multiferroic heterostructures,” *Appl. Phys. Lett.*, vol. 109, no. 11, p. 112404, Sep. 2016, doi: 10.1063/1.4962813.

[17] M. Kadota, S. Ito, Y. Ito, T. Hada, and K. Okaguchi, “Magnetic sensor based on surface acoustic wave resonators,” *Jpn. J. Appl. Phys.*, vol. 50, no. 7 PART 2, p. 07HD07, Jul. 2011, doi: 10.1143/JJAP.50.07HD07.

[18] W. Li, P. Dhagat, and A. Jander, “Surface acoustic wave magnetic sensor using galfenol thin film,” *IEEE Trans. Magn.*, vol. 48, no. 11, pp. 4100–4102, 2012, doi: 10.1109/TMAG.2012.2201928.

[19] T. Nan, Y. Hui, M. Rinaldi, and N. X. Sun, “Self-biased 215MHz magnetoelectric NEMS resonator for ultra-sensitive DC magnetic field detection,” *Sci. Rep.*, vol. 3, pp. 1–6, 2013, doi: 10.1038/srep01985.

[20] Z. Xiao *et al.*, “Cytocompatible magnetostrictive microstructures for nano- and microparticle manipulation on linear strain response piezoelectrics,” *Multifunct. Mater.*, vol. 1, no. 1, p. 014004, Nov. 2018, doi: 10.1088/2399-7532/AAE4D7.

[21] Y. C. Hsiao *et al.*, “Capturing magnetic bead-based arrays using perpendicular magnetic anisotropy,” *Appl. Phys. Lett.*, vol. 115, no. 8, p. 082402, Aug. 2019, doi: 10.1063/1.5085354.

[22] H. Sohn *et al.*, “Electrically driven magnetic domain wall rotation in multiferroic heterostructures to manipulate suspended on-chip magnetic particles,” *ACS Nano*, vol. 9, no. 5, pp. 4814–4826, May 2015, doi: 10.1021/nn5056332.

[23] J. P. Domann, C. Chen, A. E. Sepulveda, R. N. Candler, and G. P. Carman, “Multiferroic Micro-Motors with Deterministic Single Input Control,” Feb. 2018, Accessed: May 03, 2020. [Online]. Available: http://arxiv.org/abs/1802.09420.

[24] P. Smole *et al.*, “Magnetically tunable SAW-resonator,” in *Proceedings of the Annual IEEE International Frequency Control Symposium*, 2003, pp. 903–906, doi: 10.1109/freq.2003.1275210.

[25] H. Lin *et al.*, “Tunable RF band-pass filters based on NEMS magnetoelectric resonators,” in *IEEE MTT-S International Microwave Symposium Digest*, Aug. 2016, vol. 2016-August, doi: 10.1109/MWSYM.2016.7540335.

[26] A. K. Ganguly, K. L. Davis, D. C. Webb, C. Vittoria, and D. W. Forester, “Magnetically tuned surface-acoustic-wave phase shifter,” *Electron. Lett.*, vol. 11, pp. 610–611, Dec. 1975, doi: 10.1049/el:19750465.

[27] R. F. Wiegert and M. Levy, “Magnetic field dependence of surface acoustic wave velocity and attenuation in nickel thin films,” *J. Appl. Phys.*, vol. 64, no. 10, pp. 5411–5413, Nov. 1988, doi: 10.1063/1.342386.

[28] D. C. Webb, D. W. Forester, A. K. Ganguly, and C. Vittoria, “Applications of amorphous magnetic-layers in surface-acoustic-wave devices,” *IEEE Trans. Magn.*, vol. 15, no. 6, pp. 1410–1415, 1979, doi: 10.1109/TMAG.1979.1060442.

[29] A. K. Zvezdin and A. P. Pyatakov, “Phase transitions and the giant magnetoelectric effect in multiferroics,” *Physics-Uspekhi*, vol. 47, no. 4, pp. 416–421, Apr. 2004, doi: 10.1070/pu2004v047n04abeh001752.

[30] J. van den Brink and D. I. Khomskii, “Multiferroicity due to charge ordering,” *J. Phys. Condens. Matter*, vol. 20, p. 434217, 2008, doi: 10.1088/0953-8984/20/43/434217.

[31] G. Catalan and J. F. Scott, “Physics and Applications of Bismuth Ferrite,” *Adv. Mater.*, vol. 21, no. 24, pp. 2463–2485, Jun. 2009, doi: 10.1002/adma.200802849.

[32] J. Wang *et al.*, "Epitaxial BiFeO3 multiferroic thin film heterostructures," *Science (80-.).*, vol. 299, no. 5613, pp. 1719–1722, Mar. 2003, doi: 10.1126/science.1080615.

[33] Robert E. Newnham, *Properties of materials: anisotropy, symmetry, structure*. Oxford University Press on Demand, 2005.

[34] D. Boldrin *et al.*, "Giant Piezomagnetism in Mn3NiN," *ACS Appl. Mater. Interfaces*, vol. 10, no. 22, pp. 18863–18868, Jun. 2018, doi: 10.1021/acsami.8b03112.

[35] A. S. Borovik-Romanov, "PIEZOMAGNETISM IN THE ANTIFERROMAGNETIC FLUORIDES OF COBALT AND MANGANESE," *J. Exptl. Theor. Phys.*, vol. 11, no. 4, pp. 1088–1098, 1960.

[36] A. E. Clark, J. P. Teter, and M. Wun-Fogle, "Characterization of Terfenol-D for magnetostrictive transducers," *J. Acoust. Soc. Am.*, vol. 89, no. 3, pp. 1448–1455, Mar. 1991, doi: 10.1121/1.400678.

[37] E. du Tremolet de Lacheisseries, *Magnetostriction: Theory and Applications of Magnetoelasticity*. CRC Press, 1993.

[38] J. Domann, T. Wu, T. K. Chung, and G. Carman, "Strain-mediated magnetoelectric storage, transmission, and processing: Putting the squeeze on data," *MRS Bull.*, vol. 43, no. 11, pp. 848–853, Nov. 2018, doi: 10.1557/mrs.2018.260.

[39] M. T. Bohr and I. A. Young, "CMOS Scaling Trends and beyond," *IEEE Micro*, vol. 37, no. 6, pp. 20–29, Nov. 2017, doi: 10.1109/MM.2017.4241347.

[40] Z. Xiao *et al.*, "Tunable Magnetoelastic Effects in Voltage-Controlled Exchange-Coupled Composite Multiferroic Microstructures," *ACS Appl. Mater. Interfaces*, vol. 12, no. 5, pp. 6752–6760, Feb. 2020, doi: 10.1021/acsami.9b20876.

[41] V. G. Harris, "Modern microwave ferrites," *IEEE Trans. Magn.*, vol. 48, no. 3, pp. 1075–1104, 2012, doi: 10.1109/TMAG.2011.2180732.

[42] J. D. Adam, L. E. Davis, G. F. Dionne, E. F. Schloemann, and S. N. Stitzer, "Ferrite devices and materials," *IEEE Trans. Microw. Theory Tech.*, vol. 50, no. 3, pp. 721–737, Mar. 2002, doi: 10.1109/22.989957.

[43] W. Palmer, D. Kirkwood, S. Gross, M. Steer, H. S. Newman, and S. Johnson, "A Bright Future for Integrated Magnetics: Magnetic Components Used in Microwave and mm-Wave Systems, Useful Materials, and Unique Functionalities," *IEEE Microw. Mag.*, vol. 20, no. 6, pp. 36–50, Jun. 2019, doi: 10.1109/MMM.2019.2904381.

[44] H. Sobol and K. Tomiyasu, "Milestones of microwaves," *IEEE Trans. Microw. Theory Tech.*, vol. 50, no. 3, pp. 594–611, Mar. 2002, doi: 10.1109/22.989945.

[45] V. Korenivski, "GHz magnetic film inductors," *J. Magn. Magn. Mater.*, vol. 215, pp. 800–806, Jun. 2000, doi: 10.1016/S0304-8853(00)00292-4.

[46] H. J. Kim, Y. J. Kim, and J. R. Kim, "An Integrated LTCC Inductor Embedding NiZn Ferrite," *IEEE Trans. Magn.*, vol. 42, no. 10, pp. 2840–2842, 2006, doi: 10.1109/TMAG.2006.879741.

[47] S. C. Tang, S. Y. R. Hui, and H. S. H. Chung, "Evaluation of the shielding effects on printed-circuit-board transformers using ferrite plates and copper sheets," *IEEE Trans. Power Electron.*, vol. 17, no. 6, pp. 1080–1088, Nov. 2002, doi: 10.1109/TPEL.2002.805585.

[48] S. C. Tang, S. Y. Ron Hui, and H. S. H. Chung, "A low-profile power converter using printed-circuit board (PCB) power transformer with ferrite polymer composite," *IEEE Trans. Power Electron.*, vol. 16, no. 4, pp. 493–498, Jul. 2001, doi: 10.1109/63.931055.

[49] J. Y. Park, L. K. Lagorce, and M. G. Allen, "Ferrite-based integrated planar inductors and transformers fabricated at low temperature," *IEEE Trans. Magn.*, vol. 33, no. 5 PART 1, pp. 3322–

3324, 1997, doi: 10.1109/20.617931.

[50] W. Pachler *et al.*, “A silver inkjet printed ferrite NFC antenna,” in *2014 Loughborough Antennas and Propagation Conference, LAPC 2014*, Dec. 2014, pp. 95–99, doi: 10.1109/LAPC.2014.6996329.

[51] J. Lee *et al.*, “Role of small permeability in gigahertz ferrite antenna performance,” *IEEE Magn. Lett.*, vol. 4, 2013, doi: 10.1109/LMAG.2012.2237163.

[52] D. M. Pozar, *Microwave engineering*, 4th ed. Hoboken, NJ: Wiley, 2012.

[53] J. D. Adam, “Mitigate the interference: Nonlinear frequency selective ferrite devices,” *IEEE Microw. Mag.*, vol. 15, no. 6, pp. 45–56, Sep. 2014, doi: 10.1109/MMM.2014.2332831.

[54] S. D. Bader and S. S. P. Parkin, “Spintronics,” *Annu. Rev. Condens. Matter Phys.*, vol. 1, no. 1, pp. 71–88, Aug. 2010, doi: 10.1146/annurev-conmatphys-070909-104123.

[55] V. K. Joshi, “Spintronics: A contemporary review of emerging electronics devices,” *Eng. Sci. Technol. an Int. J.*, vol. 19, no. 3, pp. 1503–1513, Sep. 2016, doi: 10.1016/j.jestch.2016.05.002.

[56] T. H. Lee, *The design of CMOS radio-frequency integrated circuits*. Cambridge University Press, 2003.

[57] Y. Yu *et al.*, “Magnetic-free radio frequency circulator based on spatiotemporal commutation of MEMS resonators,” in *Proceedings of the IEEE International Conference on Micro Electro Mechanical Systems (MEMS)*, Jan. 2018, vol. 2018-Janua, pp. 154–157, doi: 10.1109/MEMSYS.2018.8346507.

[58] J. Krol and S. Gong, “A non-magnetic gyrator utilizing switched delay lines,” in *European Microwave Week 2017: “A Prime Year for a Prime Event”, EuMW 2017 - Conference Proceedings; 47th European Microwave Conference, EuMC 2017*, Dec. 2017, vol. 2017-January, pp. 452–455, doi: 10.23919/EuMC.2017.8230887.

[59] M. M. Torunbalci, T. J. Odelberg, S. Sridaran, R. C. Ruby, and S. A. Bhave, “An FBAR Circulator,” *IEEE Microw. Wirel. Components Lett.*, vol. 28, no. 5, pp. 395–397, May 2018, doi: 10.1109/LMWC.2018.2815271.

[60] Q. Wu, X. Zou, R. Zhu, and Y. E. Wang, “Chip-Scale RF Correlator with Monolithically Integrated Time-Varying Transmission Line (TVTL),” in *IEEE MTT-S International Microwave Symposium Digest*, Aug. 2018, vol. 2018-June, pp. 431–434, doi: 10.1109/MWSYM.2018.8439846.

[61] J. Marašević, J. Zhou, H. Krishnaswamy, Y. Zhong, and G. Zussman, “Resource Allocation and Rate Gains in Practical Full-Duplex Systems,” in *IEEE/ACM Transactions on Networking*, Feb. 2017, vol. 25, no. 1, pp. 292–305, doi: 10.1109/TNET.2016.2575016.

[62] R. A. Johnson, *Mechanical Filters in Electronics*. John Wiley & Sons, Inc., 1983.

[63] K. Hashimoto, *RF bulk acoustic wave filters for communications*. Artech House, 2009.

[64] J. H. Collins, “A Short History of Microwave Acoustics,” *IEEE Trans. Microw. Theory Tech.*, vol. 32, no. 9, pp. 1127–1140, 1984, doi: 10.1109/TMTT.1984.1132824.

[65] A. B. Smith and R. W. Damon, “A Bibliography of Microwave Ultrasonics,” *IEEE Trans. Sonics Ultrason.*, vol. 17, no. 2, pp. 86–111, Feb. 2016, doi: 10.1109/tsu.1970.7404097.

[66] J. D. Adam, J. H. Collins, and J. M. Owens, “Microwave device applications of epitaxial magnetic garnets,” *Radio Electron. Eng.*, vol. 45, no. 12, pp. 738–748, 1975, doi: 10.1049/ree.1975.0144.

[67] F. R. Morgenthaler, “An Overview of Electromagnetic and Spin Angular Momentum Mechanical Waves in Ferrite Media,” *Proc. IEEE*, vol. 76, no. 2, pp. 138–150, 1988, doi: 10.1109/5.4390.

[68] W. Strauss, “Elastic and Magnetoelastic Waves in Yttrium Iron Garnet,” *Proc. IEEE*, vol. 53, no.

10, pp. 1485–1495, 1965, doi: 10.1109/PROC.1965.4261.

[69] B. A. Auld, J. H. Collins, and D. C. Webb, “Excitation of magnetoelastic waves in YIG delay lines,” *J. Appl. Phys.*, vol. 39, no. 3, pp. 1598–1602, Feb. 1968, doi: 10.1063/1.1656401.

[70] M. S. Sodha and N. C. Srivastava, *Microwave Propagation in Ferrimagnetics*. New York: Springer, 1981.

[71] A. G. Gurevich and G. A. Melkov, *Magnetization Oscillations and Waves*. CRC press, 1996.

[72] J. H. Collins, N. Rubino, D. A. Wilson, and H. R. Zapp, “Measurements of magneto-elastic constants by microwave techniques,” *Int. J. Electron.*, vol. 24, no. 5, pp. 453–474, 1968, doi: 10.1080/00207216808938041.

[73] J. H. Collins and H. R. Zapp, “Analysis of Two-Port Magnetoelastic Delay Lines as Pulse-Compression Filters,” in *Proceedings of the IEEE*, 1968, vol. 56, no. 3, pp. 273–285, doi: 10.1109/PROC.1968.6271.

[74] M. Borgeaud and F. R. Morgenthaler, “An improved two-port magnetoelastic delay line,” *IEEE Trans. Magn.*, vol. 21, no. 2, pp. 1156–1163, 1985, doi: 10.1109/TMAG.1985.1063662.

[75] E. Schlömann, R. I. Joseph, and T. Kohane, “Generation of Spin Waves in Nonuniform Magnetic Fields, with Application to Magnetic Delay Lines,” in *Proceedings of the IEEE*, 1965, vol. 53, no. 10, pp. 1495–1507, doi: 10.1109/PROC.1965.4262.

[76] H. Dötsch, “Magnetoelastic YIG delay lines with linear dispersion,” *J. Appl. Phys.*, vol. 43, no. 4, pp. 1923–1927, Apr. 1972, doi: 10.1063/1.1661417.

[77] B. F. Feldman, “Optimization of microwave magnetoelastic delay lines,” AIR FORCE INST OF TECH WRIGHT-PATTERSON AFB OH, 1988.

[78] J. H. Collins and B. Yazgan, “Influence of magnetostatic-field profiles on magnetoelastic wavepaths,” *Electron. Lett.*, vol. 2, no. 8, pp. 322–323, 1966, doi: 10.1049/el:19660271.

[79] “IEEE Standard on Piezoelectricity,” *ANSI/IEEE Std 176-1987*, pp. 8–10, 1988, doi: 10.1109/IEEESTD.1988.79638.

[80] A. V. Mezheritsky, “Invariants of Electromechanical Coupling Coefficients in Piezoceramics,” *IEEE Trans. Ultrason. Ferroelectr. Freq. Control*, vol. 50, no. 12, pp. 1742–1751, Dec. 2003, doi: 10.1109/TUFFC.2003.1256315.

[81] B. a. Auld, “Wave propagation and resonance in piezoelectric materials,” *J. Acoust. Soc. Am.*, vol. 70, no. 6, p. 1577, 1981, doi: 10.1121/1.387223.

[82] H. Jaffe and D. A. Berlincourt, “Piezoelectric Transducer Materials,” *Proc. IEEE*, vol. 53, no. 10, pp. 1372–1386, 1965, doi: 10.1109/PROC.1965.4253.

[83] G. Piazza, V. Felmetsger, P. Muralt, R. H. Olsson, and R. Ruby, “Piezoelectric aluminum nitride thin films for microelectromechanical systems,” *MRS Bull.*, vol. 37, no. 11, pp. 1051–1061, 2012, doi: 10.1557/mrs.2012.268.

[84] R. Ruby, “A Snapshot in Time: The Future in Filters for Cell Phones,” *IEEE Microw. Mag.*, vol. 16, no. 7, pp. 46–59, Aug. 2015, doi: 10.1109/MMM.2015.2429513.

[85] C. C. W. Ruppel, “Acoustic Wave Filter Technology-A Review,” *IEEE Trans. Ultrason. Ferroelectr. Freq. Control*, vol. 64, no. 9, pp. 1390–1400, Sep. 2017, doi: 10.1109/TUFFC.2017.2690905.

[86] C. Campbell, *Surface Acoustic Wave Devices and Their Signal Processing Applications*. San Diego: Academic Press, Inc., 1989.

[87] H. Bhugra and G. Piazza, Eds., *Piezoelectric MEMS resonators*. Springer International Publishing,

2017.

[88] G. S. Kino, *Acoustic Waves: Devices, Imaging, and Analog Signal Processing*. Englewood Cliffs, NJ: Prentice-Hall, Inc., 1987.

[89] R. M. White and F. W. Voltmer, “Direct piezoelectric coupling to surface elastic waves,” *Appl. Phys. Lett.*, vol. 7, no. 12, pp. 314–316, Dec. 1965, doi: 10.1063/1.1754276.

[90] C. S. Lam, “A review of the timing and filtering technologies in smartphones,” in *2016 IEEE International Frequency Control Symposium (IFCS)*, May 2016, pp. 1–6, doi: 10.1109/FCS.2016.7546724.

[91] R. Aigner, “SAW and BAW technologies for RF filter applications: A review of the relative strengths and weaknesses,” in *2008 IEEE Ultrasonics Symposium*, Nov. 2008, pp. 582–589, doi: 10.1109/ULTSYM.2008.0140.

[92] R. Ruby, “The ‘how & why’ a deceptively simple acoustic resonator became the basis of a multi-billion dollar industry,” in *Proceedings of the IEEE International Conference on Micro Electro Mechanical Systems (MEMS)*, Feb. 2017, pp. 308–313, doi: 10.1109/MEMSYS.2017.7863403.

[93] F. Laermer and A. Urban, “MEMS at Bosch – Si plasma etch success story, history, applications, and products,” *Plasma Process. Polym.*, vol. 16, no. 9, p. 1800207, Sep. 2019, doi: 10.1002/ppap.201800207.

[94] S. Tabatabaei and A. Partridge, “Silicon MEMS oscillators for high-speed digital systems,” *IEEE Micro*, vol. 30, no. 2, pp. 80–88, Mar. 2010, doi: 10.1109/MM.2010.39.

[95] C. S. Lam, “A review of the recent development of mems and crystal oscillators and their impacts on the frequency control products industry,” in *Proceedings - IEEE Ultrasonics Symposium*, 2008, pp. 694–704, doi: 10.1109/ULTSYM.2008.0167.

[96] G. Piazza, P. J. Stephanou, and A. P. Pisano, “Single-chip multiple-frequency ALN MEMS filters based on contour-mode piezoelectric resonators,” *J. Microelectromechanical Syst.*, vol. 16, no. 2, pp. 319–328, 2007, doi: 10.1109/JMEMS.2006.889503.

[97] G. Piazza, P. J. Stephanou, and A. P. Pisano, “One and two port piezoelectric higher order contour-mode MEMS resonators for mechanical signal processing,” *Solid. State. Electron.*, vol. 51, no. 11–12, pp. 1596–1608, Nov. 2007, doi: 10.1016/j.sse.2007.09.037.

[98] G. Piazza, P. J. Stephanou, and A. P. Al Pisano, “Piezoelectric Aluminum Nitride Vibrating Contour-Mode MEMS Resonators,” *J. micorelectromechanical Syst.*, vol. 15, no. 6, pp. 1406–1418, 2006, doi: 10.1109/JMEMS.2006.886012.

[99] C.-M. Lin, V. Yantchev, J. Zou, Y.-Y. Chen, and A. P. Pisano, “Micromachined One-Port Aluminum Nitride Lamb Wave Resonators Utilizing the Lowest-Order Symmetric Mode,” *J. Microelectromechanical Syst.*, vol. 23, no. 1, pp. 78–91, Feb. 2014, doi: 10.1109/JMEMS.2013.2290793.

[100] C. M. Lin, Y. J. Lai, J. C. Hsu, Y. Y. Chen, D. G. Senesky, and A. P. Pisano, “High-Q aluminum nitride Lamb wave resonators with biconvex edges,” *Appl. Phys. Lett.*, vol. 99, no. 14, p. 143501, Oct. 2011, doi: 10.1063/1.3643153.

[101] C. Cassella, Y. Hui, Z. Qian, G. Hummel, and M. Rinaldi, “Aluminum Nitride Cross-Sectional Lamé Mode Resonators,” *J. Microelectromechanical Syst.*, vol. 25, no. 2, pp. 275–285, Apr. 2016, doi: 10.1109/JMEMS.2015.2512379.

[102] C. Cassella, G. Chen, Z. Qian, G. Hummel, and M. Rinaldi, “RF passive components based on aluminum nitride cross-sectional lamé-mode MEMS resonators,” *IEEE Trans. Electron Devices*, vol. 64, no. 1, pp. 237–243, Jan. 2017, doi: 10.1109/TED.2016.2621660.

[103] Q. Wang, Y. Lu, S. Mishin, Y. Oshmyansky, and D. A. Horsley, "Design, Fabrication, and Characterization of Scandium Aluminum Nitride-Based Piezoelectric Micromachined Ultrasonic Transducers," *J. Microelectromechanical Syst.*, vol. 26, no. 5, pp. 1132–1139, Oct. 2017, doi: 10.1109/JMEMS.2017.2712101.

[104] M. Moreira, J. Bjurström, I. Katardjev, and V. Yantchev, "Aluminum scandium nitride thin-film bulk acoustic resonators for wide band applications," *Vacuum*, vol. 86, no. 1, pp. 23–26, Jul. 2011, doi: 10.1016/j.vacuum.2011.03.026.

[105] H. Chandrahalim, S. A. Bhave, R. G. Polcawich, J. S. Pulskamp, and D. Judy, "Fully-differential mechanically-coupled PZT-on-silicon filters," in *Proceedings - IEEE Ultrasonics Symposium*, 2008, pp. 713–716, doi: 10.1109/ULTSYM.2008.0170.

[106] J. S. Pulskamp, R. Q. Rudy, S. S. Bedair, J. M. Puder, M. G. Breen, and R. G. Polcawich, "Ferroelectric PZT MEMS HF/VHF resonators/filters," in *2016 IEEE International Frequency Control Symposium, IFCS 2016 - Proceedings*, Aug. 2016, doi: 10.1109/FCS.2016.7546789.

[107] R. G. Polcawich and J. S. Pulskamp, "Additive Processes for Piezoelectric Materials: Piezoelectric MEMS," Springer, Boston, MA, 2011, pp. 273–353.

[108] J. S. Pulskamp *et al.*, "Piezoelectric PZT MEMS technologies for small-scale robotics and RF applications," *MRS Bulletin*, vol. 37, no. 11. Cambridge University Press, pp. 1062–1070, Nov. 2012, doi: 10.1557/mrs.2012.269.

[109] X. Zhu, J. D. Phillips, and A. Mortazawi, "A DC voltage dependant switchable thin film bulk wave acoustic resonator using ferroelectric thin film," in *IEEE MTT-S International Microwave Symposium Digest*, 2007, pp. 671–674, doi: 10.1109/MWSYM.2007.380009.

[110] S. Lee and A. Mortazawi, "An Intrinsically Switchable Ladder-Type Ferroelectric BST-on-Si Composite FBAR Filter," *IEEE Trans. Ultrason. Ferroelectr. Freq. Control*, vol. 63, no. 3, pp. 456–462, Mar. 2016, doi: 10.1109/TUFFC.2016.2517643.

[111] S. Gong and G. Piazza, "Design and analysis of lithium-niobate-based high electromechanical coupling RF-MEMS resonators for wideband filtering," in *IEEE Transactions on Microwave Theory and Techniques*, 2013, vol. 61, no. 1, pp. 403–414, doi: 10.1109/TMTT.2012.2228671.

[112] R. Wang, S. A. Bhave, and K. Bhattacharjee, "Thin-film Lithium Niobate contour-mode resonators," in *IEEE International Ultrasonics Symposium, IUS*, 2012, pp. 303–306, doi: 10.1109/ULTSYM.2012.0074.

[113] R. Wang, S. A. Bhave, and K. Bhattacharjee, "Design and fabrication of S0 Lamb-wave thin-film lithium niobate micromechanical resonators," *J. Microelectromechanical Syst.*, vol. 24, no. 2, pp. 300–308, Apr. 2015, doi: 10.1109/JMEMS.2014.2384916.

[114] S. Gong, Y. H. Song, T. Manzaneque, R. Lu, Y. Yang, and A. Kourani, "Lithium niobate MEMS devices and subsystems for radio frequency signal processing," in *Midwest Symposium on Circuits and Systems*, Sep. 2017, vol. 2017-August, pp. 45–48, doi: 10.1109/MWSCAS.2017.8052856.

[115] R. Wang and S. A. Bhave, "Etch-A-Sketch filter," in *2015 Transducers - 2015 18th International Conference on Solid-State Sensors, Actuators and Microsystems, TRANSDUCERS 2015*, Aug. 2015, pp. 2276–2279, doi: 10.1109/TRANSDUCERS.2015.7181416.

[116] G. Chen and M. Rinaldi, "Aluminum Nitride Combined Overtone Resonators for the 5G High Frequency Bands," *J. Microelectromechanical Syst.*, vol. 29, no. 2, pp. 148–159, Apr. 2020, doi: 10.1109/JMEMS.2020.2975557.

[117] Y. Yang, R. Lu, T. Manzaneque, and S. Gong, "Toward Ka Band Acoustics: Lithium Niobate Asymmetrical Mode Piezoelectric MEMS Resonators," in *IEEE International Frequency Control Symposium (IFCS)*, Dec. 2018, pp. 65–69, doi: 10.1109/FCS.2018.8597475.

[118] R. Lu, T. Manzaneque, Y. Yang, and S. Gong, “Exploiting parallelism in resonators for large voltage gain in low power wake up radio front ends,” in *Proceedings of the IEEE International Conference on Micro Electro Mechanical Systems (MEMS)*, Apr. 2018, vol. 2018-January, pp. 747–750, doi: 10.1109/MEMSYS.2018.8346663.

[119] S. S. Bedair, J. S. Pulskamp, R. G. Polcawich, B. Morgan, J. L. Martin, and B. Power, “Thin-film piezoelectric-on-silicon resonant transformers,” *J. Microelectromechanical Syst.*, vol. 22, no. 6, pp. 1383–1394, Dec. 2013, doi: 10.1109/JMEMS.2013.2262585.

[120] C. Cassella, G. Chen, Z. Qian, G. Hummel, and M. Rinaldi, “920 MHz ALUMINUM NITRIDE CROSS-SECTIONAL LAMÉ MODE PIEZOELECTRIC MEMS TRANSFORMER WITH HIGH OPEN-CIRCUIT VOLTAGE GAIN IN EXCESS OF 39,” in *Solid-State Sensors, Actuators and Microsystems Workshop*, Jun. 2016, pp. 412–415, doi: 10.31438/trf.hh2016.110.

[121] E. Mehdizadeh and G. Piazza, “AlN on SOI pMUTs for ultrasonic power transfer,” in *IEEE International Ultrasonics Symposium, IUS*, Oct. 2017, doi: 10.1109/ULTSYM.2017.8092630.

[122] E. Mehdizadeh and G. Piazza, “Chip-Scale Near-Field Resonant Power Transfer via Elastic Waves,” *J. Microelectromechanical Syst.*, vol. 26, no. 5, pp. 1155–1164, Oct. 2017, doi: 10.1109/JMEMS.2017.2719944.

[123] R. Elfrink *et al.*, “Vibration energy harvesting with aluminum nitride-based piezoelectric devices,” *J. Micromechanics Microengineering*, vol. 19, no. 9, 2009, doi: 10.1088/0960-1317/19/9/094005.

[124] F. Pop *et al.*, “Zero-Power Acoustic Wake-Up Receiver Based on DMUT Transmitter, PMUTS Arrays Receivers and MEMS Switches for Intrabody Links,” in *2019 20th International Conference on Solid-State Sensors, Actuators and Microsystems and Eurosensors XXXIII, TRANSDUCERS 2019 and EUROSENSORS XXXIII*, Jun. 2019, pp. 150–153, doi: 10.1109/TRANSDUCERS.2019.8808176.

[125] X. Jiang *et al.*, “Ultrasonic Fingerprint Sensor with Transmit Beamforming Based on a PMUT Array Bonded to CMOS Circuitry,” *IEEE Trans. Ultrason. Ferroelectr. Freq. Control*, vol. 64, no. 9, pp. 1401–1408, Sep. 2017, doi: 10.1109/TUFFC.2017.2703606.

[126] S. Akhbari, F. Sammoura, S. Shelton, C. Yang, D. Horsley, and L. Lin, “Highly responsive curved aluminum nitride PMUT,” in *Proceedings of the IEEE International Conference on Micro Electro Mechanical Systems (MEMS)*, 2014, pp. 124–127, doi: 10.1109/MEMSYS.2014.6765589.

[127] R. Abdolvand, H. M. Lavasani, G. K. Ho, and F. Ayazi, “Thin-film piezoelectric-on-silicon resonators for high-frequency reference oscillator applications,” *IEEE Trans. Ultrason. Ferroelectr. Freq. Control*, vol. 55, no. 12, pp. 2596–2606, Dec. 2008, doi: 10.1109/TUFFC.2008.976.

[128] M. Rinaldi, C. Zuo, J. Van Der Spiegel, and G. Piazza, “Reconfigurable CMOS oscillator based on multifrequency AlN contour-mode MEMS resonators,” *IEEE Trans. Electron Devices*, vol. 58, no. 5, pp. 1281–1286, May 2011, doi: 10.1109/TED.2011.2104961.

[129] C. Zuo, N. Sinha, J. Van Der Spiegel, and G. Piazza, “Multifrequency pierce oscillators based on piezoelectric AlN contour-mode MEMS technology,” *J. Microelectromechanical Syst.*, vol. 19, no. 3, pp. 570–580, Jun. 2010, doi: 10.1109/JMEMS.2010.2045879.

[130] R. Mahameed, N. Sinha, M. B. Pisani, and G. Piazza, “Dual-beam actuation of piezoelectric AlN RF MEMS switches monolithically integrated with AlN contour-mode resonators,” *J. Micromechanics Microengineering*, vol. 18, p. 10501, Jul. 2008, doi: 10.1088/0960-1317/18/10/105011.

[131] T. Wu, G. Chen, Z. Qian, W. Zhu, M. Rinaldi, and N. McGruer, “A microelectromechanical AlN resoswitch for RF receiver application,” in *TRANSDUCERS 2017 - 19th International Conference on Solid-State Sensors, Actuators and Microsystems*, Jul. 2017, pp. 2123–2126, doi: 10.1109/TRANSDUCERS.2017.7994494.

[132] F. Di Pietrantonio, M. Benetti, D. Cannatà, R. Beccherelli, and E. Verona, “Guided lamb wave electroacoustic devices on micromachined AlN/Al plates,” *IEEE Trans. Ultrason. Ferroelectr. Freq. Control*, vol. 57, no. 5, pp. 1175–1182, May 2010, doi: 10.1109/TUFFC.2010.1530.

[133] N. K. Kuo and G. Piazza, “Evidence of acoustic wave focusing in a microscale 630 MHz Aluminum Nitride phononic crystal waveguide,” in *2010 IEEE International Frequency Control Symposium, FCS 2010*, 2010, pp. 530–533, doi: 10.1109/FREQ.2010.5556274.

[134] R. Lu, Y. Yang, M.-H. Li, and S. Gong, “GHz Low-Loss Acoustic RF Couplers in Lithium Niobate Thin Film,” *IEEE Trans. Ultrason. Ferroelectr. Freq. Control*, pp. 1–1, Feb. 2020, doi: 10.1109/tuffc.2020.2971196.

[135] T. Manzaneque, R. Lu, Y. Yang, and S. Gong, “Lithium Niobate MEMS Chirp Compressors for Near Zero Power Wake-Up Radios,” *J. Microelectromechanical Syst.*, pp. 1–12, 2017, doi: 10.1109/JMEMS.2017.2750176.

[136] J. Schneider *et al.*, “Parametric Coupling in Aluminum Nitride Lamb Wave Devices Through a Nonlinear Elastic Modulus,” in *Bulletin of the American Physical Society*, 2020, vol. Volume 65, Number 1.

[137] A. Ansari and M. Rais-Zadeh, “Frequency-tunable current-assisted AlGaN/GaN acoustic resonators,” in *Proceedings of the IEEE International Conference on Micro Electro Mechanical Systems (MEMS)*, Feb. 2016, vol. 2016-February, pp. 123–126, doi: 10.1109/MEMSYS.2016.7421573.

[138] A. M. Siddiqui *et al.*, “Large Acoustoelectric Effect in Wafer Bonded Indium Gallium Arsenide / Lithium Niobate Heterostructure Augmented by Novel Gate Control,” in *2019 20th International Conference on Solid-State Sensors, Actuators and Microsystems and Eurosensors XXXIII, TRANSDUCERS 2019 and EUROSENSORS XXXIII*, Jun. 2019, pp. 61–64, doi: 10.1109/TRANSDUCERS.2019.8808281.

[139] A. M. Siddiqui *et al.*, “Comparison of amplification via the acousto-electric effect of Rayleigh and Leaky-SAW modes in a monolithic surface InP:InGaAs/lithium niobate heterostructure,” *Ferroelectrics*, vol. 557, no. 1, pp. 58–65, Mar. 2020, doi: 10.1080/00150193.2020.1713363.

[140] A. J. Ricco, S. J. Martin, and T. E. Zipperian, “Surface acoustic wave gas sensor based on film conductivity changes,” *Sensors and Actuators*, vol. 8, no. 4, pp. 319–333, Dec. 1985, doi: 10.1016/0250-6874(85)80031-7.

[141] D. B. Sohn, S. Kim, and G. Bahl, “Time-reversal symmetry breaking with acoustic pumping of nanophotonic circuits,” *Nat. Photonics*, vol. 12, no. 2, pp. 91–97, Feb. 2018, doi: 10.1038/s41566-017-0075-2.

[142] Y. J. Lai, W. C. Li, C. M. Lin, V. V. Felmetsger, and A. P. Pisano, “High-temperature stable piezoelectric aluminum nitride energy harvesters utilizing elastically supported diaphragms,” *2013 Transducers Eurosensors XXVII 17th Int. Conf. Solid-State Sensors, Actuators Microsystems, TRANSDUCERS EUROSENSORS 2013*, no. June, pp. 2268–2271, 2013, doi: 10.1109/Transducers.2013.6627257.

[143] C.-M. Lin *et al.*, “Surface acoustic wave devices on AlN/3C–SiC/Si multilayer structures,” *J. Micromechanics Microengineering*, vol. 23, p. 025019, Jan. 2013, doi: 10.1088/0960-1317/23/2/025019.

[144] T. T. Yen *et al.*, “Characterization of aluminum nitride lamb wave resonators operating at 600°C for harsh environment RF applications,” in *Proceedings of the IEEE International Conference on Micro Electro Mechanical Systems (MEMS)*, 2010, pp. 731–734, doi: 10.1109/MEMSYS.2010.5442304.

[145] G. Piazza, M. Rinaldi, and C. Zuniga, “Nanoscaled piezoelectric aluminum nitride contour-mode

resonant sensors," in *Proceedings of IEEE Sensors*, 2010, pp. 2202–2207, doi: 10.1109/ICSENS.2010.5690615.

[146] Z. Qian, Y. Hui, M. Rinaldi, F. Liu, and S. Kar, "Single transistor oscillator based on a Graphene-Aluminum Nitride nano plate resonator," in *2013 Joint European Frequency and Time Forum and International Frequency Control Symposium, EFTF/IFC 2013*, 2013, pp. 559–561, doi: 10.1109/EFTF-IFC.2013.6702274.

[147] Y. Hui and M. Rinaldi, "Aluminum Nitride nano-plate infrared sensor with self-sustained CMOS oscillator for nano-watts range power detection," in *2013 Joint European Frequency and Time Forum and International Frequency Control Symposium, EFTF/IFC 2013*, 2013, pp. 62–65, doi: 10.1109/EFTF-IFC.2013.6702280.

[148] Y. Hui, T. Nan, N. X. Sun, and M. Rinaldi, "High resolution magnetometer based on a high frequency magnetoelectric MEMS-CMOS oscillator," *J. Microelectromechanical Syst.*, vol. 24, no. 1, pp. 134–143, Feb. 2015, doi: 10.1109/JMEMS.2014.2322012.

[149] J. M. Puder *et al.*, "Rapid Harmonic Analysis of Piezoelectric MEMS Resonators," *IEEE Trans. Ultrason. Ferroelectr. Freq. Control*, vol. 65, no. 6, pp. 979–990, Jun. 2018, doi: 10.1109/TUFFC.2018.2822119.

[150] S. H. Chang, N. N. Rogacheva, and C. C. Chou, "Analysis of methods for determining electromechanical coupling coefficients of piezoelectric elements," *IEEE Trans. Ultrason. Ferroelectr. Freq. Control*, vol. 42, no. 4, pp. 630–640, Jul. 1995, doi: 10.1109/58.393106.

[151] Z. Qian, Y. Hui, and M. Rinaldi, "Effects of volume scaling in AlN nano plate resonators on quality factor," *2016 IEEE Int. Freq. Control Symp. IFCS 2016 - Proc.*, no. c, pp. 1–3, 2016, doi: 10.1109/FCS.2016.7563552.

[152] J. M. Puder, J. S. Pulskamp, R. Q. Rudy, R. G. Polcawich, and S. A. Bhave, "A General Analytical Formulation for the Motional Parameters of Piezoelectric MEMS Resonators," *IEEE Trans. Ultrason. Ferroelectr. Freq. Control*, vol. 65, no. 3, pp. 476–488, Mar. 2018, doi: 10.1109/TUFFC.2018.2793099.

[153] C. Xu and G. Piazza, "Artificial neural network based digital temperature compensation method for aluminum nitride MEMS resonators," in *IEEE International Ultrasonics Symposium, IUS*, Oct. 2017, doi: 10.1109/ULTSYM.2017.8091532.

[154] C. Xu, E. Calayir, and G. Piazza, "Fast and Accurate Prediction of Spurious Modes in Aluminum Nitride MEMS Resonators using," *Ius 2017*, pp. 1–4, 2017.

[155] J. S. Pulskamp *et al.*, "Electrode-shaping for the excitation and detection of permitted arbitrary modes in arbitrary geometries in piezoelectric resonators," *IEEE Trans. Ultrason. Ferroelectr. Freq. Control*, vol. 59, no. 5, pp. 1043–1060, 2012, doi: 10.1109/TUFFC.2012.2290.

[156] J. Zou and C. S. Lam, "Electrode Design of AlN Lamb Wave Resonators," *IEEE Freq. Control Symp.*, p. 7563573, 2016, doi: 10.1109/FCS.2016.7563573.

[157] J. H. Kuypers and A. P. Pisano, "Green's function analysis of lamb wave resonators," in *Proceedings - IEEE Ultrasonics Symposium*, 2008, pp. 1548–1551, doi: 10.1109/ULTSYM.2008.0377.

[158] J. Zou, C. M. Lin, C. S. Lam, and A. P. Pisano, "Transducer design for AlN Lamb wave resonators," *J. Appl. Phys.*, vol. 121, no. 15, p. 154502, Apr. 2017, doi: 10.1063/1.4979914.

[159] R. Lu, M. H. Li, Y. Yang, T. Manzaneque, and S. Gong, "Accurate extraction of large electromechanical coupling in piezoelectric MEMS resonators," *J. Microelectromechanical Syst.*, vol. 28, no. 2, pp. 209–218, Apr. 2019, doi: 10.1109/JMEMS.2019.2892708.

[160] R. L. Kubena, X. Pang, K. G. Lee, Y. K. Yong, and W. S. Wall, "Wide-band multiferroic quartz MEMS antennae," in *18th International Conference on Micro and Nanotechnology for Power*

Generation and Energy Conversion Applications, Dec. 2019, vol. 1407, p. 012026, doi: 10.1088/1742-6596/1407/1/012026.

[161] N. X. Sun and G. Srinivasan, "Voltage control of magnetism in multiferroic heterostructures and devices," *SPIN*, vol. 2, no. 3, Sep. 2012, doi: 10.1142/S2010324712400048.

[162] G. M. Yang *et al.*, "Dual H-and E-field tunable multiferroic bandpass filters with yttrium iron garnet film," in *IEEE MTT-S International Microwave Symposium Digest*, 2011, doi: 10.1109/MWSYM.2011.5972897.

[163] M. Liu *et al.*, "Giant Electric Field Tuning of Magnetic Properties in Multiferroic Ferrite/Ferroelectric Heterostructures," *Adv. Funct. Mater.*, vol. 19, no. 11, pp. 1826–1831, Jun. 2009, doi: 10.1002/adfm.200801907.

[164] J. Zhang, P. Li, Y. Wen, W. He, A. Yang, and C. Lu, "Shear-mode self-biased magnetostrictive/piezoelectric laminate multiferroic heterostructures for magnetic field detecting and energy harvesting," *Sensors Actuators, A Phys.*, vol. 214, pp. 149–155, Aug. 2014, doi: 10.1016/j.sna.2014.04.037.

[165] Y. Zhou, D. J. Apo, and S. Priya, "Dual-phase self-biased magnetoelectric energy harvester," *Appl. Phys. Lett.*, vol. 103, no. 19, 2013, doi: 10.1063/1.4829151.

[166] T. D. Onuta, Y. Wang, C. J. Long, and I. Takeuchi, "Energy harvesting properties of all-thin-film multiferroic cantilevers," *Appl. Phys. Lett.*, vol. 99, no. 20, pp. 10–13, 2011, doi: 10.1063/1.3662037.

[167] U. Azad, H. C. Jing, and Y. E. Wang, "Link budget and capacity performance of inductively coupled resonant loops," *IEEE Trans. Antennas Propag.*, vol. 60, no. 5, pp. 2453–2461, 2012, doi: 10.1109/TAP.2012.2189696.

[168] A. Kurs, A. Karalis, R. Moffatt, J. D. Joannopoulos, P. Fisher, and M. Soljačić, "Wireless power transfer via strongly coupled magnetic resonances," *Science (80-.).*, vol. 317, no. 5834, pp. 83–86, Jul. 2007, doi: 10.1126/science.1143254.

[169] A. E. Hassanien, M. Breen, M. H. Li, and S. Gong, "A theoretical study of acoustically driven antennas," *J. Appl. Phys.*, vol. 127, no. 1, p. 014903, Jan. 2020, doi: 10.1063/1.5129945.

[170] J. P. Domann and G. P. Carman, "Strain powered antennas," *J. Appl. Phys.*, vol. 121, no. 4, p. 044905, Jan. 2017, doi: 10.1063/1.4975030.

[171] J. Hu, "High Frequency Multiferroic Devices," University of California, Los Angeles, 2020.

[172] P. Nordeen, "High Frequency Dynamics of Magnetoelastic Composites and Their Application in Radio Frequency Sensors," University of California, Los Angeles, 2016.

[173] D. Labanowski, A. Jung, and S. Salahuddin, "Power absorption in acoustically driven ferromagnetic resonance," *Appl. Phys. Lett.*, vol. 108, no. 2, 2016, doi: 10.1063/1.4939914.

[174] L. Dreher *et al.*, "Surface acoustic wave driven ferromagnetic resonance in nickel thin films: Theory and experiment," *Phys. Rev. B - Condens. Matter Mater. Phys.*, vol. 86, no. 13, p. 134415, Oct. 2012, doi: 10.1103/PhysRevB.86.134415.

[175] K. Nygren *et al.*, "On and Off-Resonance Spin Wave/Surface Acoustic Wave Coupling Measured Using Brillouin Light Scattering," in *Bulletin of the American Physical Society*, 2019, vol. Volume 64, Number 2.

[176] P. Chowdhury, P. Dhagat, and A. Jander, "Parametric amplification of spin waves using acoustic waves," *IEEE Trans. Magn.*, vol. 51, no. 11, Nov. 2015, doi: 10.1109/TMAG.2015.2445791.

[177] W. Li, B. Buford, A. Jander, and P. Dhagat, "Writing magnetic patterns with surface acoustic waves," in *Journal of Applied Physics*, May 2014, vol. 115, no. 17, p. 17E307, doi:

10.1063/1.4863170.

[178] B. Casals *et al.*, “Generation and Imaging of Magnetoacoustic Waves over Millimeter Distances,” *Phys. Rev. Lett.*, vol. 124, no. 13, p. 137202, Apr. 2020, doi: 10.1103/physrevlett.124.137202.

[179] M. Foerster *et al.*, “Direct imaging of delayed magneto-dynamic modes induced by surface acoustic waves,” *Nat. Commun.*, vol. 8, no. 1, pp. 1–6, 2017, doi: 10.1038/s41467-017-00456-0.

[180] P. Kuszewski *et al.*, “Resonant magneto-acoustic switching: influence of Rayleigh wave frequency and wavevector,” *J. Phys. Condens. Matter*, vol. 30, no. 24, p. 244003, Jun. 2018, doi: 10.1088/1361-648X/aac152.

[181] S. Tateno and Y. Nozaki, “ Highly Nonreciprocal Spin Waves Excited by Magnetoelastic Coupling in a Ni / Si Bilayer ,” *Phys. Rev. Appl.*, vol. 13, no. 3, p. 034074, Mar. 2020, doi: 10.1103/physrevapplied.13.034074.

[182] R. Sasaki, Y. Nii, Y. Iguchi, and Y. Onose, “Nonreciprocal propagation of surface acoustic wave in Ni/LiNbO3,” *Phys. Rev. B,* vol. 95, no. 2, p. 020407, Jan. 2017, doi: 10.1103/PhysRevB.95.020407.

[183] M. Küß *et al.*, “Nonreciprocal Dzyaloshinskii-Moriya magnetoacoustic waves,” Apr. 2020, Accessed: May 04, 2020. [Online]. Available: http://arxiv.org/abs/2004.03535.

[184] S. Alekseev, N. Polzikova, I. Kotelyanskii, and Y. Fetisov, “Tunable HBAR based on magnetoelectric YIG/ZnO structure,” in *IEEE International Ultrasonics Symposium, IUS*, 2012, pp. 2481–2484, doi: 10.1109/ULTSYM.2012.0621.

[185] N. Polzikova, S. Alekseev, I. Kotelyanskii, and A. Raevskiy, “Acoustically driven magnetic excitations in BAW resonators with magnetic layers,” *IEEE Int. Ultrason. Symp. IUS*, pp. 216–219, 2013, doi: 10.1109/ULTSYM.2013.0056.

[186] N. Polzikova, S. Alekseev, I. Kotelyanskii, and A. Raevskiy, “Magnetic field influence on the spectra of BAW resonator with ferrite layers,” *IFCS 2014 - 2014 IEEE Int. Freq. Control Symp. Proc.*, pp. 3–6, 2014, doi: 10.1109/FCS.2014.6859874.

[187] A. V. Chumak, P. Dhagat, A. Jander, A. A. Serga, and B. Hillebrands, “Reverse Doppler effect of magnons with negative group velocity scattered from a moving Bragg grating,” *Phys. Rev. B - Condens. Matter Mater. Phys.*, vol. 81, no. 14, p. 140404, Apr. 2010, doi: 10.1103/PhysRevB.81.140404.

[188] P. G. Gowtham, D. Labanowski, and S. Salahuddin, “Mechanical back-action of a spin-wave resonance in a magnetoelastic thin film on a surface acoustic wave,” *Phys. Rev. B*, vol. 94, no. 1, p. 014436, Jul. 2016, doi: 10.1103/PhysRevB.94.014436.

[189] X. Li, D. Labanowski, S. Salahuddin, and C. S. Lynch, “Spin wave generation by surface acoustic waves,” *J. Appl. Phys.*, vol. 122, no. 4, p. 043904, Jul. 2017, doi: 10.1063/1.4996102.

[190] Z. Yao *et al.*, “Modeling of Multiple Dynamics in the Radiation of Bulk Acoustic Wave Antennas,” *IEEE J. Multiscale Multiphysics Comput. Tech.*, vol. 5, pp. 7–20, 2020, doi: 10.1109/JMMCT.2019.2959596.

[191] Z. Yao, R. U. Tok, T. Itoh, and Y. E. Wang, “A Multiscale Unconditionally Stable Time-Domain (MUST) Solver Unifying Electrodynamics and Micromagnetics,” *IEEE Trans. Microw. Theory Tech.*, vol. 66, no. 6, pp. 2683–2696, Jun. 2018, doi: 10.1109/TMTT.2018.2825373.

[192] R. C. O’Handley, *Modern Magnetic Materials: Principles and Applications*. John Wiley & Sons, Inc., 2000.

[193] D. Jiles, *Introduction to Magnetism and Magnetic Materials*, 2nd ed. London, UK: Chapman & Hall, 1998.

[194] M. Kläui *et al.*, “Direct observation of spin configurations and classification of switching processes

in mesoscopic ferromagnetic rings," *Phys. Rev. B - Condens. Matter Mater. Phys.*, vol. 68, no. 13, p. 134426, Oct. 2003, doi: 10.1103/PhysRevB.68.134426.

[195] J. Raabe, C. Quitmann, C. H. Back, F. Nolting, S. Johnson, and C. Buehler, "Quantitative analysis of magnetic excitations in landau flux-closure structures using synchrotron-radiation microscopy," *Phys. Rev. Lett.*, vol. 94, no. 21, p. 217204, Jun. 2005, doi: 10.1103/PhysRevLett.94.217204.

[196] S. Wintz *et al.*, "Magnetic vortex cores as tunable spin-wave emitters," *Nat. Nanotechnol.*, vol. 11, no. 11, pp. 948–953, Nov. 2016, doi: 10.1038/nnano.2016.117.

[197] H. Sohn *et al.*, "Deterministic multi-step rotation of magnetic single-domain state in Nickel nanodisks using multiferroic magnetoelastic coupling," *J. Magn. Magn. Mater.*, vol. 439, pp. 196–202, Oct. 2017, doi: 10.1016/j.jmmm.2017.04.077.

[198] T. Kampfrath *et al.*, "Coherent terahertz control of antiferromagnetic spin waves," *Nat. Photonics*, vol. 5, no. 1, pp. 31–34, Jan. 2011, doi: 10.1038/nphoton.2010.259.

[199] A. Aharoni, "Demagnetizing factors for rectangular ferromagnetic prisms," *J. Appl. Phys.*, vol. 83, no. 6, pp. 3432–3434, 1998, doi: 10.1063/1.367113.

[200] R. Eisberg and R. Resnick, *Quantum Physics of Atoms, Molecules, Solids, Nuclei, and Particles*, 2nd ed. John Wiley & Sons, Inc., 1985.

[201] D. D. Stancil and A. Prabhakar, *Spin Waves: Theory and Applications*. Springer, 2009.

[202] J. B. Goodenough, "Summary of losses in magnetic materials," *IEEE Trans. Magn.*, vol. 38, no. 5 II, pp. 3398–3408, Sep. 2002, doi: 10.1109/TMAG.2002.802741.

[203] G. F. Dionne, "Magnetic Relaxation and Anisotropy Effects on High-Frequency Permeability," *IEEE Trans. Magn.*, vol. 39, no. 5 II, pp. 3121–3126, Sep. 2003, doi: 10.1109/TMAG.2003.816026.

[204] T. Tsutaoka, T. Nakamura, and K. Hatakeyama, "Magnetic field effect on the complex permeability spectra in a Ni-Zn ferrite," *J. Appl. Phys.*, vol. 82, no. 6, pp. 3068–3071, Sep. 1997, doi: 10.1063/1.366145.

[205] M. Manteghi and A. A. Y. Ibraheem, "On the study of the near-fields of electric and magnetic small antennas in lossy media," *IEEE Trans. Antennas Propag.*, vol. 62, no. 12, pp. 6491–6495, Dec. 2014, doi: 10.1109/TAP.2014.2359499.

[206] D. Viehland, M. Wuttig, J. McCord, and E. Quandt, "Magnetoelectric magnetic field sensors," *MRS Bull.*, vol. 43, no. 11, pp. 834–840, Nov. 2018, doi: 10.1557/mrs.2018.261.

[207] S. Dong, J. F. Li, D. Viehland, J. Cheng, and L. E. Cross, "A strong magnetoelectric voltage gain effect in magnetostrictive- piezoelectric composite," *Appl. Phys. Lett.*, vol. 85, no. 16, pp. 3534–3536, Oct. 2004, doi: 10.1063/1.1786631.

[208] C. M. Leung, X. Zhuang, J. Xu, J. Li, G. Srinivasan, and D. Viehland, "Importance of composite parameters in enhanced power conversion efficiency of Terfenol-D/PZT magnetoelectric gyrators," *Appl. Phys. Lett.*, vol. 110, no. 11, p. 112904, Mar. 2017, doi: 10.1063/1.4978751.

[209] Y. Wang *et al.*, "An Extremely Low Equivalent Magnetic Noise Magnetoelectric Sensor," *Adv. Mater.*, vol. 23, no. 35, pp. 4111–4114, Sep. 2011, doi: 10.1002/adma.201100773.

[210] C. Kirchhof *et al.*, "Giant magnetoelectric effect in vacuum," *Appl. Phys. Lett.*, vol. 102, no. 23, p. 232905, Jun. 2013, doi: 10.1063/1.4810750.

[211] B. Gojdka *et al.*, "Fully integrable magnetic field sensor based on delta-E effect," *Appl. Phys. Lett.*, vol. 99, no. 22, p. 223502, Nov. 2011, doi: 10.1063/1.3664135.

[212] R. Jahns, H. Greve, E. Woltermann, E. Quandt, and R. Knöchel, "Sensitivity enhancement of magnetoelectric sensors through frequency-conversion," *Sensors Actuators, A Phys.*, vol. 183, pp.

16–21, Aug. 2012, doi: 10.1016/j.sna.2012.05.049.

[213] P. Hayes *et al.*, “Electrically modulated magnetoelectric sensors,” *Appl. Phys. Lett.*, vol. 108, no. 18, p. 182902, May 2016, doi: 10.1063/1.4948470.

[214] K. E. Kamentsev, Y. K. Fetisov, and G. Srinivasan, “Low-frequency nonlinear magnetoelectric effects in a ferrite-piezoelectric multilayer,” *Appl. Phys. Lett.*, vol. 89, no. 14, p. 142510, Oct. 2006, doi: 10.1063/1.2360239.

[215] J. G. Wan, J. M. Liu, H. L. W. Chand, C. L. Choy, G. H. Wang, and C. W. Nan, “Giant magnetoelectric effect of a hybrid of magnetostrictive and piezoelectric composites,” *J. Appl. Phys.*, vol. 93, no. 12, pp. 9916–9919, Jun. 2003, doi: 10.1063/1.1577404.

[216] L. Y. Fetisov, Y. K. Fetisov, G. Sreenivasulu, and G. Srinivasan, “Nonlinear resonant magnetoelectric interactions and efficient frequency doubling in a ferromagnetic-ferroelectric layered structure,” *J. Appl. Phys.*, vol. 113, no. 11, p. 116101, Mar. 2013, doi: 10.1063/1.4798579.

[217] B. G. Colpitts and G. Boiteau, “Harmonic radar transceiver design: Miniature tags for insect tracking,” *IEEE Trans. Antennas Propag.*, vol. 52, no. 11, pp. 2825–2832, Nov. 2004, doi: 10.1109/TAP.2004.835166.

[218] S. Tiwari and R. N. Candler, “Using flexural MEMS to study and exploit nonlinearities: A review,” *J. Micromechanics Microengineering*, vol. 29, no. 8, p. 083002, Jun. 2019, doi: 10.1088/1361-6439/ab23e2.

[219] Z. Xiao *et al.*, “Bi-directional coupling in strain-mediated multiferroic heterostructures with magnetic domains and domain wall motion,” *Sci. Rep.*, vol. 8, no. 1, p. 5207, Dec. 2018, doi: 10.1038/s41598-018-23020-2.

[220] F. J. Rachford, P. Lubitz, and C. Vittoria, “Magnetic multi-domain resonance in single crystal ferrite platelets,” *J. Appl. Phys.*, vol. 52, no. 3, pp. 2259–2260, Mar. 1981, doi: 10.1063/1.328898.

[221] S. Saravanan, E. Berenschot, G. Krijnen, and M. Elwenspoek, “A novel surface micromachining process to fabricate AlN unimorph suspensions and its application for RF resonators,” *Sensors Actuators, A Phys.*, vol. 130–131, no. SPEC. ISS., pp. 340–345, Aug. 2006, doi: 10.1016/j.sna.2005.09.029.

[222] M. J. Donahue and D. G. Porter, “OOMMF User’s Guide, Version 1.0,” *Natl. Inst. Stand. Technol.*, 1999.

[223] J. D. Schneider *et al.*, “Acoustically Driven Magnetic Oscillations at High Frequency,” in *ASME 2019 Conference on Smart Materials, Adaptive Structures and Intelligent Systems*, 2019.

[224] D. Labanowski, A. Jung, and S. Salahuddin, “Effect of magnetoelastic film thickness on power absorption in acoustically driven ferromagnetic resonance,” *Appl. Phys. Lett.*, 2017, doi: 10.1063/1.4994933.

[225] M. Weiler *et al.*, “Elastically driven ferromagnetic resonance in nickel thin films,” *Phys. Rev. Lett.*, vol. 106, no. 11, pp. 1–4, 2011, doi: 10.1103/PhysRevLett.106.117601.

[226] D. Labanowski, “Acoustically Driven Ferromagnetic Resonance for Device Applications,” University of California, Berkeley, 2017.

[227] J. P. Parekh and H. L. Bertoni, “Magnetoelastic Rayleigh waves propagating along a tangential bias field on a YIG substrate,” *J. Appl. Phys.*, vol. 45, no. 1, pp. 434–445, Jan. 1974, doi: 10.1063/1.1662999.

[228] R. S. Weis and T. K. Gaylord, “Lithium niobate: Summary of physical properties and crystal structure,” *Appl. Phys. A Solids Surfaces*, vol. 37, no. 4, pp. 191–203, Aug. 1985, doi:

10.1007/BF00614817.

[229] L. J. Schowalter *et al.*, “Preparation and characterization of single-crystal aluminum nitride substrates,” *Mater. Res. Soc. Symp. - Proc.*, vol. 595, no. S1, pp. 445–451, 2000, doi: 10.1557/s1092578300004622.

[230] J. Lou, R. E. Insignares, Z. Cai, K. S. Ziemer, M. Liu, and N. X. Sun, “Soft magnetism, magnetostriction, and microwave properties of FeGaB thin films,” *Appl. Phys. Lett.*, vol. 91, no. 18, pp. 18–20, 2007, doi: 10.1063/1.2804123.

[231] D. W. Hoffman, “Perspective on stresses in magnetron-sputtered thin films,” *J. Vac. Sci. Technol. A Vacuum, Surfaces, Film.*, vol. 12, no. 4, pp. 953–961, 1994, doi: 10.1116/1.579073.

[232] J. Bjurström, G. Wingqvist, and I. Katardjiev, “Synthesis of textured thin piezoelectric AlN films with a nonzero C-axis mean tilt for the fabrication of shear mode resonators,” *IEEE Trans. Ultrason. Ferroelectr. Freq. Control*, vol. 53, no. 11, pp. 2095–2100, Nov. 2006, doi: 10.1109/TUFFC.2006.149.

[233] C. J. Chung, Y. C. Chen, C. C. Cheng, and K. S. Kao, “An improvement of tilted AlN for shear and longitudinal acoustic wave,” *Appl. Phys. A Mater. Sci. Process.*, vol. 94, no. 2, pp. 307–313, Feb. 2009, doi: 10.1007/s00339-008-4793-7.

[234] S. M. Tanner and V. V. Felmetsger, “Microstructure and chemical wet etching characteristics of AlN films deposited by ac reactive magnetron sputtering,” *J. Vac. Sci. Technol. A Vacuum, Surfaces, Film.*, vol. 28, no. 1, pp. 69–76, Jan. 2010, doi: 10.1116/1.3268620.

[235] D. Chen, D. Xu, J. Wang, B. Zhao, and Y. Zhang, “Dry etching of AlN films using the plasma generated by fluoride,” *Vacuum*, vol. 83, no. 2, pp. 282–285, Sep. 2008, doi: 10.1016/j.vacuum.2008.07.007.

[236] J. S. Wang, Y. Y. Chen, and K. M. Lakin, “Reactive Ion Etching of Piezoelectric Films for Acoustic Wave Devices,” in *1982 Ultrasonics Symposium*, 1982, pp. 346–349, doi: 10.1109/ULTSYM.1982.197843.

[237] P. B. Chu *et al.*, “Controlled pulse-etching with xenon difluoride,” in *International Conference on Solid-State Sensors and Actuators, Proceedings*, 1997, vol. 1, pp. 665–668, doi: 10.1109/sensor.1997.613739.

[238] K. R. Williams and R. S. Muller, “Etch rates for micromachining processing,” *J. Microelectromechanical Syst.*, vol. 5, no. 4, pp. 256–269, Dec. 1996, doi: 10.1109/84.546406.

[239] K. R. Williams, K. Gupta, and M. Wasilik, “Etch rates for micromachining processing - Part II,” *J. Microelectromechanical Syst.*, vol. 12, no. 6, pp. 761–778, Dec. 2003, doi: 10.1109/JMEMS.2003.820936.

[240] M. Li *et al.*, “Ultra-sensitive NEMS magnetoelectric sensor for picotesla DC magnetic field detection,” *Appl. Phys. Lett.*, vol. 110, no. 14, 2017, doi: 10.1063/1.4979694.